R-04-79

System and safety studies of accelerator driven transmutation

Annual Report 2003

Waclaw Gudowski, Jan Wallenius, Kamil Tucek,
Marcus Eriksson, Johan Carlsson, Per Seltborg,
Jerzy Cetnar, Mikael Jollkonen, Christina Lagerstedt,
Alberto Talamo, Daniel Westlén and André Grisell

Department of Nuclear and Reactor Physics
Royal Institute of Technology, Stockholm

December 2004

Svensk Kärnbränslehantering AB
Swedish Nuclear Fuel
and Waste Management Co
Box 5864
SE-102 40 Stockholm Sweden
Tel 08-459 84 00
+46 8 459 84 00
Fax 08-661 57 19
+46 8 661 57 19

ISSN 1402-3091
SKB Rapport R-04-79

System and safety studies of accelerator driven transmutation

Annual Report 2003

Waclaw Gudowski, Jan Wallenius, Kamil Tucek,
Marcus Eriksson, Johan Carlsson, Per Seltborg,
Jerzy Cetnar, Mikael Jollkonen, Christina Lagerstedt,
Alberto Talamo, Daniel Westlén and André Grisell

Department of Nuclear and Reactor Physics
Royal Institute of Technology, Stockholm

December 2004

The full report including all Appendices is available as a .pdf-file on the enclosed CD-ROM-disc. The printed version contains only the main text and a list of the Appendices.

The research on safety of Accelerator-Driven Transmutation Systems (ADS) at the Department of Nuclear and Reactor Physics reported here has been focused on different aspects of safety of the Accelerator-Driven Transmutation Systems and on Transmutation research in more general terms. An overview of the topics of our research is given in the Summary which is followed by detailed reports as separate chapters or subchapters.

Some of the research topics reported in this report are referred to appendices, which have been published in the open literature. Topics, which are not yet published, are described with more details in the main part of this report. The main report is also included in a PDF-format on a CD-ROM attached to this report. The Appendices are only included in the CD-ROM disc.

Blue text color in a PDF version of this report implies links which can take a reader by a mouse click to the referred part of the report or to a referred Appendix.

Abbreviations and acronyms are explained in a table on pages 16-20. The appendices are submitted with the printed report on a CD-ROM.

A summary in Swedish is given in the very early chapter called “SAMMAN-FATTNING”.

SUMMARY

The results of the research activities on safety of Accelerator-Driven Transmutation Systems (ADS) at the Department of Nuclear and Reactor Physics have been extensively described in the number of papers published in 2003. All the papers are attached in Appendices. In particular a PhD dissertation of Johan Carlsson "Inherent Safety Features and Passive Prevention Approaches for Pb/Bi-cooled Accelerator-Driven Systems" (Appendix 1) and licentiate dissertation of Per Seltborg "External Source Effects and Neutronics in Accelerator-Driven Systems" (Appendix 2) have been finished and defended in 2003. Main focus has been as before largely determined by the programme of the European projects of the 5th Framework Programme in which KTH is actively participating. In particular:

a) ADS core design and development of advanced nuclear fuel optimised for high transmutation rates and good safety features. This activity includes even computer modeling of nuclear fuel production. Three different ADS-core concept are being investigated:
    - Conceptual design of Pb-Bi cooled core with nitride fuel – so called Sing-Sing Core developed at KTH
    - Pb-Bi cooled core with oxide fuel – so called ANSALDO design for the European Project PDS-XADS
    - Gas cooled core with oxide fuel – a design investigated for the European Project PDS-XADS.

b) analysis of potential of advance fuels, in particular nitrides with high content of minor actinides

c) analysis of ADS-dynamics and assessment of major reactivity feedbacks;

d) emergency heat removal from ADS;

e) participation in ADS: MUSE (CEA-Cadarache), YALINA subcritical experiment in Minsk and designing of the subcritical experiment SAD in Dubna;

f) theoretical and simulation studies of radiation damage in high neutron (and/or proton) fluxes ;

g) computer code and nuclear data development relevant for simulation and optimization of ADS, validation of the MCB code and sensitivity analysis;

h) studies of transmutation potential of critical reactors in particular High Temperature Gas Cooled Reactor.

Most important findings and conclusions from our studies are

ADS-cores:

- Reactor cores with high minor actinide content fuel exhibit generally higher void worth than cores fueled primarily with plutonium. A disadvantage of sodium versus lead/bismuth in terms of larger positive coolant void worth is apparent for all transmutation type fuels investigated.

- For an FBR with $(U,Pu)O_2$ fuel, Pb/Bi yields larger void worth than sodium when P/D ≥ 1.4. While in sodium cooled FBRs the negative reactivity is introduced upon coolant voiding by both increase of neutron capture in structural material and coolant (in the reflectors and plena), in Pb/Bi-cooled reactors the reactivity contribution is negative only from the former.

- In lead/bismuth-cooled systems, a radial steel pin reflector has to be applied, if coolant void worth is to be significantly reduced.

- Enlarging the pitch-to-diameter ratio P/D lowers the coolant void worth in ADS burners operating in two-component scenario, while ADS burners with MA based fuel should be designed with minimum allowable P/D.

- Pins with small diameters and non-absorbing fuel matrices are preferable with respect to the coolant void worth. However, even an application of strongly absorbing matrix (HfN), does not have to deteriorate the void worth critically; large amount of negative reactivity still being introduced into the reactor upon voiding both core & upper plenum, as e.g. in TRU-fueled ADS

- The excess of neutrons in a plutonium fueled fast reactor may be used to increase the pin pitch to diameter ratio. By doing this it is possible to design a gas cooled fast core where cooling is sufficient even during a severe loss of pressure accident, while maintaining a high burnup

- Actinide transmutation was demonstrated in the simulated gas cooled XADS core. However, the masses possible to transmute in this facility are small.

- Transmutation of technetium is very questionable. Even with a large introduction of technetium, the build-up in the driver fuel will be in the same order of magnitude as the actual destruction. In fact also for most actinide isotopes, the build-up in the fuel is larger than the transmutation in the special assemblies. Large-scale transmutation will require dedicated cores with far higher contents of the nuclei to be transmuted. In addition, the neutron fluence should be significantly higher in order to achieve high transmutation efficiencies. Inserting special transmutation assemblies into the XADS may show valuable for proving technology

Core Reference Cycle Analysis for the Gas-Cooled XADS:

- The cycle length is limited by the criticality of 0.97 at Beginning of Life and by the current of 5mA at End of Life. In the MCB burn-up calculation in single batch cycle the limiting current is reached after cycle length of 993 full power days

- Three-batch cycle requires higher fuel enrichment than in single batch case what could raise the critical above unity when the whole core was loaded with the fresh fuel. Therefore in pre-equilibrium state a few sub-assemblies must be voided to keep the criticality within its constraints

- Differences between MCB and ERANOS/ECCO code systems have been assessed and in principle understood.

- Evaluation of Radiation Damage and Circuit Activation of the Gas-Cooled XADS shows:

- Activation of spallation target loop is dominated by the nuclides produced with core flux neutron. Predominant here are ^{210}Po, ^{210}Bi, ^{209}Pb, ^{207}Bi and ^{210m}Bi.
- The overall activity after 1 year of full power is about $1.1*10^{16}$ Bq and it grows modestly after that time since ^{210}Po reached its equilibrium. The peak value could be about 10 % higher if irradiation time will be extended to 10 years. Quoted values refer to full power operation. If the beam availability were 50% the activity at equilibrium would be also 50% of that for full power. The accumulated mass of ^{210}Po, the most hazardous nuclide is about 34 grams but it could be responsible for intake risks of $6.8*10^{17}$Sv

The LBE-Cooled XADS

Core Reference Cycle Analysis

The core cycle analysis was performed for two cases of fuel enrichments: the single enrichment and the dual enrichment. Comparative analysis of obtained results shows that with the introduction of the dual enrichment fuel the core has:

- higher Pu and MA load,
- smaller reactivity and proton beam current change rate,
- the radial form factor lowered by about 12% from 1.26 to 1.11.
- the source neutron multiplication factor k_s ~ 500 pcm smaller as compared to the single enrichment case for the same level of criticality k_{eff}.

Nuclear Data Sensitivity Analysis

- The difference in reactivity at BOC between JEF and ENDF is about 4000 pcm, for gas-cooled XADS loaded with 50% MA fuel. This indicates that uncertainty in nuclear data for MA are still large and must be improved.
- The differences associated with the applied calculation method or an introduction of heterogeneous fuel distribution can increase that gap further, possibly exceeding 5000 pcm.
- A faster transmutation of americium in the JEF case, and its lower fission cross sections, compared to the ENDF case, are responsible for the observed difference in reactivity swing.

Radiotoxicity Assessment of the Spallation Target Module

- Nuclides predominant for radiotoxicity build-up originated from interaction with core neutrons are: ^{210}Po, ^{210}Bi, ^{209}Pb, ^{207}Bi, ^{210m}Bi and ^{206}Bi, ^{205}Bi.
- The major contributions from spallation process are: ^{194}Hg, ^{204}Tl, ^{198}Au, ^{203}Pb, ^{203}Bi.

- The list of most volatile and radiotoxic nuclides is the following: ^{194}Hg, ^{197}Hg, ^{203}Hg, ^{195}Hg, ^{193}Hg, ^{125}I, ^{126}I, ^{124}I, ^{130}I, ^{123}I, ^{120}I, ^{82}Br, ^{76}Br, ^{84}Br, ^{83}Br, ^{77}Br, ^{80}Br.
- ^{194}Hg predominates the toxicity of that group and due to its physical and chemical properties and substantially long half-life time it should bring much attention for further research of its migration and prevention against contamination of accelerator vacuum tube.

Advanced fuels for ADS

- The Mo-cermet fuel is clearly superior with regard to thermal conductivity, which indicates much better the thermal performance, but yet very little information is available on its irradiation performance. Under normal operating conditions, the primary design constraint is due to the cladding temperature limits.
- The ferritic steels do not posses sufficient strength at high temperature operation whereas the austenitic steels are limited by radiation damage and coolant corrosion attack. Compared to austenitic stainless steel, ferritic/martensitic steels demand lower operating temperatures in return for improved cladding operating life.
- Standard 316 austenitic steel is not expected to survive the neutron doses and the corrosive environment anticipated for a lead/bismuth-cooled reactor. The CW 15-15Ti stainless steel is selected as cladding material because it has a proven irradiation resistance and reasonable knowledge is available on the mechanical performance of this type of steel.
- The maximum fluence of this steel may still remain below some goals and the Pb/Bi corrosion resistance is not known, so the choice may change as more data becomes available.

MUSE experiment:

- Experiments with a limited replacement of sodium coolant by lead coolant gives significantly higher source efficiency than for the sodium-cooled configuration, 2.39 compared to 2.13. There are significant differences for the dynamic neutron source response in both cases.
- MUSE experiment indicates proton importance monitoring as one of the methods for subcriticality monitoring.

Point kinetic model for ADS:

- MUSE experiments has revealed significant difficulties in describing details of MUSE-kinetic with a point model. However, the point kinetics approximation is capable of producing highly accurate results for many types of transients in ADS’s.

The passive emergency decay heat removal during severe cooling accidents in Pb/Bi-cooled ADS

- A large accelerator-driven system of 800 MWth with a 17 m tall vessel may eventually become a standard engineering size. For this high power ADS, the location of the heat-exchangers has great impact on the natural convection capability. The design with heat-exchangers in the downcomers, the long-term vessel temperature peaks at 996 K during a loss-of-flow accident with the beam on. This does not pose a threat of creep rupture for the vessel. The location of the heat-exchangers in the downcomers will probably require secondary coolant other than water, like for example oil (for temperatures not higher than 673 K) or Pb/Bi coolant.

Better understanding of radiation damage mechanisms:

- A need to introduce a many-body potential into the Embedded Atom Method (EAM), dependent on the local Cr concentration in order to predict a correct cluster size distribution.
- Potentials for Fe-C and Cr-C are needed, with the purpose of simulating formation of metal-carbide precipitates, which are known to govern the mechanical properties of real steels.

The Deep Burn - Modular Helium Reactor (DB-MHR) may effectively and safely burn LWRs wastes. Neutronic parameters of this reactor are very favorable: both the fuel and moderator temperature coefficients are negative; in addition, the temperature coefficient of moderator is very large (about 4000-9000 pcm) and it is one order of magnitude higher than the value of the fuel coefficient. The temperature coefficients allow this reactor to shutdown automatically in an accident scenario.

MCB-code needs some extra attention and development to handle ^{135}Xe oscillations for PWR-like simulations. MCB validation simulations revealed that a special Monte Carlo routine has to be developed to handle properly oscillations of ^{135}Xe. The same approach may also be applied for void oscillations in simulations of BWRs.

SAMMANFATTNING

Avdelningen för Kärn- och reaktorfysik på KTH har under år 2003 forskat om avancerade reaktorsystem, särskilt acceleratordrivna sådana, för transmutation av kärnavfall. Forskningen har haft särskilt fokus på följande områden:

- Utformning och utveckling av flera modeller av underkritiska reaktorhärdar
- Datormodellering av produktionsmetoder för uranfria nitridbränslen
- Datormodellering av egenskaper hos nitridbränslen med hög americiumhalt
- Underkritisk reaktordynamik
- Nödkylning av acceleratordrivna reaktorer
- Deltagande i och planering av flera internationella reaktorfysikaliska experiment
- Simulering av strålskador i konstruktionsmaterial
- Utveckling av simuleringskoder och kärndatabibliotek
- Utvärdering av avancerade kritiska reaktorer ur transmutationssynpunkt.

Avdelningen är aktiv i en rad EU-projekt och deltar i internationell experimentverksamhet. Arbetet har under året redovisats i 15 vetenskapliga artiklar, konferensbidrag och tekniska rapporter, vilka redovisas i appendici. Bland dessa märks även en doktors- och en licenciatavhandling som framgångsrikt försvarats av på avdelningen verksamma forskarstuderande.

Till de mer intressanta resultaten hör följande:

Reaktorhärdar med stort innehåll av högre aktinider har högre voidkoefficient än utpräglade plutoniumhärdar. Detta kan begränsas genom användande av flytande bly-vismut som kylmedel i stället för flytande natrium. Reaktorn bör då omges med en neutronreflektor av stål. I snabba bridreaktorer gäller däremot under vissa betingelser det motsatta förhållandet att bly-vismut ger högre voidkoefficient än natrium.

Det lämpligaste förhållandet mellan bränslestavarnas diameter och avstånd är starkt beroende av ett flertal faktorer såsom reaktortyp, kylmedel och bränsle, och är möjlig att anpassa för de olika fallen så att en kombination av driftsäkerhet och effektivitet erhålles.

Det kan ifrågasättas huruvida det är realistiskt att transmutera teknetium, emedan de mängder som konsumeras är i samma storleksordning som nybildningen i det klyvbara materialet i härden. I vart fall kräver detta specialiserade härdar med mycket högt teknetiuminnehåll för att ge en väsentlig reduktion av teknetiummängderna.

Simulering av transmutation i en gaskyld acceleratordriven reaktor visar att transmutation är genomförbar med denna design, som dock har tämligen begränsad kapacitet. Utbränningen av bränslet begränsas av den maximala reaktivitet som härden kan laddas med och den effekt som acceleratorn kan leverera, och har beräknats motsvara 993 driftsdagar. Om nytt bränsle tillförs i intervaller istället för att allt bränsle byts på samma gång är en högre anrikning möjlig, och därmed en effektivare utbränning.

I spallationsmålet bildas radioaktiva isotoper av huvudsakligen polonium, vismut och bly. Efter ett års drift har aktiviteten nått ungefär 90 % av den maximala, eller 11000 TBq, eftersom den i sammanhanget viktigaste isotopen ^{210}Po nått jämvikt mellan sönderfall och nybildning vid en mängd av cirka 34 gram.

För en simulerad bly-vismutkyld acceleratordriven reaktor har vidare visats att andelen flyktiga, radiotoxiska ämnen som bildas domineras av kvicksilver-, jod- och bromisotoper, i synnerhet ^{194}Hg. Med anledning av dess livslängd (520 år) och fysikalisk-kemiska egenskaper så bör det läggas stor vikt vid att förhindra spridning till och kontamination av andra delar av acceleratoranläggningen.

Molybdenbaserade keram-metallkompositbränslen uppvisar en överlägsen värmeledningsförmåga, men många frågor kvarstår om hur väl de motstår strålning.

Valet av kapslingsmaterial står mellan olika rostfria specialstål, som alla uppvisar fördelar och nackdelar vad rör temperaturgreänser, strålningstålighet, mekanisk styrka och korrosionsbenägenhet. Den bästa kandidaten är för tillfället ett strålningsresistent stål betecknat CW15-15Ti, men eftersom alla dess relevanta parametrar ännu inte blivit bestämda kan detta komma att ändras.

En tänkt standardkonstruktion för acceleratordrivna reaktorer har 800 MW termisk effekt och en reaktortank av 17 meters höjd. Den ska i nödfall kunna kylas genom naturlig konvektion, och placeringen värmeväxlarna har därvid stor betydelse. Med dessa belägna i nedström (”downcomers”) planar temperaturen vid kylningsbortfall ut vid 996 K, vilket är inom toleransgränserna för reaktortanken. Med denna konstruktion behövs troligen ett sekundärt kylmedel med högre kokpunkt än vatten, exempelvis olja eller bly-vismut.

En alternativ, heliumkyld typ av transmutationsreaktor som studerats uppvisar mycket lovande egenskaper, i synnerhet ur säkerhetssynpunkt i och med att kärnreaktionen avstannar av sig själv om temperaturen överskrider 1800 K i bränsle respektive 1500 K i moderatorn.

TABLE OF CONTENTS

LIST OF APPENDICES

Attached on the CD-ROM-disc.

1. Johan Carlsson, Inherent Safety Features and Passive Prevention Approaches for Pb/Bi-cooled Accelerator-Driven Systems, Doctoral Dissertation, Royal Institute of Technology, Department of Nuclear and Reactor Physics, Stockholm 2003, ISBN 91-7283-470-6, TRITA-FYS 2003:7, ISSN 0280-316X, ISRN KTH/FYS/--03/7—SE
2. Per Seltborg, External Source Effects and Neutronics in Accelerator-Driven Systems, Licentiate Thesis, Department of Nuclear and Reactor Physics, Royal Institute of Technology, Stockholm 2003, ISBN91-7283-600-8, TRITA-FYS 2003:46, ISSN 0280-316X, ISRN KTH/FYS/--03:46--SE
3. Per Seltborg, Jan Wallenius, Kamil Tucek and Waclaw Gudowski, “Definition and application of proton source efficiency in accelerator driven systems”, Nuclear Science and Engineering 145 (2003).
4. J. Wallenius, Neutronic aspects of inert matrix fuels for application in ADS, Journal of Nuclear Materials, 320 (2003)
5. P. Olsson, I.A. Abrikosov, L. Vitos, J. Wallenius, Ab initio formation energies of Fe–Cr alloys, Journal of Nuclear Materials, 321 (2003)
6. J. Wallenius, C. Lagerstedt et al, “Development of an EAM potential for simulation of radiation damage in Fe-Cr alloys”, 11th International Conference on Fusion Reactor Materials: ICFRM-11, Kyoto, 7 12 December 2003
7. Per Seltborg and Jan Wallenius, Proton Source Efficiency for Inert Matrix Fuels in Accelerator Driven Systems, Sixth International Meeting on Nuclear Applications of Accelerator Technology Accelerator Applications in a Nuclear Renaissance – AccApp’03, June 1-5, 2003 • San Diego, CA
8. J. Carlsson and H. U. Wider, Safety Aspects of Larger Heavy Metal-Cooled Accelerator-Driven Systems, Sixth International Meeting on Nuclear Applications of Accelerator Technology Accelerator Applications in a Nuclear Renaissance – AccApp’03, June 1-5, 2003 • San Diego, CA
9. J. Carlsson, H. Wider, Comparison of Safety Performance of Pb/Bi-cooled Accelerator-Driven Systems for two heat-exchanger locations and two power levels, Annals of Nuclear Energy, 2003
10. C.H.M. Broeders, J. Cetnar, R. Dagan, W. Gudowski, A. Travleev, “On the Use of Existing High Enriched MOX Fuel in an Experimental ADS”, Sixth International Meeting on Nuclear Applications of Accelerator Technology Accelerator Applications in a Nuclear Renaissance – AccApp’03, June 1-5, 2003 • San Diego, CA
11. J. Cetnar, W. Gudowski, G. Domanska, Moderating Reflectors with Burnable Absorbers for Reactivity Swing Reduction in Small ADS, Sixth International Meeting on Nuclear Applications of Accelerator Technology Accelerator

Applications in a Nuclear Renaissance – AccApp’03, June 1-5, 2003 • San Diego, CA

12. J. Cetnar, J. T. Murgatroyd, C.H.M. Broeders, W.Gudowski, R. E. Sunderland, R. Dagan, M. Schikorr, A. Travleev, “Reference Core Design for a European Gas Cooled Experimental ADS”, Sixth International Meeting on Nuclear Applications of Accelerator Technology Accelerator Applications in a Nuclear Renaissance – AccApp’03, June 1-5, 2003 • San Diego, CA

13. Daniel Westlén, Jerzy Cetnar, Waclaw Gudowski, Study on Transmutation Assembly Performance in the Gas-Cooled XADS, Sixth International Meeting on Nuclear Applications of Accelerator Technology Accelerator Applications in a Nuclear Renaissance – AccApp’03, June 1-5, 2003 • San Diego, CA

14. C.H.M. Broeders, J. Cetnar, R. Dagan, W. Gudowski, A. Travleev, “On the Use of Existing High Enriched MOX Fuel in an Experimental ADS”, International Workshop on P&T and ADS Development, October 6-8, 2003 SCK•CEN, Mol, Belgium

15. Kamil Tucek, Janne Wallenius, and Waclaw Gudowski, “Coolant Void Worth in Fast Breeder Reactors and Accelerator-Driven Transuranium and Minor-Actinide Burners “, Annals of Nuclear Energy, 2003

ABBREVIATIONS AND ACRONYMS:

EUROPEAN PROJECTS:

ADOPT	“Thematic Network on Advanced Options for Partitioning and Transmutation.”
CONFIRM	"Collaboration On Nitride Fuel Irradiation and Modelling"– shared cost project
FUETRA	“Fuel for Transmutation” – cluster of nuclear fuel related EU-projects
FUTURE	“Fuels for transmutation of long lived radiotoxic elements"– shared cost project
ITEM	“Network - Development of multiscale modelling for simulation of radiation effects for Virtual Test Reactors (VTR).
MOST	“Network - Review and revaluation of Molten Salt Reactor technology and previous realizations or projects.”
MUSE	"Experiment for Subcritical Neutronics Validation - MasUrca Subcritical Experiment"– shared cost project
PDS-XADS	“Preliminary Design Studies of an eXperimental Accelerator Driven System” – shared cost project
SPIRE	SPallation and IRradiation Effects - "Irradiation Effects in Martensitic Steels under Neutron and Proton Mixed Spectrum" – shared cost project
TECLA	“Technologies, Materials and Thermal-hydraulics and Safety for Lead Alloys” – shared cost project
TETRA	Technology for Transmutation – cluster of EU-projects

OTHER ABBERVIATIONS AND ACRONYMS

ADS	Accelerator Driven (Transmutation) System
ALMR	Advanced Liquid Metal Reactor
ANSALDO	Italian electromechanical company, Ansaldo Nucleare is a part of this company
BA	Burnable Absorber
BCC	Body Centered Cubic - type of a crystallographic lattice
BOL	Beginning of Life

BOC	Beginning of Cycle
BR	Breeder Reactor
CAPRA	Consommation Accrue de Plutonium dans les Rapides – Enhanced Burning of Plutonium in Fast Reactors
CERCER	CERamic-CERamic – type of nuclear fuel
CERMET	CERamic-METallic – type of nuclear fuel
CFD	Computational Fluid Dynamics
CR	Control Rods
DB-MHR	Deep Burn Modular Helium Reactor
DF	Driver Fuel (for the high temperature gas cooled reactors)
DIF3D	The multigroup steady state neutron diffusion and transport code
DLC200	Nuclear Data Library release following the standard version of the MCNP-code
DPA	Displacement Per Atom
EAF99	European Activation File, version 99. Nuclear data file containing neutron activation cross-sections
EAM	Embedded Atom Method
EBR	Experimental Breeder Reactor
EFPD	Effective Full Power Days
EM10	type of ferritic steel
ENDFB	Evaluated Nuclear Data File, suffix indicates a version of the file e.g. ENDFB6.8
EOC	End of Cycle
EOF	End of Life
ERMT	European Research on Materials for Transmutation Workshops
FAE	Fuel Adjacency Effect
FBR	Fast Breeder Reactor
FCC	Face Centered Cubic - type of a crystallographic lattice
FCTT	Fuel Cladding Transient Test
FFTF	Fast Flux Test Facility
FTF	Flat-to-Flat, a core design strategy
FZK	Forschungszentrum Karlsruhe

GENEPI	High intensity neutron generator, external neutron source for MUSE experiments
GeV	Giga-electron-Volt, energy unit
GWd	GigaWatt day, energy unit
HfN	Hafnium Nitride
HTGR	High Temperature Gas Cooled Reactors
HM	Heavy Metal
HT-9	High quality stainless steel
H451	Symbol of the nuclear-grade graphite
ISOTX	A format of string/representing of multigroup data neutron cross-sections
ITU	Institute of Transuranium Elements, Karlsruhe
JEF	Joint Evaluated (Nuclear Data) File, suffix indicates a version of the file e.g. JEF2.2
JENDL	Japanese Evaluated nuclear Data Library, suffix indicates a version of the file e.g. JENDL3.2
keV	kilo-electron-Volt – energy unit
KCODE	A MCNP module for k_{eff} (eigenvalue) calculations
KMC	Kinetic Monte Carlo
LA150	Nuclear data cross section library up to 150 MeV for the MCNPX-code, standard release of the Los Alamos (LA) National Laboratory
LBE	Lead Bismuth Eutectic
LOCA	Loss of Coolant Accident
LOF	Loss of Flow
LOHS	Loss of Heat Sink
LWR	Light Water Reactor
MA	Minor Actinides
MASURCA	Fast reactor at Cadarache, hosting MUSE-experiments
MCB	Monte Carlo based computer program for burnup calculations
MCNP	Monte Carlo Neutron Photon transport code
MCNPX	Monte Carlo Neutron Photon and Light Ion transport code
MC^2	A computer program for nuclear data evaluation and multigroup structure derivation
MeV	Mega-electron-Volt, energy unit

MHTGR	Modular High Temperature Gas Cooled Reactor
MOX	Mixed Oxide (fuel)
NEA	Nuclear Energy Agency
NJOY	A computer program for processing evaluated nuclear data files
NNC	NNC Holdings Limited, an international engineering support company, participant of the PDS-XADS Project
P/D	Pitch to Diameter ratio
pcm	pro centimille, a reactivity unit equal to 10^{-5}
PPS	Plant Protection System
PRISM	Advanced fast reactor concept
P0, P1	Approximation symbols of the nodal transport theory
RSC	Reserve Shutdown Control Rods
SA, S/A	SubAssembly (of the nuclear fuel)
SAS4	Reactor kinetic calculation code
SAS/DIFF-K	Reactor kinetic calculation code system
SNR300	SNR, Schneller Natriumgekühlter Reaktor - fast sodium-cooled reactor, the German fast breeder reactor prototype of 300 MW power
SS	Stainless Steel
SSC	Sing-Sing Core, an accelerator driven system concept of KTH
STAR-CD	Computer program for fluid dynamics problems
TF	Transmutation Fuel (for the high temperature gas cooled reactors)
TOP	Transient Overpower
TRADE	Triga Acclerator Driven Experiment, ADS-related experiment in Italy
TRISO	Triple isotropic coated fuel particles, fuel particles for gas cooled high temperature reactor
TRU	TRansUranium elements
TWODANT	A deterministic neutron transport code
UREX	URanium and fission products Extraction, nuclear fuel reprocessing technology
UTOP	Unprotected Transient Overpower
VARIANT-K	A Nodal transport and diffusion module for the DIF3D
WP	Workpackage

1 INTRODUCTION

Primary goal of partitioning and transmutation technology is to limit radiotoxic inventory of nuclear wastes destined to geological repository.

The research programme in accelerator-driven nuclear transmutation at the Department of Nuclear and Reactor Physics of the Royal Institute of Technology in Stockholm is focused on safety aspects of transmutation systems. In order to cover this broad and complicated topic and to harmonize our activities with international projects in which we actively participate, our research has put emphasis on the following major working areas:

- ADS system studies, in particular design of high-performance ADS-cores and analysis of their parameters. Safety studies focused on kinetics and dynamics of ADS, emergency cooling systems, radiation stability of materials and development of advanced fuel for ADS
- Development of simulation tools and nuclear data libraries necessary for advanced ADS-simulations
- Participation in ADS-related experiments, with a special attention to important components of ADS (e.g. construction of the spallation target)

2 ADS SYSTEM STUDIES

A number of innovative reactor systems for transmutation of plutonium and minor actinides were proposed in last decades. Fuels utilized in these reactors have low uranium content or are completely U-free. The presence of americium leads to a decrease in Doppler reactivity coefficient and delayed neutron fractions, raising significant safety concerns. It was therefore suggested that sub-critical accelerator-driven systems (ADS) should be implemented in fuel cycles involving recycling of minor actinides. Additional reactivity margin is hence provided, limiting the influence of reactivity coefficients and allowing steady-state operation of the system.

Accelerator-driven reactors are usually conceived to operate on fast neutron spectrum to avoid further build-up of minor actinides during irradiation. To maintain the fast spectrum, two types of coolant candidates can be considered – liquid metals (Na, Pb/Bi, Pb) and gases (He, CO_2).

In recent years, work has been under way on the design of lead-bismuth and helium cooled sub-critical transuranium ADS burners at the department [1]. In the case of lead-bismuth cooled system (Sing-Sing core concept), we identified a potential for rapid reactivity excursions of the reactor following loss of coolant from the core, which may lead to fuel failure and core disruption.

In this chapter, we first summarize premises and results of parametric, scoping study investigating coolant void worth for several model fast breeder reactors and accelerator-driven systems. We identify a set of fuel and core design parameters minimizing conceivable reactivity insertion in the standard set of design basis accidents. Thereafter, we discuss neutronic and burnup characteristics of helium cooled TRU ADS burner. Finally, we mention some results obtained in the frame of PDS-XADS project, a part of the 5th EU framework program.

2.1 PARAMETRIC DESIGN STUDIES OF ACCELERATOR-DRIVEN TRANSURANIUM AND MINOR-ACTINIDE BURNERS

In our recent study [2], we analysed coolant void reactivity as a function of fuel composition and core geometry for series of fast breeder and accelerator-driven system configurations. First, scoping studies of Δk_∞ were performed in two-dimensional pin lattices for several fuel compositions and wide range of pitches. Then, we investigated the coolant void worth in various types of model critical & ADS transmutation systems, employing nitride and oxide fuel, different types of inert matrices and two types of coolants - lead/bismuth and sodium. Void reactivity was studied as a function of core geometry parameters as e.g. reactor lattice pin pitch and fuel pin design. The optimal pin pitch was then identified for each configuration. Finally, we discussed the implications of our results for ADS core design in general.

We found that reactor cores with high minor actinide content fuel exhibit generally higher void worth than cores fueled primarily with plutonium. A disadvantage of sodium versus lead/bismuth in terms of larger positive coolant void worth is apparent for all transmutation type fuels investigated.

For an FBR with $(U,Pu)O_2$ fuel, on the contrary, Pb/Bi yields larger void worth than sodium when $P/D \geq 1.4$. While in sodium cooled FBRs the negative reactivity is introduced upon coolant voiding by both increase of neutron capture in structural material and coolant (in the reflectors and plena), in Pb/Bi-cooled reactors the reactivity contribution is negative only from the former.

We further show that in lead/bismuth-cooled systems, a radial steel pin reflector has to be applied, if coolant void worth is to be significantly reduced.

Enlarging the pitch-to-diameter ratio lowers the coolant void worth in ADS burners operating in two-component scenario, while ADS burners with MA based fuel should be designed with minimum allowable P/D.

Pins with small diameters and non-absorbing fuel matrices are preferable with respect to the coolant void worth. However, even an application of strongly absorbing matrix (HfN), does not have to deteriorate the void worth critically; large amount of negative reactivity still being introduced into the reactor upon voiding both core & upper plenum, as e.g. in TRU-fueled ADS.

2.2 A GAS COOLED ACCELERATOR-DRIVEN TRANSMUTATION SYSTEM

2.2.1 Designing a gas cooled transmutation core

The liquid metal coolant used in the Sing-Sing core design has a moderating effect on the neutrons decreasing the theoretical upper limit of transmutation efficiency. We are interested in examining the consequences of hardening the neutron spectrum further. This may be achieved by using helium coolant, minimizing the neutron moderation.

During the last year, work has been underway aiming at designing a gas-cooled ADS burner, which meets the safety requirements while showing better transmutation efficiency than the Sing-Sing core. Similarly as in the Sing-Sing core, we use uranium free plutonium-americium-curium fuel.

2.2.2 Achieving decay heat removal at ambient pressure

In conventional fast reactor designs, achieving a high breeding ratio has been the primary concern. Consequently, the reduction of neutron leakage has been an important design parameter. In contrast, uranium free fuels dedicated to waste transmutation feature a neutron surplus that may be used to improve transmutation performance and core safety.

The core height is designed to minimize the axial power peaking factor. This leads to axial neutron leakage, which however may be afforded due to the excellent neutron balance caused by the plutonium rich fuel.

Our main design criterion has been the avoiding of severe consequences in the case of a loss of pressure accident. By increasing the coolant fraction, the working pressure may be lowered, minimizing the consequences of loosing core pressure. In order to achieve reasonable burnup rates, we adopt an average power in the hottest pin equal to 36 kW/m for the design work. It was required that the corresponding decay heat (1.8 kW/m) should be possible to remove at ambient pressure and a coolant velocity of 70 m/s.

2.2.3 Core design

In an ADS design with hexagonal fuel bundles, the choices for hexcan flat-to-flat (FTF) are dictated by the space occupied by the spallation target. In the present study, we adopt a spallation target radius of 21.4 cm being a compromise between heat removal capacity and proton source efficiency. Assuming the seven central assemblies were removed to make room for the target, we arrive at an outer FTF of 185 mm. For a given pin pitch to diameter ratio (P/D), there are only discrete values of pin diameters possible. Details of a core geometry are given in Table 2.1

P/D equal to 2.0 gives a good trade off between the neutronic and thermo-hydraulic boundary conditions. The cladding temperature at one atmosphere for a decay heat power of 1.5 kW/m with P/D=2.0 is displayed in Figure 2.1. At a pin diameter of 7.8 mm, P/D=2.0 is sufficient to keep cladding temperature below the rapid burst limit of 1330 K for austenitic steels. To stay conservative, we do not let the cladding temperature rise over 1300 K.

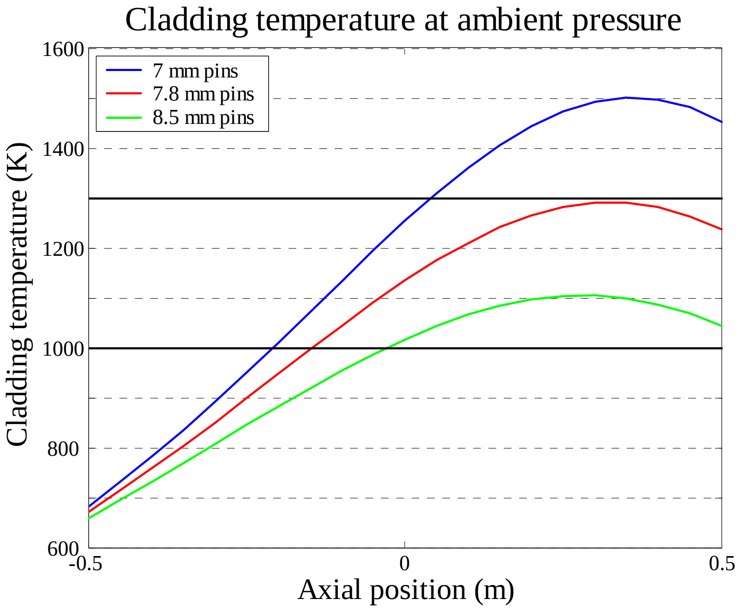

Figure 2.1: During a loss of pressure accident, the cladding temperature does not rise over the rapid burst limit of 1330 K elvin at ambient coolant pressure.

The pin diameter chosen is a trade-off between burnup and working pressure. At a constant pin linear power, increasing the pin diameter leads to better cooling, meaning that a lower working pressure is needed. Consequently, the increase in temperature during a loss of pressure transient is smaller. However, the power density is also decreased implying lower transmutation ratios.

Having fixed P/D, we may calculate the core working pressure. A lower limit is given by the hottest pin upper temperature limit set to 1000 K. In order to assure sufficient cooling of this pin, the helium pressure must exceed 4.3 MPa, see Figure 2.2.

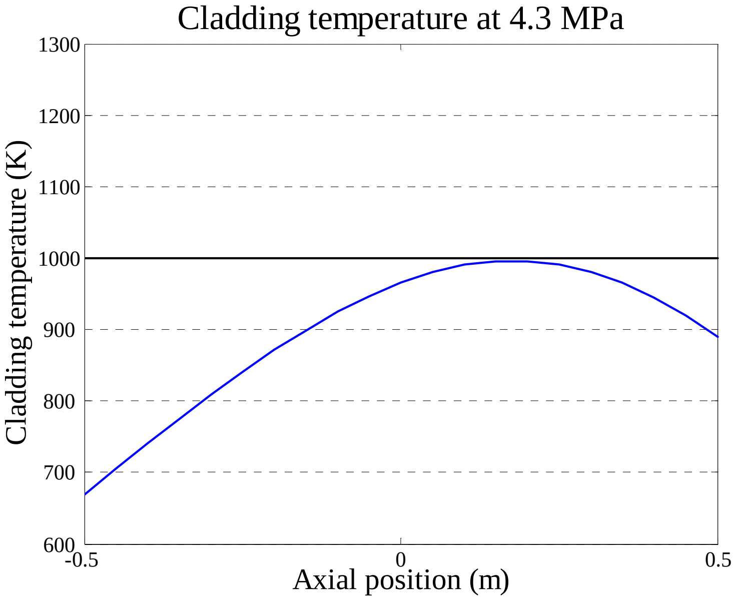

Figure 2.2: At normal operation a working pressure of 4.3 MPa is required to assure sufficient cooling.

In the beginning of the fuel cycle (BOC), the highest linear power in a fuel rod is 45 kW/m. Allowing a maximum radial power peaking of 1.3 and a maximum axial power peaking of 1.24, this means the average pin linear power is 27.9 kW/m giving a total core power of 566 MW_{th}.

We summarize the thermal characteristics of the core in Table 2.1.

Table 2.1: Core thermal hydraulics

Total core power	566 MW_{th}
Average linear power	27.9 kW/m
Operating pressure	$4.3 \cdot 10^6$ Pa
Coolant flow speed	70 m/s
Max cladding temperature – operation	1000 K
Max cladding temperature – accident	1330 K

2.2.4 Fuel composition

There are 120 fuel assemblies in the core. We select nitride fuel because of its high power to melt and the relative ease of reprocessing. An inert matrix is required to stabilize the fuel at high temperatures. Tests of (Pu,Zr)N fabrication have shown that a solid solution can be obtained for matrix fractions in the order of sixty atomic percent.

We keep the ZrN fraction of the fuel constant at a level of 60% in the entire core and adjust the Pu/MA ratio in the fuel to obtain a k-eigenvalue of 0.97 at BOL. The actinide vector adopted corresponds to the spent MOX-fuel composition as shown in Table 2.2.

Table 2.2: Composition of the fuel heavy metals

Element isotope compositions used

^{238}Pu	5.1%	^{241}Am	66.6%
^{239}Pu	37.9%	^{243}Am	33.4%
^{240}Pu	30.3%		
^{241}Pu	13.2%	^{244}Cm	87.3%
^{242}Pu	13.5%	^{245}Cm	12.7%

In order to minimize the radial power peaking, the core has been divided into four fuel zones each with a unique Pu/MA composition.

The contribution of neptunium to the radiotoxic inventory of spent LWR fuel is less than the radiotoxicity in natural uranium (20 mSv/g) and is hence not significant. For this reason, we chose not to include neptunium in our transmutation strategy. Enriched nitrogen-15 has been used in the fuel to avoid the production of ^{14}C. The ^{15}N content is taken as 99.5 percent. The fuel porosity was assumed to be 15 percent to allow for solid fission product swelling. Gaseous fission products and helium are expected to be released into the gas-plenum.

2.2.5 Neutronic parameters

Some neutronic parameters have been calculated. The coolant void coefficient is a measure of the reactivity effect of loosing the helium pressure. This was calculated in two subsequent MCB-runs, the first one with normal He-density, and the second with the He-density at ambient pressure. The calculations show the k-eigenvalue increase by 870(±40) pcm at a pressure drop accident.

Another important neutronics parameter is the k-eigenvalue response to a temperature change. We calculated this by comparing the k-eigenvalues at fuel temperatures of 300 K and 1800 K. The difference was calculated to -0.02(±0.01) pcm per Kelvin temperature increase.

Delayed neutrons are a very important for the controllability of reactors. Thus deciding the delayed neutron content and the amount of fissions induced by delayed neutrons is important. Two measures are of interest concerning delayed neutrons. β expresses the reactivity delayed neutrons would insert if they would have the same energy spectrum as fission neutrons have. β_{eff} is the reactivity effect actually caused by delayed neutron induced fissions. The resulting β has been calculated to 240(±21) pcm and β_{eff} to 138(±21) pcm.

2.2.6 Fuel cycle

For safety reasons, we do not allow the accelerator current to increase more than a factor two during the fuel cycle. With a k-eigenvalue of 0.97 in the beginning of the fuel cycle, this leads to a k-eigenvalue of 0.94 in the end of the cycle. This sets the cycle length. In order to avoid refueling and reprocessing, we suggest using the same fuel for several fuel cycles, raising the k-eigenvalue by altering the reflector. In the first cycle, we will use boron assemblies next to the outer most fuel assemblies. The k-eigenvalue may be raised by replacing boron assemblies for reflecting steel assemblies. This way it is possible to burn the same fuel for at least five cycles after which the radiation damage to the fuel cladding limits burnup.

The burnup is limited by radiation damage to the cladding material. After 1400 days of full power operation the highest dose received by the cladding anywhere in the core is 170 dpa. At this time, 21.2 percent of the original actinide mass has fissioned.

2.2.7 Results

Preliminary calculations show that we may go as far as P/D = 2.6 before it is impossible to maintain reactor in operation. There are several reasons not to go that far though. Mainly, it becomes problematic to maintain constant criticality in the system. The higher the Pu content, the faster criticality drops. Long periods of constant criticality reduce the need for reprocessing of the fuel and are thus beneficial for actinide burnup.

At a P/D ratio of 2.0, a fuel pin diameter of 7.8 mm is sufficient to assure decay heat removal at ambient pressure for a 566 MW_{th} core. With this design, a working pressure of 4.3 MPa is sufficient during normal operation.

Keeping the radial and axial power profiles of the core as flat as possible is important since there is an upper limit to the local power production. With power peakings small, the total power may be higher implying better transmutation efficiency. We have been looking for the optimal Pu-fraction in the different zones in both a three and four fuel zone strategy. It shows that with a three-zone strategy it is hard to achieve a radial power peaking lower than 1.4. However, with a four-zone strategy, 1.2 is achievable. Apart from finding as flat a power profile as possible, we have also chosen the Pu-concentrations to give a k-eigenvalue of 0.97 at BOC. In each case the fraction of the heavy metals in the fuel not consisting of Pu is 5/6 Am and 1/6 Cm.

The fuel assembly row closest to the spallation target consists of twelve fuel assemblies with the lowest plutonium content equal to 28 atom-percent, while the minor actinide content is quite high. The next core region (zone 2) constitutes of 18 assemblies. These are more reactive, containing 34 percent Pu, compensating for the lower neutron flux in this region. Zone three is the largest with 54 assemblies containing 45 percent Pu. The furthest away from the spallation source (zone 4) there is a filled row of 36 assemblies, where the Pu content is as high as 99.5 percent. With 169 fuel rods in each assembly, this gives a total of 20280 fuel rods in the core.

The neutronic parameters of the core have been calculated in accordance with Table 2.3.

Table 2.3 : Neutronic parameters

Neutronic parameters		St. dev.
Void coefficient	873 pcm	36 pcm
Temperature feedback	-0.02 pcm/K	0.01 pcm/K
β	240 pcm	21 pcm
β_{eff}	138 pcm	21 pcm

In 1400 days 21.2 percent burnup is reached.

2.2.7.1 Conclusions

The excess of neutrons in a plutonium fueled fast reactor may be used to increase the pin pitch to diameter ratio. By doing this it is possible to design a gas cooled fast core where cooling is sufficient even during a severe loss of pressure accident, while maintaining a high burnup.

2.3 A GAS COOLED CONCEPT OF THE PDS-XADS CORE

A gas cooled Accelerator Driven System has also been investigated in details in the frame of the European Project “Preliminary Design Studies of the eXperimental Accelerator Driven System” – PDS-XADS. This work has been performed as a joint effort of KTH Stockholm and UMM Krakow.

2.3.1 Assessment of the Possibility to Adopt Special Assemblies with MA and LLFP in the Gas-Cooled XADS Core

A possibility of introducing tailored assemblies for the transmutation of minor actinides (MA) and long-lived fission products (LLFP) into the gas-cooled XADS core in order to demonstrate the feasibility of ADS for waste transmutation has been investigated. Apart from that short-term goal also a long-term goal that is the transmutation demonstration with a large number of MA-based fuel assemblies (phase 2) is being discussed.

Several studies have been done on ADS demonstration for waste transmutation, but their constraints have been taken in a simplified way for:

- Fuel behaviour (thermal constraints and gaseous releases)
- Reactivity feedbacks (and reactivity margins required for a safe design)
- Size of the plant(to provide substantial transmutation efficiency and accepted reactivity coefficients)

Similar thermal conductibility as the MOX pin can be provided using a MA/Pu fuel pin (Oxide on MgO matrix) with adjusted Fuel/MgO ratio. For the feasibility demonstration the adopted limited number of MA subassemblies will keep reactivity coefficients not significantly changed.

In order to demonstrate the transmutation capabilities of the XADS core, a different approach should be taken with more issues need to be considered. The main problem concerns introduction of a positive contribution to the Doppler coefficient when substantial amount of MA is loaded. Other important issue is concerned with discrepancies in cross section data that can lead up to 4000 pcm difference in criticality level, what further can be increased due to calculation uncertainties of neutron transport methods (Monte-Carlo versus deterministic). Those problem need to be strongly addressed and investigated in the near future. Possible ways of dealing with that problem were discussed.

As for the near term goal several different assembly designs and geometrical core arrangements have been studied. The actinides have been placed in the same fuel elements as adopted for the reference core. These have been placed in the core centre, located close to the spallation target where they receive as high a fast neutron flux as possible.

Transmutation performance of ^{99}Tc and ^{129}I has been studied in the assemblies having a different design than the actinide assemblies. Since efficient transmutation of the long-lived fission products ^{99}Tc and ^{129}I requires an intense thermal flux, only one large rod is used in each assembly with its centre filled with graphite as a moderator. It turned out that graphite shows better performance than zirconium hydride. The FP assemblies have been placed in the periphery of the core for two reasons: to utilise neutrons that are leaking from the core and to avoid moderating of neutrons in the core. It was shown that the introduction of these tailored transmutation assemblies is possible without violating core design parameters such as linear power, accelerator current, radiation damage or linear power.

An actinide vector consisting of plutonium and americium (40/60 atom fraction) was used in the actinide assemblies. The composition is actinide oxide with the oxygen content of 1.93 oxygen atoms per atom heavy metal. Magnesium oxide is used as matrix for the transuranium oxides. The MgO constitutes sixty percent of the final volume. It is chosen mainly because of its rather high thermal conductivity (8 W/(K·m)) and because of its high melting temperature.

The plutonium vector corresponds to the plutonium from MOX-fuel, which has cooled for seven years. The relation between plutonium and americium is chosen to the equilibrium composition reached after many recycles in a transmutation system

To assure an intense fast flux, the MA special assemblies are placed in the core centre as close as possible to the spallation target.

The burn-up calculations were performed using the Monte Carlo Continuous Energy Burn-up code – MCB [4]-[7], with an extensive temperature dependent cross section library that is included in the MCB system. For the most isotopes the neutron transport cross sections of JEF2.2 were used whereas for isotopes of lead JENDL3.2 was adopted. The system gets also support from activation cross section library that is based on EAF99 data. MCB allows for a complete treatment of fuel burn-up, distributed on twenty-three axially divided burn-up cells. The transport calculation is performed on fully heterogeneous geometry model on the level of fuel pins. Introduction of S/A with MA reduces the reactivity swing due to the burnup allowing for irradiation over 3-year period of full power without refueling.

The design limit for radiation damage is 150 dpa. This criterion potentially limits the length of the irradiation periods and also the system lifetime. The calculated cycle average peaking values of about 10 dpa/year would allow for irradiation over 15 years of full power.

The linear power distribution has been calculated to ensure that the design constraint of 25 kW/m is preserved. The peak linear power in MA pins are 20 kW/m and it remains below that limit. The power profile remains rather constant during the entire cycle. This is due to compensating effects; increasing beam power compensates burn-up of the fuel.

Several different technetium loads have been tested for the FP special assemblies. Due to smaller neutron flux suppression, the thinner, the technetium shell is made, the higher the relative transmutation efficiency gets. However, the absolute amount of technetium transmuted decreases sharply with decreasing technetium load. In order to find the optimum design we should consider other parameters of nuclear waste treatment. Most of all the effort of reprocessing the rods is an important issue. In a situation where reprocessing is difficult (*expensive*), high relative transmutation is desirable. When reprocessing is a simple task (*cheap*), a high absolute transmutation becomes more important. It should be noted that only a tiny fraction of the technetium is transmuted in the case where 50% of the rod volume is FP. Only 63 grams out of 3.4 kg are destroyed when the technetium content is that high.

The obtained transmutation ratios show that some isotopes are transmuted rather efficiently in the transmutation assemblies with the exception for ^{238}Pu, ^{242}Pu and ^{242m}Am, which are being accumulated. However, for most isotopes, six special MA assemblies are not enough to compensate for the build up of those isotopes in the core fuel. In order to obtain an efficient transmutation a reduction of fertile material ^{238}U will be required what means an increment of MA fraction.

Actinide transmutation could be demonstrated in the XADS core. However the masses possible to transmute in this facility are small. For the technetium transmutation the situation looks worse. Even with a large introduction of technetium, the build-up in the driver fuel will be in the same order of magnitude as the actual destruction. In fact also for most actinide isotopes, the build-up in the fuel is larger than the transmutation in the special assemblies. Large-scale transmutation will require dedicated cores with far higher contents of the nuclei to be transmuted. In addition, the neutron fluence should be significantly higher in order to achieve high transmutation efficiencies. However inserting special transmutation assemblies into the XADS may show valuable for demonstrating technology.

For details look into Appendix 13

2.3.2 Core Reference Cycle Analysis for the Gas-Cooled XADS

Performance of XADS core in fuel cycle is strongly influenced by the definition of core configuration and the refueling approach whether we assume single or multi-batch refueling. A three batches refueling of gas-cooled XADS core was proposed by NNC to meet peek pin burnup at targeted level of 40GWd/Tme. This option leads to an equilibrium stage when a new fuel cycle replicates its performance pattern from the previous cycle. In the equilibrium cycle the fuel enrichment and the reactor core criticality level are to be controlled by the length of the cycle period not only at the end of life (EOL) as it is in the single batch cycle but also at the start of life (SOL). It makes this option more complex than the single batch refueling one and brings more uncertainty to the design and making it more sensitive to the embedded nuclear data uncertainties. Yet, an introduction of fuel shuffling would further increase its complexity. Therefore the two options were carefully examine in order to better understand the physics of XADS thus increasing its safety. The application of different design tools can allow us to learn more about sources of the uncertainties and to make a better choice of designed parameters like fuel enrichment, cycle length or fuel shuffling pattern. Fuel cycle analysis has been performed by a Monte Carlo approach using the MCB system and compared to the results of deterministic calculations based on ERANOS code system.

The cycle length is limited by the criticality of 0.97 at SOL and by the current of 5mA at EOL. In the MCB burn-up calculation in single batch cycle the limiting current occur after cycle length of 993 full power days.

Time derivatives of the criticality and proton current have following values:

$$\frac{dk}{dt} = -3.092\ pcm/day$$

$$\frac{dI}{dt} = 2.610\,\mu A/day$$

They are a few percent lower than in deterministic calculation that partially can be explained by differences in enrichments to produce required criticality at SOC in both methods.

Three-batch cycle requires higher fuel enrichment than in single batch case that could raise the criticality above unity when the whole core is loaded with the fresh fuel. Therefore in pre-equilibrium state a few sub-assemblies must be voided to keep the criticality within its constraints. Simulation of pre-equilibrium phase was performed. Taking the cycle length value (limited by constrained burnup) around 620 days the resultant enrichment of 23.83% by volume of Pu+MA has been obtained by ERANOS/ECCO system. That enrichment gives us higher criticality levels while using MCB. To meet criticality constraints of 0.97 at SOC the cycle length had to be increased to above 800 days leading to an overflow the current level at EOL. Therefore the enrichment of fresh fuel had to be lowered in MCB model. The estimated value of 23.6% was used for detailed cycle analysis.

Time derivatives of the criticality and proton current at the equilibrium have following values:

$$\begin{aligned} \frac{dk}{dt} &= -3.17\ pcm/day \\ \frac{dI}{dt} &= 2.65 \mu A/day \end{aligned},$$

which is about 10% lower than values assessed in deterministic model but still slightly higher than in single enrichment case.

The power distributions that are to be used in thermo-hydraulic analysis were calculated on pin level at SOC and EOC of every batch in a search for peaking values.

Unsurprisingly the highest ratings occur in the first fuel subassembly surrouinding the spallation target, particularly at the EOC. In case of single enrichment pin form factor in hottest S/A is 1.035 and the overall (axial, radial and pin) form factor was found 1.705. For 3-batch case the largest pin from factor equals 1.072 but it does not occur in the hottest S/A. In the hottest S/A it is equal to 1.042 and the overall (axial, radial and pin) form factor is 1.759. Detailed power characteristics were presented for both refueling options. The 3-batch option presents only modestly worse power peaking and still remains in the range of feasibility.

Evaluation of reactivity coefficients was performed using single batch refueling. The results are presented in Table 2.4. Since the differences between the data at SOC and EOC are small there is no real need to calculate the data for the middle of cycle. If those data were required they can be obtained as the simple average of SOC and EOC results. All reactivity coefficients were calculated using full geometry model of XADS reactor prepared for MCB system with adequately modified relevant parameters. The coefficient for expansion of fuel pin concerns the actual physical expansion of the pin both in axial and radial direction with associated density dilution.

Table 2.4 Reactivity coefficients of Gas-cooled XADS in 1-batch cycle

Coefficient	Unit	SOC	EOC
Doppler feedback[1]	[pcm/^{o}C]	-0.33 ±0.004	-0.32 ±0.005
Fuel pin expansion	[pcm/^{o}C]	-0.326 ±0.016	-0.323 ±0.016
Diagrid expansion	[pcm/^{o}C]	-1.12 ±0.07	-1.11 ±0.07
Clad expansion	[pcm/^{o}C]	-0.04 ±0.03	-0.04 ±0.03
Wrapper expansion	[pcm/^{o}C]	-0.06 ±0.05	-0.05 ±0.05
Reflector and target expansion	[pcm/^{o}C]	-0.20 ±0.05	-0.24 ±0.05

2.3.3 Evaluation of Radiation Damage and Circuit Activation of the Gas-Cooled XADS

This task hes been concerned with evaluation of radiation damage and activation of the Gas-Cooled XADS over the fuel cycle. It includes evaluation of neutron flux and damage as well as activation and spallation products in target loop. Since the primary system is cooled by helium no activation of coolant will occur.

Calculation of DPA was preformed by using MCB code (which incorporates neutron transport modules of MCNP4C [3]) in a heterogeneous model of XADS reactor using damage energy cross section present in the neutron transport cross-section libraries of the MCB system. Cross section libraries from evaluated data files JEF2.2 supported for lacking nuclides of lead from JENDL3.2 were used in calculations. Cross section tables at power temperatures were applied. For assessing DPA values a conservative approach was applied as follows:

DPA = Ea / 2Ed,

where Ea is available damage energy calculated from damage energy cross section and Ed is threshold displacement energy of 40eV for main steel components: Fe, Cr, Ni. The conservative approach in calculation of DPA was employed here due to neglecting

---

[1] Doppler feedback originates from a temperature enhancement of neutron capture cross sections

in current assessment the damage effects that occur due to recoil of atoms in case of their alpha decay which process can add about 15 % to DPA obtained from recoils after direct kinetic interaction with neutrons.

The results obtained for SOC and EOC in single batch cycle show that peak damage on cladding equals 9,7 dpa/year at SOC and it slightly grows to 10,6 dpa/year at EOC.

Activation of target loop is dominated by the nuclides produced with core flux neutron. Predominant here are ^{210}Po, ^{210}Bi, ^{209}Pb, ^{207}Bi and ^{210m}Bi.

The overall activity after 1 year of full power is about $1.1*10^{16}$ Bq and it grows modestly after that time since ^{210}Po reached its equilibrium. The peak value could be about 10 % higher if irradiation time will be extended to 10 years. Quoted values refer to full power operation. If the beam availability were 50% the activity at equilibrium would be also 50% of that for full power. The accumulated mass of ^{210}Po, the most hazardous nuclide is about 34 grams and poses a risk for intake of $6.8*10^{17}$Sv.

2.4 PDS-XADS LBE-COOLED CONCEPT CORE DESIGN

2.4.1 Assessment of the Possibility to Use Existing Highly Enriched MOX Fuel

Burnup modeling with MCB system for XADS with SNR300 fuel were performed in order to make a comparison with results obtained when using a deterministic method. Applied model was simplified by the homogenisation of the assemblies since this is generally required by the deterministic code. The system evolution over 3 years period was assessed while using the JEF2.2 cross-section libraries and power temperatures 1200K for fuel and 900K for target. Important parameters that characterize the core performance like k_{eff}, k_s, source effectiveness, reactivity loss and nuclide transmutations were obtained and then compared with the results obtained by multi group deterministic method based on FZK KAPROS/KARBUS system. The external source multiplication factor – k_s is slightly higher than the actual reactivity or effective neutron multiplication factor - k_{eff} implying the source effectiveness greater than one. The criticality level and its time evolution remain in a margin of 300 pcm that can be considered a good agreement taking into account the differences in the compared calculation system. The nuclide density evolutions show reasonable agreement for uranium and ^{239}Pu and ^{240}Pu whereas for nuclides with more complex transmutation chains the differences in transmuted mass calculated in both approaches show larger differences. This effect can be caused firstly by the differences in the cross section applied and furthermore by the differences in the applied neutron transport methods. Nuclides that are being reduced in mass are ^{238}U, ^{239}Pu, ^{235}U and ^{241}Am. Other nuclides of plutonium are being build-up, what reduces to some extent the pace of the reactivity swing. See Appendices 10 and 14 for details.

2.4.2 Neutronic Source Characterization of the LBE-Cooled XADS - Evaluation of the Relationship between Multiplication Factor and Intrinsic Core Criticality

The process of neutron multiplication in fissionable systems can be quantitatively described with a few different parameters depending on their physical meaning as well as their applicability constrained by the system criticality. Special attention has been paid to the applicability of derived parameters to the Monte-Carlo simulations of subcritical ADS. A definition of k-source - k_s – has been introduced as a ratio of neutron production to losses averaged over the neutron flux from the fixed source. This is a straightforward extrapolation of the definition of the eigenvalue k-effective - k_{eff}. Substitution of the neutron flux in eigenstate with the flux in the source problem leads to following:

$$k_{eff} = \frac{\left\langle \boldsymbol{F} \phi_0 \right\rangle}{\left\langle \boldsymbol{A} \phi_0 \right\rangle} \tag{2.1}$$

$$k_S = \frac{\left\langle \mathbf{F} \phi_S \right\rangle}{\left\langle \mathbf{A} \phi_S \right\rangle} \tag{2.2}$$

An alternative formula for k-source was derived, that can be useful to calculate k-source in terms of the total number of fission neutrons born in the system per one source neutron or by using the estimators of production and loss terms due to various events, which are readily available from MCNP. This approach has an advantage for MCNP users because it does not require a direct specification of the source term since the system assesses it using the balance equation. The physical meaning of derived definition is discussed in the document.

A direct extrapolation of the k-eigenvalue definition in the eigenvalue problem for the fixed source problem leads to an unambiguous definition of k-source that has a clear physical meaning in terms of fission neutron multiplications. The presented approach allows the user of MCNP code for application of a convenient formulas for calculation of k-source expressed by the parameters delivered by MCNP by default in the summary table of the output file. While the definition of the fixed neutron source still influences the value of k-source it is possible to avoid normalization problems by applying the equation in a source-free form.

2.4.3 Neutronic Source Characterization of the LBE-Cooled XADS - Evaluation of the Delayed Neutron Fraction

Special investigations have been performed to assess precisely a delayed neutron fraction in MCNP neutron transport simulation. It is possible using the current version –

MCNP4C, which uses cross section libraries taking into account, delayed neutron spectra. Taking advantage of this new feature one can assess β_{eff}, by taking the difference between the reactivity calculated with the prompt and delayed neutrons considered and the reactivity with only the prompt neutrons considered. This approach requires a fast calculation system in order to lower statistical fluctuation. The advantage of it is that the above approach follows the simulation path of neutron transport process as it is performed by MCNP code thus obtained results will reflect the one that served for evolution of the criticality level. The results obtained with JENDL3.2 and ENDFB6.8 are consistent whereas results based on JEF files show some kind of systematic bias. In a search for a reason of this bias we have checked both new and previous releases of the data files – respectively JEF2.2 and JEF3 as well as the Pb cross section (JEF files contain only cross section data for natural Pb). The difference between JENDL/ENDF and JEF results lowers a bit in the case of natural Pb but still in the range of one standard deviation. The version of JEF file does not make any difference.

The fraction of delayed neutrons - β - varies from 311 pcm to 351 pcm generally in the range of statistical uncertainty when different libraries are applied. The β_{eff} obtained varies from 295 pcm to 409 pcm. It can be greater or less than β depending on the applied library. This cannot be simply explained by the statistical fluctuations since both parameters are strongly correlated. Probably, different libraries vary in terms of delayed neutron spectra as well as Pb cross sections. The importance of the Pb cross section is visible when the JEF libraries are combined with the Pb cross section from JENDL. In such cases β_{eff} varies much bigger probably due to some incompatibilities between both libraries at this point. This needs to be investigated further concerning the procedure applied in MCNP.

Fluctuations of k_{eff} for different data libraries exceed significantly statistical level of fluctuations. As it was observed before, a relatively high k_{eff} value for ENDFB6.8 is caused by inelastic neutron scattering on lead. Special attention should be also paid for the difference in k_{eff} between JEF2.2 and JEF3. This difference may be caused by differences in Pb cross sections. In cases of applying delayed neutron spectra treatment in MCNP neutron transport calculations there is no need for correction due to β_{eff} of obtained values of reactivity and other neutron multiplication related parameters.

2.4.4 Core Reference Cycle Analysis for the LBE-Cooled XADS

The core cycle analysis was performed using the MCB system for two cases of fuel enrichments: the single enrichment and the dual enrichment. In the first case the Pu+MA enrichment was 23.5% (atomic fraction) where in the second case the inner S/A are filled with fuel enriched to 21.8% whereas the remaining ones with fuel enriched to 28,25%. The enrichment levels provide the criticality level at BOC close to 0.97 in both cases. Comparative analysis of obtained results shows that with the introduction of the dual enrichment fuel the core has:

a) higher Pu and MA load,

b) smaller reactivity and proton beam current change rate,
c) the radial form factor lowered by about 12% from 1.26 to 1.11.
d) the source neutron multiplication factor k_s ~ 500 pcm smaller than in the single enrichment case for the same level of criticality k_{eff}.

This also causes a lowering of the neutron source effectiveness below unity whereas it was above unity in the single enrichment case. This effect should not be considered disadvantageous since it leads to lowering the reactivity swing along the fuel cycle. The lower neutron source efficiency with the higher load increases fuel cycle length when permissible beam current level is limited. This however would be considered disadvantageous if one is focused on the transmutation efficiency since the longer fuel cycle with higher Pu and MA load results in lower transmutation efficiency for the thermal power constrained. Taking into account that XADS is dedicated for transmutation in special assemblies only the dual enrichment option can be a proper choice since it can maintain the criticality in required range for a longer time than in the single enrichment option.

Analysis of statistical fluctuation of neutron transport simulation in Monte-Carlo process was performed in order to quantitatively assess the statistical uncertainty that is added here to the results at EOC. Analysed parameters are: criticality, neutron multiplication, proton beam current, and transmutation rate of plutonium. The results show that the highest fluctuations occur for fission neutrons and the proton current (required to maintain constant power). This however does not propagate strongly to the ks and transmutation rates. It has been observed that statistical fluctuations are rather stable and showing even some decrease of its magnitude with increasing burnup.

2.5 INITIAL ANALYSIS OF SENSITIVITY TO CROSS SECTIONS FOR XADS AS MINOR ACTINIDE TRANSMUTER

The analysis of sensitivity to applied cross section in the XADS system design. Results of this analysis might be important for the long-term goal of ADS development for nuclear waste transmutation; that is, the transmutation demonstration with a large number of minor actinides (MA)-based fuel assemblies. A Monte Carlo burn-up simulation of the gas-cooled XADS, with a 50% homogeneous load of MA in the core, was performed using two major evaluated nuclear data files, JEF2.2 and ENDF/B-IV, in order to examine the sensitivity of the calculated criticality level and transmutation performance to the choice of library.

2.5.1 Calculation model

The burn-up calculations for this analysis were performed using the Monte Carlo Continuous Energy Burn-up code – MCB, with extensive temperature dependent cross section libraries that are included in the MCB system. In the first run we have used

JEF2.2 files with cross sections for isotopes of lead adopted from JENDL3.2 due to the lack of such cross sections in JEF2.2. In the second run, while using exactly the same system and calculation model, the ENDF/B-IV files were applied. The transport calculations were performed on a fully heterogeneous geometry model on the level of fuel pins, the same as was used for the gas-cooled XADS reference core with 90 fuel subassemblies. The composition of the heavy metal with a 50% load of MA actinide that was used in calculations is shown in Table 2.5. The core was divided into fifteen burnable regions; five in axial dimension times three in radial. An assumption of homogenous distribution of uranium, plutonium and MA fuel was made to simplify considerations. A five-year period of XADS system operation at full power of 80 MWth has been simulated.

In this initial analysis of fuel cycle and MA transmutations we focused on comparing calculation results of criticality and transmutation ratios of MA and plutonium, as well as their time functions, since these parameters and functions are strongly sensitive to the differences between the compared cross sections.

Table 2.5: Composition of the heavy metal in the fuel

Nuclide	Molar fraction	Total mass at BOC [kg]
^{235}U	0.0017	7.59
^{238}U	0.3383	1530
Total U	**0.34**	**1538**
^{238}Pu	0.00496	22.43
^{239}Pu	0.084	381.4
^{240}Pu	0.0392	178.8
^{241}Pu	0.01952	89.38
^{242}Pu	0.01232	56.65
Total Pu	**0.16**	**728.7**
^{241}Am	0.289	1323
^{243}Am	0.1565	722.6
^{244}Cm	0.052	241.1
^{245}Cm	0.0025	11.64
Total MA	**0.5**	**2298**

2.5.2 Criticality

Figure 2.3 plots the system criticality evolution JEF versus ENDF data files. A large gap between obtained values is clearly visible, particularly in BOC. The gap of about 3600 pcm for k_{eff} or about 4100 pcm for the reactivity due solely to the cross sections should be considered a large value, especially in ADS without compensation rods. The corresponding reactivity gap in the reference core case with MOX fuel is only 430 pcm, also with the value obtained with ENDF being higher than the one with JEF. Altogether it shows that the uncertainties in the MA cross sections will be responsible for the most of the calculation uncertainty of the reactivity in cores with substantial MA loads.

A demonstration of transmutation, with substantial loads of MA, will require substantial improvement of the available neutron cross sections in the materials and physical conditions that will be present in accelerator driven systems. For an early design of an ADS system, with large MA loads and lack of reactivity compensation measures, a design system need to be flexible with regard to the number of loaded fuel subassemblies (with all of the consequences this brings to the design). An adjustment of the criticality required for the real system could be achieved by reducing or increasing the number of loaded fuel assemblies. Another important issue concerns the reactivity swing. In systems with large MA loads a substantially smaller reactivity swing is observed compared to the Figure 2.3.

XADS reference design, which allows the system to work in much longer fuel cycles and, also owing to a smaller Doppler effect, it allows designers to reduce the subcriticality level in order to increase the system power for a constrained proton beam current. However, this nice feature might be jeopardised by a reactivity change with burnup which is different from that projected. The possibility of such scenario exists as is demonstrated here since the calculated reactivity time derivatives obtained in two cases have opposite signs, although, fortunately, they both have a small absolute value. Therefore the observed result of narrowing of the reactivity gap with burn-up does not actually reduce the uncertainty but rather increases it.

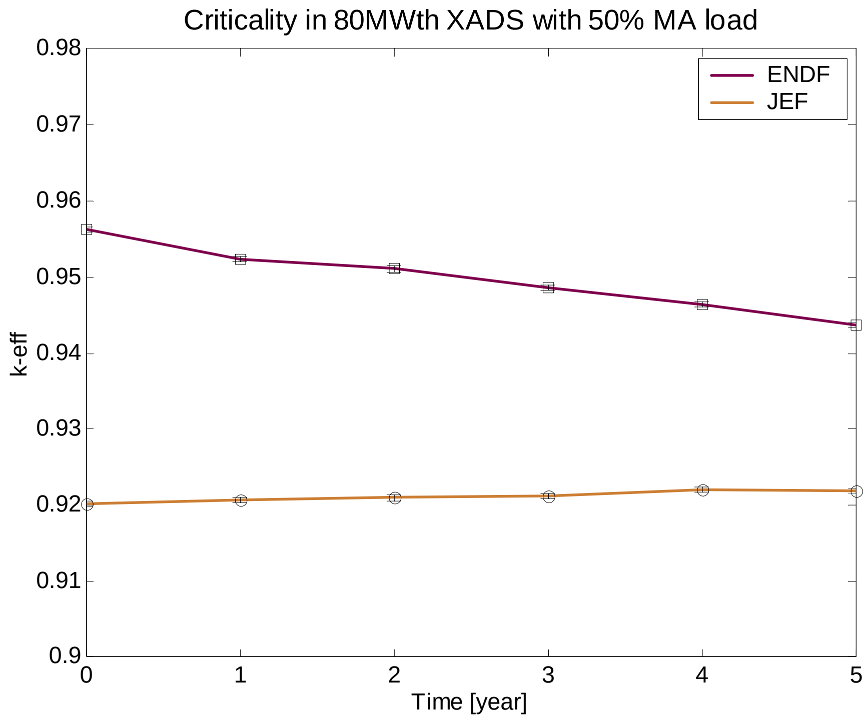

Figure 2.3 Comparison of criticality evolution in XADS with 50% load of MA obtained with different cross section data files

2.5.3 Transmutation efficiency

The comparison of transmuted mass for nuclides experiencing a net destruction is shown in Figure 2.4. Those with a net production are illustrated in Figure 2.5. A good agreement is obtained only for ^{239}Pu, probably due to the vast experimental and industrial experience with it. For the other nuclides larger uncertainties are apparent. The amount of transmuted mass after 3 years is shown in Table 2.6. The period of 3 years was chosen in order to compare the results with the calculations made for the references XADS core with special assemblies Figure 2.4. A faster destruction of americium in the JEF case implies a faster production of plutonium, particularly ^{238}Pu, thus sustaining the criticality more strongly than in the ENDF case. The conversion of curium isotope 244 into 245 is about twice as fast as in the case of JEF. The main reasons for the observed difference in reactivity swing are faster transmutation of americium in the JEF case and their lower fission cross sections, compared to the ENDF case, by about 10%. The fission cross sections of plutonium in both libraries are very close to each other; for ^{238}Pu the difference is 1.3% while for ^{239}Pu and ^{241}Pu it is below 1%. This again proves our earlier conclusion about the uncertainties in MA cross sections as the main source of the reactivity uncertainties.

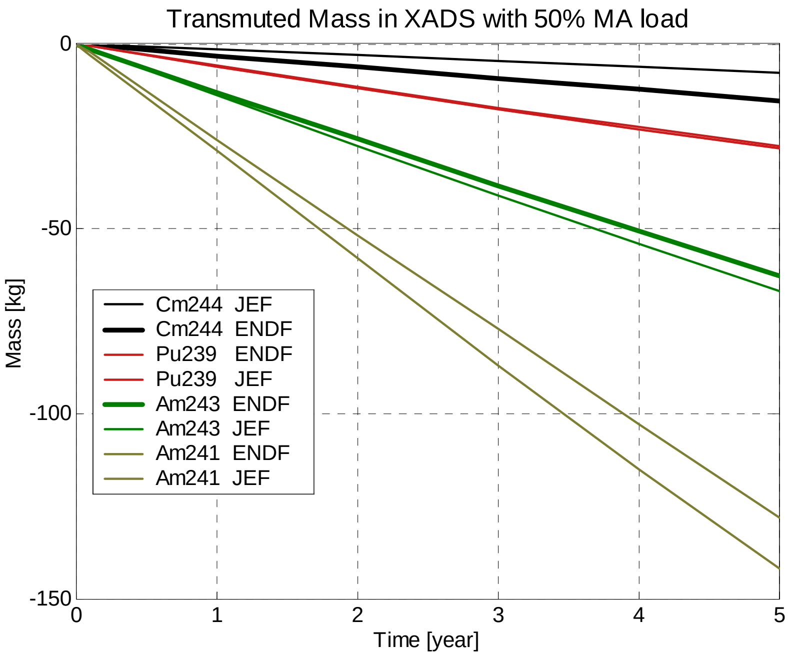

Figure 2.4 Comparison of destructed nuclide mass as calculated with different cross sections: JEF versus ENDF.

Table 2.6: Transmutation of isotopes after 3 years

Nuclide	**Jef2.2**		**ENDFB6.8**	
^{238}Pu	33.9 kg	151 %	28.3 kg	126 %
^{239}Pu	-16.9 kg	-4.44 %	-16.6 kg	-4.36 %
^{241}Am	-85.2 kg	-6.44 %	-76.8 kg	-5.80 %
^{242m}Am	14.7 kg	N.A.	12.3 kg	N.A.
^{243}Am	-40.1 kg	-5.55 %	-37.6 kg	-5.21 %
^{244}Cm	-4.74 kg	-1.97 %	-9.2 kg	-3.83 %
^{245}Cm	2.4 kg	20.6 %	5.53 kg	47.5 %

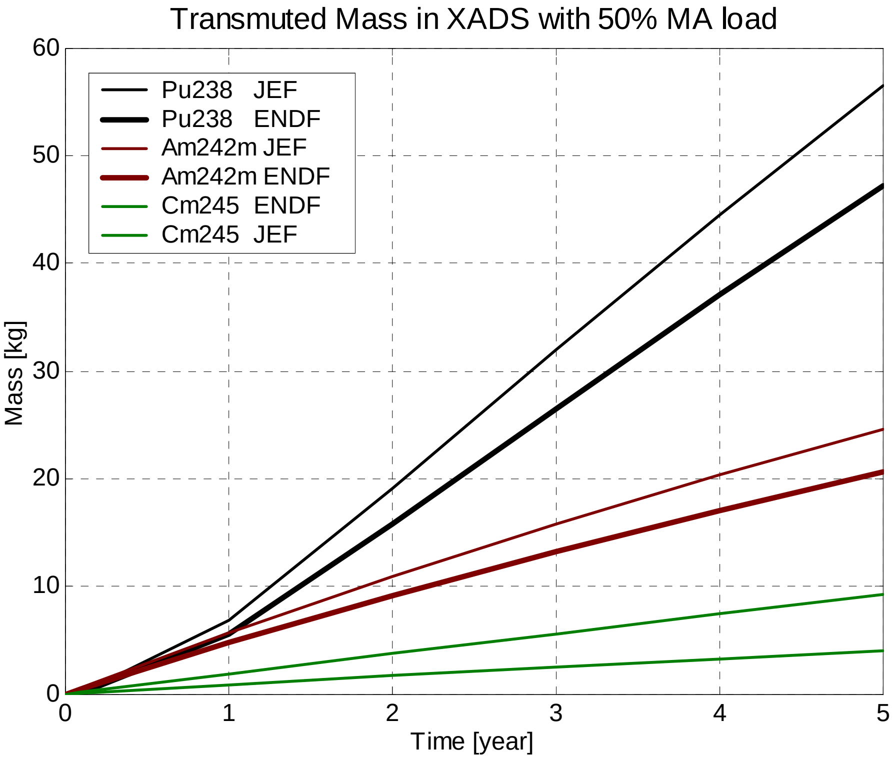

Figure 2.5. Comparison of produced nuclide mass as calculated with different cross sections: JEF versus ENDF.

2.5.4 Conclusions

The difference in reactivity observed at BOC between using JEF and ENDF data files, is about 4000 pcm, for gas-cooled XADS loaded with 50% MA fuel. This difference is associated solely with cross section differences in evaluated nuclear data files, where the uncertainties of MA cross sections are about ten times higher than those of uranium and plutonium. The differences associated with the applied calculation method or an introduction of heterogeneous fuel distribution can increase that gap further, possibly exceeding 5000 pcm. The transition in ADS technology development into the second phase, that is the demonstration of transmutation with substantial loads of MA, will require a substantial improvement of available neutron cross sections for the physical conditions existing in ADS. For the early design of an ADS system with larger MA loads and lack of reactivity compensation measures, the design system would need to be flexible with regard to the number of loaded fuel subassemblies (with all of the consequences and constraints that this brings to the design). Since time evolution of criticality is much less sensitive to the available cross sections a required adjustment of the criticality in the real system can be made possible by reducing or increasing the number of loaded fuel assemblies.

A possible reduction of subcriticality level in order to increase the system power for a constrained proton beam current might be jeopardised by a reactivity change with burnup which is different from that projected. The risk of such a scenario apparently exists, as is demonstrated here, since the calculated reactivity time derivatives obtained in the two cases have opposite signs although fortunately they have a small absolute value. The effect of narrowing the reactivity gap with the burn-up, observed in the calculations, does not reduce the uncertainty since the errors on the cross sections propagate.

A faster transmutation of americium in the JEF case, and its lower fission cross sections, compared to the ENDF case, are responsible for the observed difference in reactivity swing.

2.6 ADS TARGET UNIT DESIGN - RADIOTOXICITY ASSESSMENT OF THE TARGET MODULE

Calculation of radiotoxicity in the target of an ADS covers several areas of radiation transport simulation. It starts from high-energy particle transport – were protons, in this project of energy 600MeV, from accelerator initiate spallation process in the target modules. The further radiotoxicity build-up occurs due to neutron yield from the reactor core causing transmutation of nuclides from initial target composition as well as of already emerged transmutation products – both due to spallation and low energy neutron interaction. Transmutation calculation is performed by MCB system on the basis of estimated in neutron transport calculation values of transmutation reaction rates for all nuclides virtually emerging in the transmutation zone. Every active nuclide contributes to the radiotoxicity by its dose per intake ratio, which can be thought of as a radiotoxicity index. Those values are taken from EURATOM directive for radiation protection [8].

Analysis of radiotoxicity accumulation in the target lead to following conclusions:

- Nuclides predominant for radiotoxicity build-up originated from interaction with core neutrons are: ^{210}Po, ^{210}Bi, ^{206}Bi, ^{207}Bi, ^{205}Bi.
- The major contributions from spallation process are: ^{194}Hg, ^{204}Tl, ^{198}Au, ^{203}Pb, ^{203}Bi.

Analysis of transmutation process of the radiotoxic nuclides after their productions shows that the influence of the neutron or proton flux on their destruction is very limited and by orders of magnitude is overshadowed by the decay term.

What can be important from radioprotection point of view is the analysis of the migration potential of the radiotoxic nuclides.

The list of most volatile and radiotoxic nuclides is the following: ^{194}Hg, ^{197}Hg, ^{203}Hg, ^{195}Hg, ^{193}Hg, ^{125}I, ^{126}I, ^{124}I, ^{130}I, ^{123}I, ^{120}I, ^{82}Br, ^{76}Br, ^{84}Br, ^{83}Br, ^{77}Br, ^{80}Br.

It should be noted that ^{194}Hg predominates the toxicity of that group and due to its physical and chemical properties and substantially long half-life time it should bring much attention for further research of its migration and prevention against contamination of accelerator vacuum tube.

3 SUBCRITICAL EXPERIMENTS – MUSE - EXPERIMENT

One of the objectives of our studies in the frame of the MUSE project was to compare the effects from the GENEPI-generated (d,d)- and (d,t)-neutron sources with the effects from a spallation source, representative of a future ADS. All of the sources were coupled to the same sub-critical MUSE-4 core. MCNP was used for all calculations with the (d,d)- and the (d,t)-sources, while MCNPX was used to simulate the configurations involving the 1000 MeV proton-induced spallation source.

3.1 NEUTRON LEAKAGE SPECTRA FROM THE LEAD BUFFER

One way to investigate the neutron source effects is to first study the sources without the multiplicative medium present and to compare the different neutron leakage spectra. For this purpose, the surrounding fuel and shielding were temporarily removed, as shown in Figure 3.1. For the simulation of the spallation source, the lead buffer/target in the model was extended by one extra sub-assembly towards the proton beam, replacing part of the accelerator tube. Using MCNPX, 1000 MeV protons were directed towards the lead target, generating the spallation source.

The energy spectra of the neutrons exiting the lead buffer are plotted in Figure 3.2 and it is seen that the spectrum from the (d,d)-source has a large peak between 2 and 3 MeV, which is the energy range with which the neutrons are emitted by the GENEPI generator.

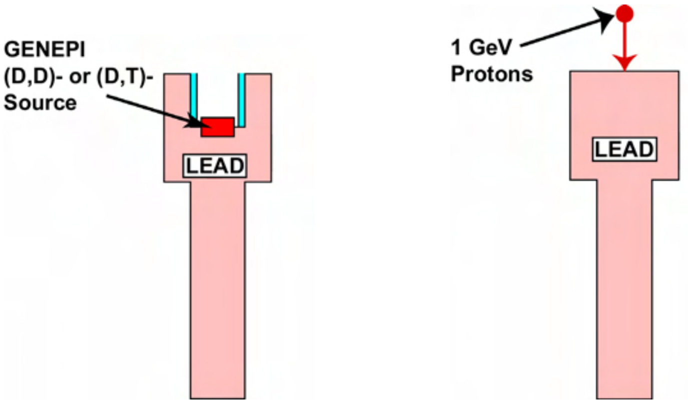

Figure 3.1 Configuration of only the lead buffer region. To the left: (d,d)- or (d,t)-source neutrons emitted at the center of the core. To the right: 1000 MeV protons accelerated towards the extended lead buffer creating a large number of spallation source neutrons.

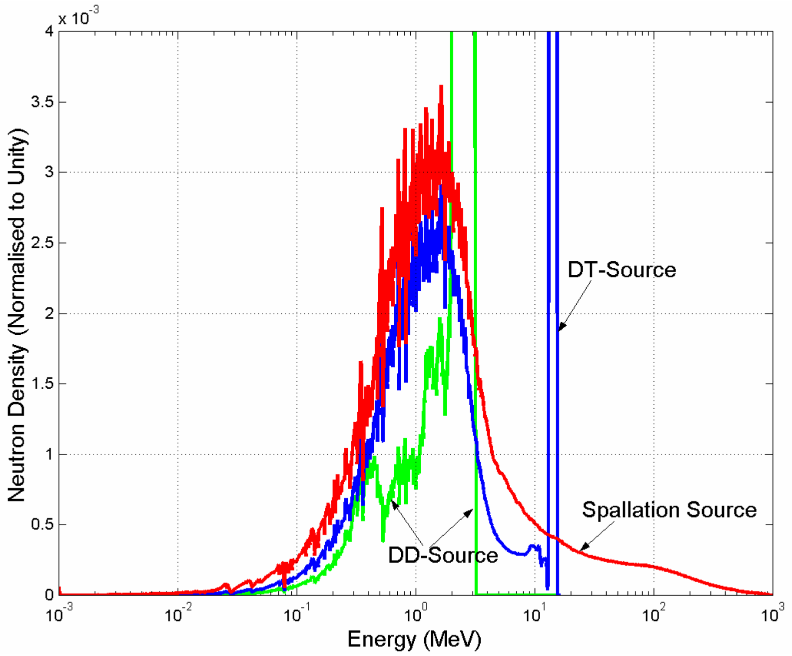

Figure 3.2 Neutron leakage spectrum from the lead buffer/target for a (d,d)-source, a (d,t)-source and a spallation source (1000 MeV protons).

Hence, only a small fraction of the source neutrons have lost their initial energy. This is an expected result, since the energy loss by elastic scattering of neutrons in lead is quite small. However, for the (d,t)-source, the energy of the neutron spectrum has decreased significantly, which is explained by the (n,2n)-reactions in the lead buffer, induced by the 14 MeV neutrons. The (n,2n)-reaction in lead has a threshold at about 7 MeV (Figure 3.3), explaining why there is no such effect for the (d,d)-source. However, about 35 % of the neutrons exiting the lead buffer have not interacted with the lead and are still in the 14-MeV peak. For the spallation source, most of the source neutrons have rather low energy compared to the initial proton energy, with the maximum density at a little less than 2 MeV. This is a typical neutron leakage spectrum for 1000 MeV protons impinging on a lead target of this size. About 7 % of the spallation neutrons, however, still have energy higher than 20 MeV.

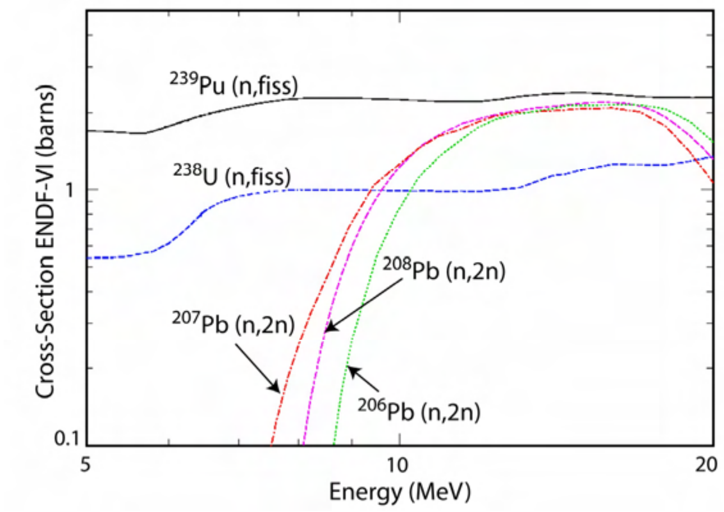

Figure 3.3 Neutron microscopic cross-sections for ^{239}*Pu fission,* ^{238}*U fission and (n,2n)-reactions in* ^{206}*Pb,* ^{207}*Pb and* ^{208}*Pb (ENDF/B-VI).*

The GENEPI-generated neutron sources in the MUSE experiments were surrounded by a lead buffer with the purpose to simulate the neutron diffusion of an actual lead (or lead-bismuth) target in an ADS. The comparison of the neutron leakage spectra shows that the neutrons from the (d,t)-source in MUSE-4 have a rather similar energy spectrum as the neutrons from the spallation source have, and can from this point of view be considered more representative for a spallation-driven system than the (d,d)-source.

3.2 NEUTRON SPECTRA IN THE CORE

The neutron energy spectra for the three different sources have been computed with the entire core present (including fuel, reflector and shields), according to Figure 3.4. As in the case of the neutron leakage calculations in the previous section, the target/buffer was extended by one extra sub-assembly for the calculations with the spallation source (Figure 3.1). The spectra were calculated in two different positions; one in the lead buffer and one in the fuel (marked with black dots in Figure 3.4). The calculations were performed for the second sub-critical state of MUSE-4 (SC2, k_{eff} ~0.97). The spectra for the other sub-critical states (SC0, k_{eff} ~0.994 and SC3, k_{eff} ~0.95) are not shown here, since they are rather similar to the spectra of SC2. However, as there is less fission multiplication for larger sub-criticalities, the origin of the sources becomes a little more pronounced in SC3 and vice versa in SC0.

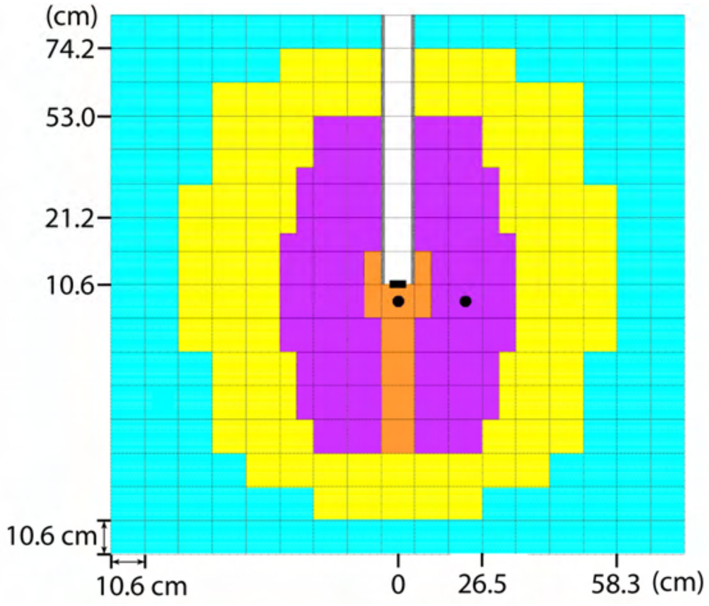

Figure 3.4 The two positions (marked with the black dots) where the neutron energy spectra have been calculated.

In Figure 3.5, the neutron energy spectra for the three different sources calculated in the lead buffer are plotted. The spectra are very similar to each other, the energy density being maximal at about 500 keV. Several spectrum characteristics of the multiplying fuel can be recognized, for example the two dips in the neutron fluxes caused by the scattering resonances in sodium (~3 keV) and oxygen (~0.4 MeV). This indicates that the neutron spectrum in this position is rather dominated by the fission multiplication in the fuel and that many of the neutrons from the fuel enter into the lead buffer. However, a smaller fraction of the neutrons have energies different from the average behavior and the two peaks representing the origins of the GENEPI-generated neutron sources and the high-energy tail of the spallation source are very clear in this position. It should be noted that the position in the lead buffer where the energy spectra have been calculated is only about 5 cm from the position where the GENEPI source neutrons are emitted.

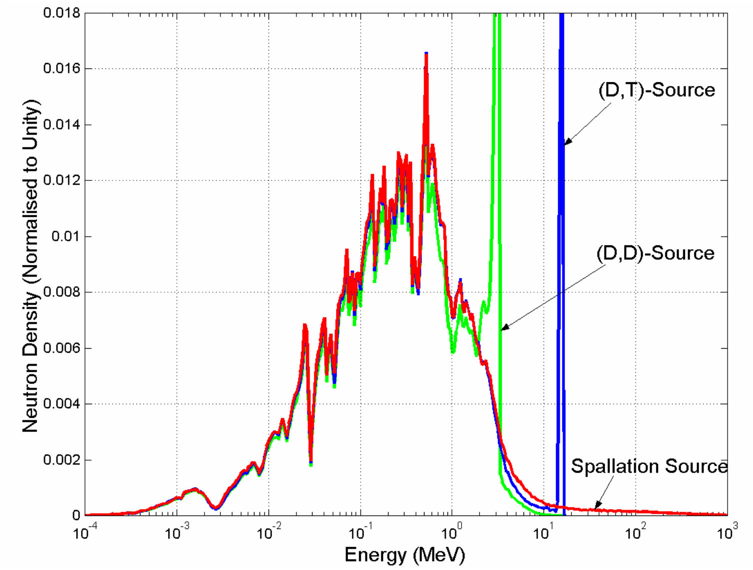

Figure 3.5 Neutron energy spectra in the lead buffer.

In Figure 3.6, the neutron spectra in the fuel at a point located 21 cm from the center of the core and about 10 cm into the fuel are depicted. Naturally, the fuel spectrum characteristics in this case are even more pronounced than in the lead buffer. The three different curves are very similar and almost no traces from the origins of the external neutron sources can be observed. Only about 0.15 % of the (d,t)-source neutrons are still in the 14 MeV peak and about 0.04 % of the neutrons in the spallation-driven system have energies higher than 20 MeV.

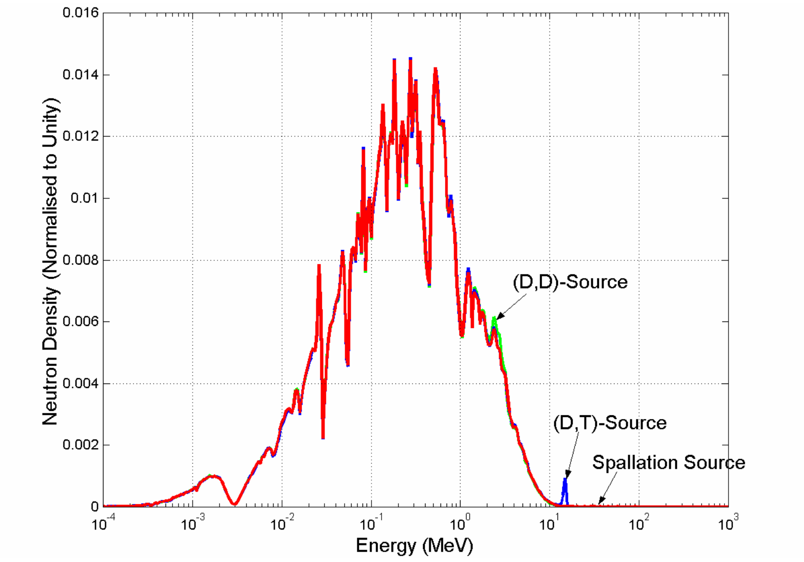

Figure 3.6 Neutron energy spectra in the fuel.

The computed neutron spectra show that the energy spectra in the core, originating from the three different external sources are very similar to each other. These results indicate the validity of one of the basic hypothesis of the experiments, namely that the choice of using a spallation source or the source neutrons produced by the (d,d)- or the (d,t)-reactions, will affect very little the neutron spectrum in the fuel. Only inside the lead buffer and at the buffer/core interface some differences are observed. We therefore conclude that, for the purpose of computing neutron spectrum-weighted quantities, the presence of the external source can be neglected beyond a few centimeters into the fuel, whatever the neutron source energy distribution.

3.3 DISTRIBUTION OF THE SPALLATION NEUTRONS

The distribution of the neutrons produced in the spallation target was calculated for 1000 MeV protons impinging on the extended MUSE-4 target. The properties, in terms of energy and space, of the neutrons emerging from the proton-induced spallation reactions were recorded. These emitted neutrons have been called “primary neutrons”, as they include only the first neutron in each neutron chain reaction. No neutrons generated in reactions induced by other neutrons (secondary neutrons) are included. The definition of primary neutrons is further treated in Appendix 2 and 3 and in Section 3.4 .

The spatial distribution of the positions where the primary neutrons were created was found to be rather limited. Axially, most of the neutrons were created in the upper part of the lead target (77% within the first 20 cm), as shown in Figure 3.7. It is also seen that the neutron density, which in addition to the primary neutrons include

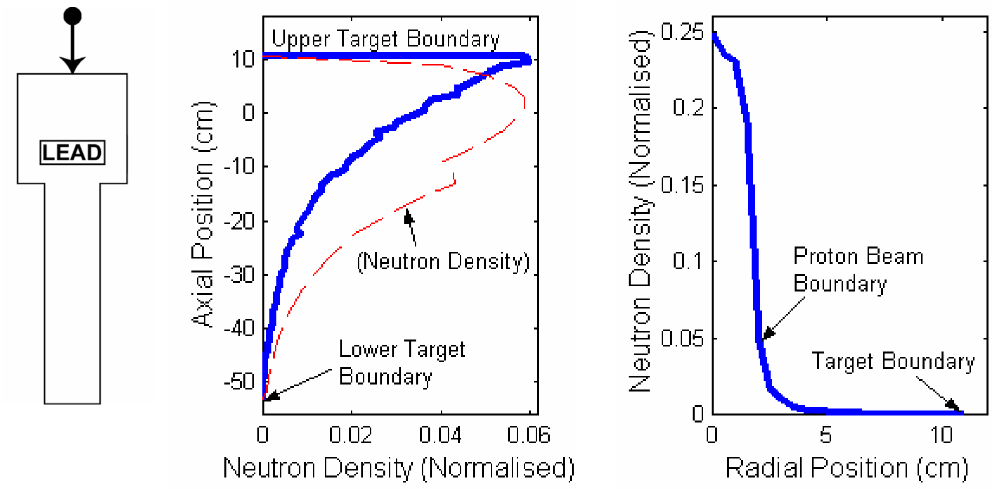

Figure 3.7 To the left: 1000 MeV protons impinging on the extended MUSE-4 lead buffer/target. In the middle: Axial distribution of the primary spallation neutrons. To the right: Radial distribution of the primary spallation neutrons.

also secondary neutrons, has a different shape with its maximum about 10 cm below the top of the target. The radial distribution was found to be very peaked around the axis of the incident proton beam, about 98% of the neutrons were created within a 3 cm radius. In this case, the radius of the uniformly distributed proton beam was 2 cm. The energy distribution of the primary neutrons produced by the 1000 MeV protons is displayed in Figure 3.8. We note that 16.8% of the neutrons have energies higher than 20 MeV and 3.3% of them higher than 150 MeV. The neutrons with very high energy were mainly emitted in the forward direction of the proton beam.

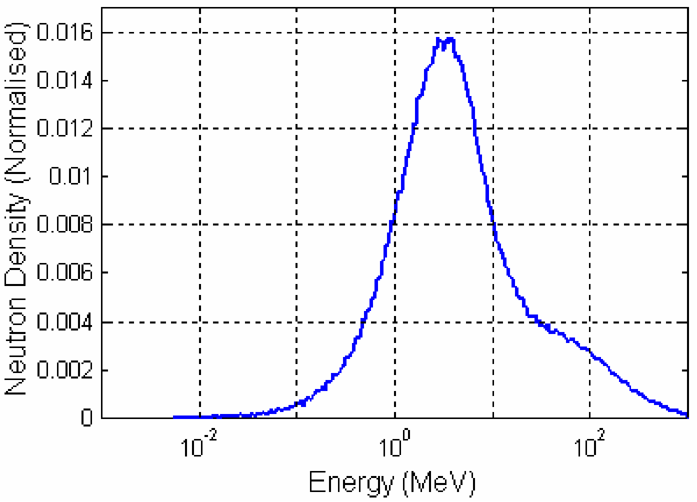

Figure 3.8 Energy spectrum of the primary spallation neutrons created by the 1000 MeV protons.

On average, there were about 14.5 primary neutrons produced in each proton-induced spallation reaction. This value may be compared with the total number of neutrons produced in the lead target, i.e. about 21 neutrons per incident proton. Thus, almost a third of the neutrons that exit the lead target and enter into the fuel are secondary neutrons, most of them created in neutron-induced spallation reactions and (n,xn)-reactions. In a large cylindrical target (r≥30 cm), this fraction is about 50%, the total number of neutrons created per proton being as large as 30, while the number of primary spallation neutrons are the same, independently of the target size.

3.4 NEUTRON SOURCE EFFICIENCY

The neutron source efficiency φ* was determined for the GENEPI-generated neutron sources and for the spallation source, all of them coupled to the second sub-critical state (SC2) of the MUSE-4 experiments.

3.4.1 Definition of φ*

The neutron flux distribution ϕ_S in a sub-critical core is the solution to the inhomogeneous steady-state neutron transport equation

$$\boldsymbol{A}\phi_s = \boldsymbol{F}\phi_s + S \ , \tag{3.1}$$

where

$$\boldsymbol{A}\phi_s = \boldsymbol{\Omega}\cdot\nabla\phi_s + \sigma\phi_s - \sum_{x\neq f}\iint \sigma'_x f_x \phi'_s d\boldsymbol{\Omega}' dE' \tag{3.2}$$

$$\boldsymbol{F}\phi_s = \iint \frac{1}{4\pi}\sigma_f \nu(\boldsymbol{r};E'\to E)\cdot\phi'_s d\boldsymbol{\Omega}' dE' \tag{3.3}$$

F is the fission production operator, ***A*** is the net neutron loss operator and *S* is the external source. The neutron source efficiency, usually denoted φ*, represents the relative efficiency of the external source neutrons and can be expressed according to the following equation;

$$\varphi^* = \left(\frac{1}{k_{eff}} - 1\right)\cdot\frac{<\boldsymbol{F}\phi_s>}{<S_n>} \ , \tag{3.4}$$

which is valid in the range $0 < k_{eff} < 1.0$. $<\boldsymbol{F}\phi_s>$ is the total production of neutrons by fission and $<S_n>$ is the total production of neutrons by the external source. In the above formula, the brackets imply integration over space, angle and energy. Eq. (3.4) relates the total fission neutron production $<\boldsymbol{F}\phi_s>$ to the external neutron source, φ* and the reactivity (1 – 1/ k_{eff}). It shows that, for given values of k_{eff} and $<S_n>$, the larger φ* the larger the fission power produced in the system. The quantities on the right hand side of Eq. (3.3.4) are standard outputs from MCNP and MCNPX.

3.4.2 Estimation of the Statistical Error in φ*

In order to estimate the statistical uncertainty in φ*, the formula for "propagation of error" was applied (Eq. (3.5)), assuming that the errors of $<\boldsymbol{F}\phi_s>$ and $<S_n>$ (labeled *F* and *S* in this sub-section) are ΔF and ΔS.

$$\Delta f(x_1,x_2,\ldots) = \sqrt{\left(\frac{\partial f}{\partial x_1}\Delta x_1\right)^2 + \left(\frac{\partial f}{\partial x_2}\Delta x_2\right)^2 + \ldots + \rho_{12}\cdot\frac{\partial f}{\partial x_1}\Delta x_1\cdot\frac{\partial f}{\partial x_2}\Delta x_2 + \ldots} \ . \tag{3.5}$$

The correlation constant ρ could be either positive or negative; negative if k_{eff} and *F* are correlated and positive if they are anti-correlated. However, as a first approximation, ρ was assumed to be zero. With the derivatives $\frac{\partial\varphi^*}{\partial k_{eff}}$, $\frac{\partial\varphi^*}{\partial F}$ and $\frac{\partial\varphi^*}{\partial S}$ inserted in Eq. (3.5), an expression for the relative error in φ^* can be obtained,

$$\left(\frac{\Delta\varphi^*}{\varphi^*}\right)^2 \approx \left(\frac{1}{1-k_{eff}}\cdot\frac{\Delta k_{eff}}{k_{eff}}\right)^2 + \left(\frac{\Delta F}{F}\right)^2 + \left(\frac{\Delta S}{S}\right)^2 . \qquad (3.6)$$

Eq. (3.6) was used in all simulations to estimate the statistical uncertainty in φ*.

3.4.3 Definition of the External Neutron Source in Spallation-driven Systems

Since the actual source particles in a system coupled to a proton-induced spallation source are protons and not neutrons, it is not obvious which is the best way to define the external neutron source. The procedure to calculate φ* is usually divided into two steps, the first generating the source neutrons produced from the proton beam interacting with the target and the second step determining the efficiency of these source neutrons. Different source definitions are possible and they will result in different values and meanings of φ*. A brief summary of four different definitions of the external neutron source that have been used in the ADS field is given in [9] and [10]. Among these, the two most frequently used definitions, the target neutron leakage source and the energy cut-off source, as well as the primary neutron source, are described in the following. The fourth definition is the fission source, consisting of the first generation of fission neutrons.

3.4.3.1 The Target Neutron Leakage Source

The approach of the target neutron leakage source uses the neutrons that leak out radially from the target as source neutrons [10]. The method consists of, in the first step, transporting the high-energy protons and the secondary particles that they produce in the target. The neutrons that leak out from the target are defined as the source and their properties, in terms of position, direction and energy are written to a source file. Only the target is present in the first simulation, so no once-leaked neutrons re-entering the target are included in the source definition. In the second step, the leakage neutrons are reemitted as fixed source neutrons in a separate run and the efficiency (φ*) of them is determined. Since the target neutron leakage spectrum includes a high-energy tail, both step 1 and 2 need to be simulated with a high-energy transport code (which can simulate neutrons with energy up to the incident proton energy).

3.4.4 The Energy Cut-off Neutron Source

The other way to define the neutron source is to collect the neutrons that fall below a certain cut-off energy (usually 20 or 150 MeV) (see Appendix 2). In the first step, a high-energy code is used to transport the accelerated protons and the secondary high-energy particles. The neutrons that are produced are either killed if they are born below the cut-off energy or transported until they fall below this energy. The properties of the killed neutrons are written to a source file, which is followed by their reemission in the second-step run and the calculation of φ*. An advantage of this approach is that the second step can be simulated with a low-energy transport code. The cut-off energy is set to the upper energy limit of the cross-section library that will be used in the second-step calculation. This is desirable since many reactor code systems are limited to the energy range covered by the cross-section data library (generally 20 or 150 MeV).

3.4.5 The Primary Neutron Source

The source neutrons produced from spallation are here defined as the neutrons produced directly in a spallation reaction induced by a proton (or by any other particle, except neutrons), see [11]. They are called “primary neutrons”, in contrast to “secondary” neutrons, which are the neutrons created by the primary neutrons (e.g. via neutron-induced spallation or (n,xn)-reactions). In this approach, the starting point for the chain of neutron multiplication is the moment when a neutron is born in a non-neutron-induced spallation reaction. The primary neutron might be multiplied by secondary spallation (if its energy is very high) and/or (n,xn)-reactions in the lead target, followed by fission reactions in the fuel, the end point of the neutron multiplication chain being the absorption or escape of the last neutron originating from the initial primary source neutron.

3.4.6 Calculations of φ* for the MUSE-4 Model

The multiplication factor k_{eff} and the total number of neutrons produced by fission ($<\boldsymbol{F}\phi_s>$) were calculated for the three different sources. Knowing these two parameters φ* can be determined according to Eq. (3.4). $<\boldsymbol{F}\phi_s>$ is automatically normalized per source neutron in MCNP (and in MCNPX if the source particles are neutrons), so $<S_n>$ was always equal to 1 in the calculations. The corresponding statistical errors (±1 standard deviation) were calculated using Eq. (3.3.6). The results, including error estimates, are listed in Table 3.1.

For the calculations of the spallation source, the primary neutron source definition was used and the MCNPX simulations calculating φ* were divided into two steps. In the first simulation, a large number of protons were accelerated (to 1000 MeV) towards the lead target. The protons were uniformly distributed across the beam of radius 2 cm. The angular, energy and spatial distributions of all neutrons that were created directly in the spallation interactions (primary spallation neutrons) were recorded. After that, the neutron trajectories were immediately terminated. This procedure produces a spectrum of primary spallation neutrons, i.e. no secondary neutrons are included. In the second step, these primary spallation neutrons were supplied to the MCNPX code as fixed source neutrons for separate simulations and φ* was determined.

Table 3.1: Source Efficiency for the MUSE-4 SC2 Configuration

Source	k_{eff}	$< \boldsymbol{F}\phi_s >$	φ*
(D,D)-Source	0.97285 (± 18 pcm)	48.8 (± 0.4 %)	1.36 (± 0.010)
(D,T)-Source		77.6 (± 0.5 %)	2.17 (± 0.020)
Spallation Source		80.6 (± 1.0 %)	2.25 (± 0.030)

The energy of the emitted (d,d)-source neutrons (2-3 MeV) is only slightly larger than the average energy of a neutron produced by fission. Since φ* is 1.0 for an average fission neutron, the value for the (d,d)-source is therefore expected to be equal or slightly larger than 1, which is indeed the case. For the (d,t)-source, the reason for the higher values of φ* is the larger fission rate, part of which coming from fissions induced by the neutrons multiplied by (n,2n)-reactions in the lead buffer. It is seen in Table 3.1 that the number of fission neutrons per source neutron is large, approximately 59 % larger than for the (d,d)-source. The (n,2n)-multiplication of the 14 MeV neutrons increases the number of neutrons leaking out into the fuel and inducing fission chain reactions, thus enhancing the neutron source efficiency. In average, about 1.5 neutrons leave the lead buffer per initial 14 MeV neutron, compared to 1 neutron for each 2.7 MeV (d,d)-source neutron.

Concerning the spallation source neutrons, the values of φ* obtained in the simulations are somewhat higher than for the (d,t)-source. This is due to the fraction of primary neutrons having very high energy. Most of the neutrons from the spallation process are born with an energy lower than the (n,2n)-cross-section threshold in lead (i.e. no (n,2n)-multiplication occurs), but the neutrons with very high energy contribute significantly to φ*. Additional calculations investigating the contribution to φ* by the high-energy fraction of the spallation source show that the primary source neutrons with energies higher than 20 MeV (16.8 % of all source neutrons) contribute for about 50% to the total φ*. The explanation for this is that most of the high-energy neutrons from the spallation source have already been multiplied in the lead (most of them via secondary neutron spallation and (n,xn)-reactions) *before* they enter into the fuel. Each of them gives birth to a number of lower-energy neutrons, which then leak out of the lead and induce fission chain reactions in the fuel.

3.5 DYNAMIC NEUTRON SOURCE RESPONSE

Techniques to monitor the sub-criticality level during operation in ADS are under development within the MUSE-4 program. With the introduction of GENEPI into MASURCA, it is now possible to perform accurate dynamic measurements, allowing for experimental reactivity determination of the sub-critical multiplying medium. The dynamic measurements are based on the pulsed mode operation of GENEPI.

In the experiments, after the reactivity calibration by the rod drop technique, the sub-critical level of the different configurations will first be precisely determined by the well-known static Modified Source Method (MSM). In the next step, based on reactor kinetics and neutron noise theory, different dynamic techniques are applied, in order to determine the reactivity level. The methods being studied are the pulsed neutron source method, the inverse kinetics method, the Rossi-α method and the Feynman-α method. These methods, as well as results and interpretations from the dynamic experiments have been presented in several documents.

3.5.1 The Pulsed Neutron Source Method

When a multiplying medium is sub-critical, the neutron density will decay exponentially and the pulse will quickly disappear, according to basic point-kinetic theory. The decay process after a neutron pulse in a sub-critical medium is governed by the following relation;

$$N(t) = N_0 e^{-\alpha t} \ , \qquad (3.7)$$

where $\alpha = \frac{1 - k_{prompt}}{\Lambda}$ and Λ = neutron generation time. Hence, α is the slope of the decaying curve and it is directly related to the reactivity. Eq. (3.7) is derived from the reactor kinetics equation, not taking the delayed neutrons into account. Within this time scale there is no contribution from delayed neutrons, which is the reason why α is directly proportional to k_{prompt} and not to k_{eff}.

The "Pulsed Neutron Source Method" is one of the most promising techniques for the experimental reactivity determination of the sub-critical core in a future ADS. The procedure consists of, after having registered the neutron intensity decay after a neutron pulse, determining the slope of the curve (α) and then determine $k_{prompt,}$ according to

$$k_{prompt} = 1 - \alpha \cdot \Lambda \qquad (3.8)$$

The neutron generation time, Λ first has to be calculated and does not change much with reactivity. In order to obtain the effective reactivity, you also need to determine the effective delayed neutron fraction ($k_{eff} = k_{prompt} + \beta_{eff}$).

The time response in one of the detectors in MASURCA has been simulated for a GENEPI-generated (d,t)-neutron source pulse for the three sub-critical states, SC0, SC2 and SC3 of the MUSE-4 experiments. The generation time Λ was approximately 0.60 microseconds. The results computed by MCNP are plotted in Figure 3.9. It is clear from the figure that the more sub-critical the core is, the faster is the prompt decay rate. The α-values corresponding to the sub-critical states (determined graphically from the plotted curves) are for SC0; $\alpha_0 \approx 1 \cdot 10^4$ ($k_{prompt} \approx 0.995$), for SC2; $\alpha_2 \approx 5 \cdot 10^4$ ($k_{prompt} \approx 0.97$) and for SC3; $\alpha_3 \approx 8 \cdot 10^4$ ($k_{prompt} \approx 0.95$). The results are in good agreement with Eq. (3.7).

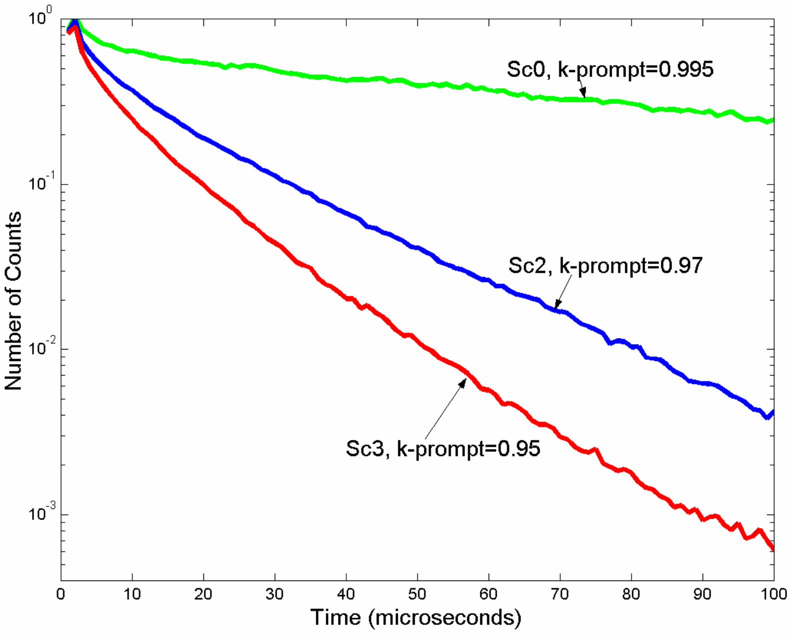

Figure 3.9 Neutron source response after a (d,t)-source pulse for the three different sub-critical configurations in MUSE-4, SC0, SC2 and SC3.

3.6 REPLACEMENT OF SODIUM COOLANT BY LEAD COOLANT

It was decided within the MUSE community to include, in an extended phase of the MUSE-4 experiments, a new configuration, in which 22 of the central sodium-cooled fuel sub-assemblies were replaced by lead-cooled sub-assemblies (the limit of the lead-cooled region being marked by the black line in Figure 3.10). Three parameters; k_{eff}, the source efficiency φ^* and the dynamic neutron source response were studied for this centrally lead-cooled configuration. The neutron source used in the study comparing this configuration with the original sodium-cooled configuration was the GENEPI-generated (d,t)-source.

When calculating k_{eff} for the new lead-cooled configuration, it was found that it increases with about 1600 pcm. The reason for this is that there is less absorption in lead and that the energy spectrum is different. In order to maintain the same reactivity for the two configurations, which is particularly important for the comparison of the neutron source response, some of the peripheral fuel sub-assemblies were removed. k_{eff} was approximately 0.974 in both cases.

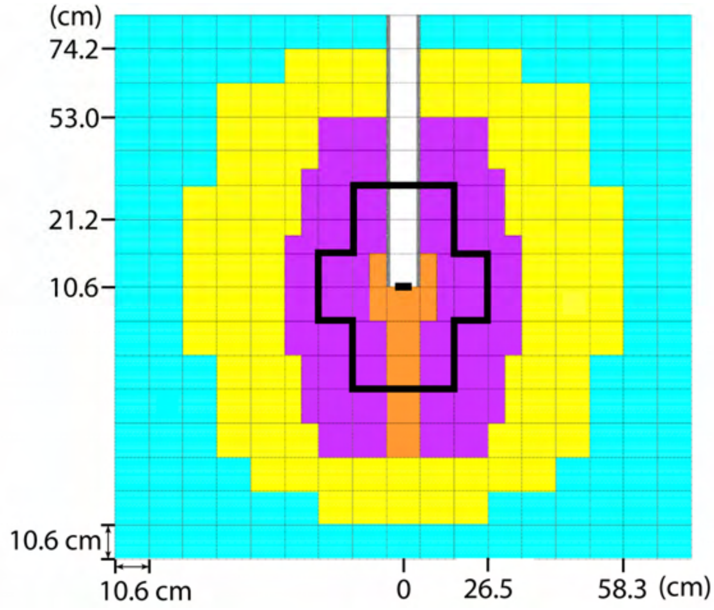

Figure 3.10 Configuration where 22 of the sodium-cooled sub-assemblies were replaced by lead-cooled sub-assemblies (the limit of the lead-cooled sub-assemblies is marked by the black line).

3.6.1 Source Efficiency

The results from the comparison of φ*, for the two configurations, are listed in Table 3.2. As is shown, the value for the lead-cooled configuration is significantly higher than for the sodium-cooled configuration, 2.39 compared to 2.13. The reason for this difference is again the (n,2n)-multiplicative effect in lead, the same effect that caused the large difference in φ* between the (d,d)- and the (d,t)-source. Since there is more lead in the central part of the core in the lead-cooled configuration, where there are still many neutrons with energy higher than about 7 MeV, there is more (n,2n)-reactions. These circumstances enhance the neutron multiplication as well as φ*. Since the source efficiency relates the source intensity to the power produced in the system, we conclude that the replacement of sodium coolant by lead coolant in the 22 central fuel sub-assemblies increases the power by approximately 12%.

Table 3.2: Source Efficiency φ* for the Sodium-cooled and the Centrally Lead-cooled MUSE-4 Configurations

Configuration	k_{eff}	φ*
Sodium-cooled	*0.97428 (± 20 pcm)*	*2.13 (± 0.02)*
Centrally lead-cooled	*0.97382 (± 27 pcm)*	*2.39 (± 0.03)*

3.6.2 Dynamic Neutron Source Response

Finally, the neutron source response from a pulse insertion from the (d,t)-source, registered by a detector in the core, was calculated and it is seen in Figure 3.11 that the intensity is somewhat higher (on average ~15%) for the lead-cooled configuration. The explanation for this is the same as for the difference in source efficiency, namely the multiplicative effect of the (n,2n)-reactions in the lead. Since the neutron multiplication is higher in the second case, the intensity registered by the detector will also be higher. We also observe that the prompt decay rate is more or less the same for the two systems. The neutron generation time Λ, calculated by MCNP, changes very little and since k_{eff} is the same, the α-value and the decay rate must also be the same.

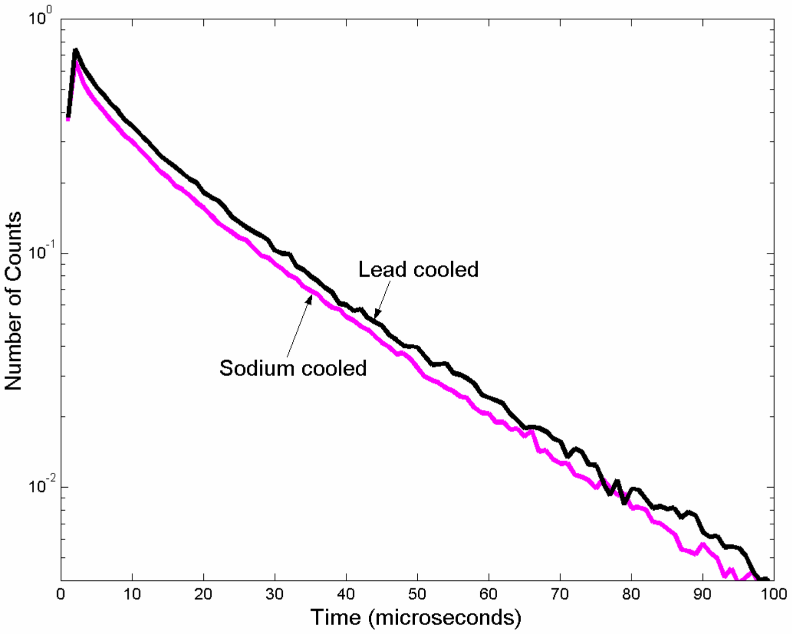

Figure 3.11 Neutron source response in one of the detectors from a neutron source pulse.

4 ADS SAFETY STUDIES - KINETICS STUDIES

4.1 POINT KINETICS ANALYSIS OF ACCELERATOR DRIVEN SYSTEMS

4.1.1 Introduction

Appropriate neutron kinetics models are required for predicting transient behaviour in nuclear reactor systems. The so-called “point kinetics approximation” is a widely used method for analysing dynamic phenomena. It has been extensively applied for the transient design analysis of existing reactors and it forms the basis of many transient analysis computational codes. It is based on kinetics theory developed for critical reactor studies. The ADS is a non-self-sustaining, subcritical reactor driven by an external neutron source that is maintained by a charged-particle accelerator. While the utility of the point kinetics methodology for critical reactor analysis is well known, its applicability to source-driven subcritical systems is subject to discussion [11]. Because the neutron balance equations that describe the response in source-driven reactors are fundamentally different from the conditions in a critical reactor, it has been suggested [12] that the point kinetics technique may be inappropriate for ADS studies; it is nonetheless very popular and often used for analysis of such systems.

In this chapter the precision of the point kinetics approximation in its application to ADS is investigated. The basic approach is by comparison with an “exact” numerical solution as obtained using full three-dimensional energy-space-time dependent calculations, coupled with thermal- and hydraulic feedback effects. Results are obtained as a function of k_{eff} to provide insight into the dependence of the performance on the subcritical level. The work was performed in collaboration with Argonne National Laboratory (ANL).

4.1.2 Point Kinetics Theory

The point kinetics equations were first derived by Henry [13]. Their limitations and capabilities for critical reactor analysis have been investigated in great detail [14]-[16]. The purpose behind the formulation of the kinetics equations is to derive a lumped model that describes the change in the average level of the flux, i.e., the integral of the neutron flux over the energy and the spatial domain. The point kinetics equations are obtained by recasting the time-dependent diffusion (or transport) equation into:

$$\frac{dp(t)}{dt} = \frac{\rho(t) - \beta(t)}{\Lambda(t)} p(t) + \sum_k \lambda_k c_k(t) + s(t)$$

$$\frac{dc_k(t)}{dt} = \frac{\beta_k(t)}{\Lambda(t)} p(t) - \lambda_k c_k(t)$$

The above equations are usually referred to as the “point kinetics equations” or sometimes the “exact point kinetics equations” in a way to distinguish them from the simplifying assumptions applied in the point kinetics approximation. The new quantities, ρ, β, Λ, s, and c_k that emerge in point kinetics equations are the point kinetics parameters. They are integral quantities and they arise only in the derivation of the point kinetics equations. This is realized since the basic time-dependent neutron diffusion equations do not involve these concepts. It should be recognized that, as long as the exact definitions are applied in the calculation of the kinetics parameters (that implies full solution of the space-energy-time problem), the point kinetics equation is exact and completely equivalent to the basic, time-dependent diffusion (or transport) equation, but in a different form. This is true for critical as well as for subcritical systems. The error is introduced when an approximate representation of the time-dependent flux shape, e.g., the point kinetics approximation, is applied. In that case, a prefixed shape representation of the flux is used throughout the entire transient, only the “level” of that flux shape changes, i.e., first-order perturbation theory approach. In the point kinetics approximation, the basic assumption is that the time dependence is separable from the (**r**,E) dependence, i.e, the space-energy flux shape is fixed at all times. For a critical reactor, it permits the use of first-order perturbation theory to calculate the reactivity changes. The neutron balance equation for a reactor with an independent source is mathematically an inhomogeneous problem. In strict terms, separation of variables is not possible for such cases. Thus, the point kinetics approximation becomes questionable. Moreover, the adjoint flux, which is normally used as a flux weighting function in the perturbation theory approach for a critical system, is not uniquely defined for a source-driven system. This invalidates the use of the standard first-order perturbation formula. The usual procedure for generating a weight function for a source-driven reactor is to employ an artificial initial λ-mode adjoint weighting function, i.e., the solution to the source-free adjoint equation.

4.1.3 Computational Models

The test model used in the present study is based on a previous OECD/NEA benchmark model [17]. The model pertains to an accelerator-driven, lead-bismuth cooled, and minor-actinide loaded transmuter core. The core consists of a central lead-bismuth target region and a homogenized fuel region surrounded by radial and axial reflectors (70% steel and 30% coolant). 114 fuel assemblies are included in the hexagonal-z representation; Figure 4.1contains a plan view of a one-sixth symmetry section of the core. The height of the active core is 100 cm. The fuel consists of 2/3 minor actinides and 1/3 plutonium with a ZrN diluent; $(Pu_{0.1},MA_{0.2},Zr_{0.7})N$, where MA represents minor actinides such as Np, Am, and Cm. Fuel compositions correspond to plutonium discharge from UOX-fueled LWRs mixed with MA from a “double strata” strategy [18]. Start-up core loading is used in the simulations. The fuel is further diluted with

71% ZrN. Core material compositions are summarized in Table 4.1. Additional lattice parameters are included in Table 4.2.

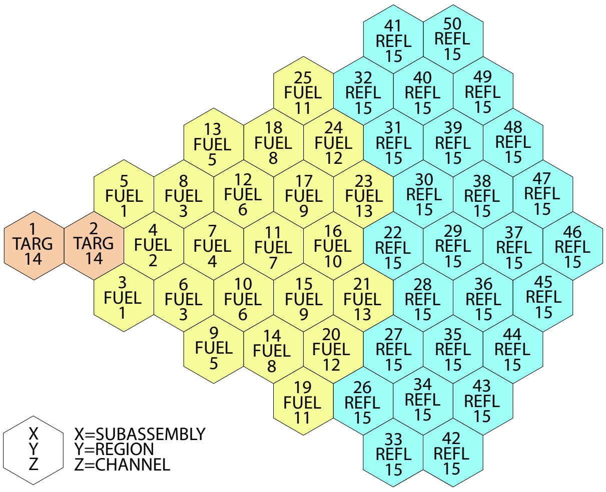

Figure 4.1 One-Sixth Core Subassembly and Channel Assignment.

Table 4.1: Material Specification of the Reference Core Configuration

Core Volume Fractions:
- 30 vol% Fuel
- 48 vol% Coolant (Pb/Bi eutectic)
- 22 vol% Clad + Structure (stainless steel)

Reflector Volume Fractions:
- 30 vol% Coolant
- 70 vol% Stainless Steel

Fuel:
- Fuel Material: $(Pu_{0.1},MA_{0.2},Zr_{0.7})N$
- Theoretical density (300°C): 9.19 g/cm^3
- Fuel smear density: 84 % of theoretical
- 68% MA/TRU ratio
- 71% molar fraction ZrN

Table 4.2: Lattice parameters

Number of pins per assembly	217
Pitch/diameter ratio	1.6
Pin diameter [mm]	7.366
Cladding thickness [mm]	0.787
Ducts flat-to-flat distance [cm]	15.956

Numerical testing was performed with coupled core dynamics calculations using the SAS4A/DIF3D-K code [19]. The “exact” results are obtained from a direct numerical solution of the time-, space-, and energy-dependent multigroup diffusion equation. The direct solution is used as a standard of comparison for the point kinetics solution. One advantage of using the SAS4A/DIF3D-K program for the current task is that the direct solution method and the point kinetics procedure are implemented within the same code. This makes it straightforward to compare the underlying methods without worrying about consistency among different computational procedures and models. For example, the initial steady-state solutions, cross sections, thermal- and hydraulics treatments, and model specifications are all identical.

The spatial flux solutions are based on a three-dimensional nodal diffusion theory method [20]. The core is partitioned into assembly-sized hexagonal unit cells in the horizontal planar direction and axially subdivided into twenty-one axial nodes, each with a mesh spacing of 4.76 cm. In reflector regions, axial mesh sizes of 12.5 cm are employed. The radial distance between the assembly vertical centerlines is 16 cm. The solution takes advantage of one-sixth core symmetry by solving for a single sextant section of the core. Uniform nuclear cross sections are used within each node. In the direct method, the time-dependent component is solved using a fully implicit finite-difference approximation (the DIF3D-K [21] code uses a specified θ-method [22] of time differencing). The theta (θ=1) method consists of representing the time differential operators with their implicit finite-difference formulation. Thermal- and hydraulic calculations are performed for 13 channels, each representative of an average pin within individual subassemblies (See Figure 4.1 for channel to subassembly assignments). Feedback effects (due to Doppler and coolant density variations) are included as necessary to reproduce the physical situation as closely as possible. Feedbacks are accounted for through temperature-dependent microscopic and macroscopic cross sections. The cross sections are updated with time as local temperatures and densities changes. In the point kinetics solution, the initial flux shape is used throughout the entire transient calculation. Time-dependent point kinetics parameters are computed by means of first-order perturbation theory. The initial flux shape, determined with a given external source distribution, and the initial λ-mode adjoint flux are used along with macroscopic cross sections to compute time-dependent kinetics parameters, especially the reactivity parameter which reflects the thermal feedbacks. The adjoint flux is required in the evaluation of the scalar products used in the calculation of the time-dependent kinetics parameters. It corresponds to the initial source-free mathematical nodal adjoint solution [23]. The direct solution technique does not require the formulation of kinetics parameters and adjoint fluxes. The great advantage of the direct solution is that an unambiguous and “exact” solution of the inhomogeneous time-dependent group diffusion equation is obtained, in that sense that no approximations is introduced other than space nodalization and time differencing.

4.1.4 Numerical Results

Numerical experiments were carried out on a minor-actinide loaded and lead-bismuth cooled ADS. The test results suggest that the point kinetics approximation is capable of producing highly accurate results for many types of transients in ADS’s. For accidents involving external source perturbations the point method provided extremely accurate results, see Figure 4.2 and Figure 4.3. Such changes are associated with spatially uniform reactivity feedbacks that produce little flux deformation. It is expected that source disturbances be rather well described by point kinetics.

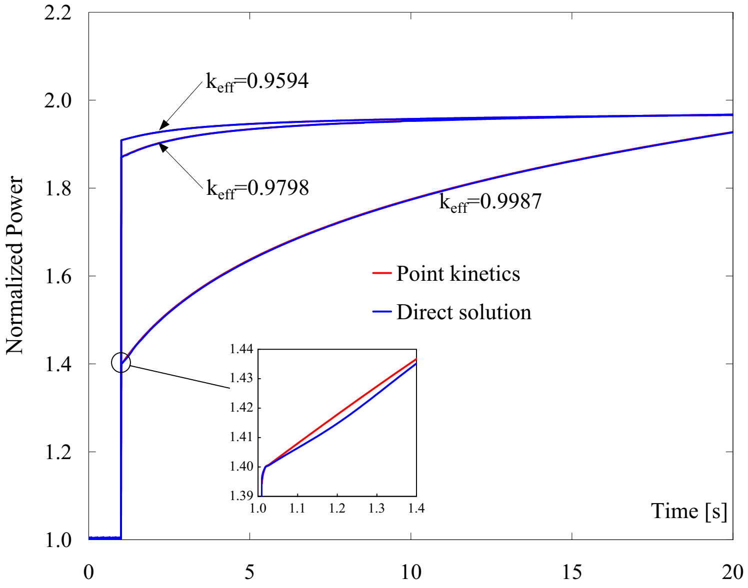

Figure 4.2 Beam overpower transient

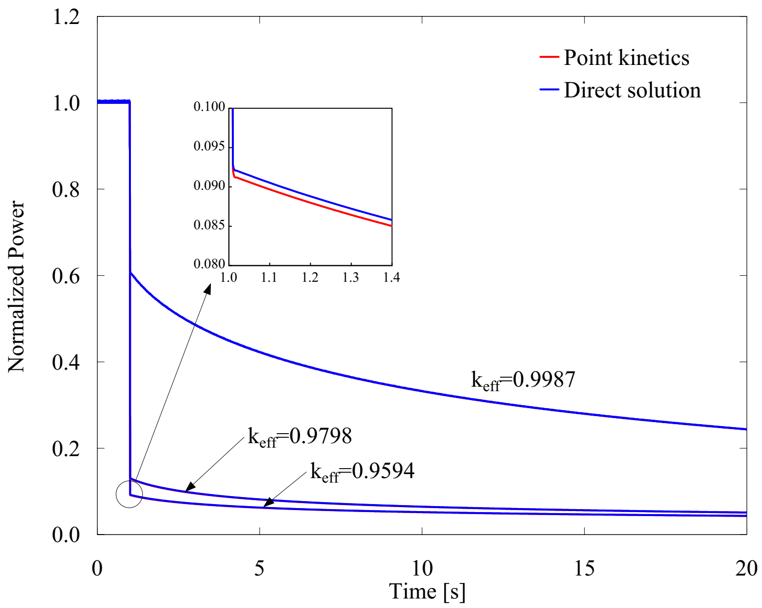

Figure 4.3 Beam trip transient

When applied to the analysis of localized reactivity perturbations - a condition when the point treatment is expected to be a poor approximation - the results indicated better precision at lower k_{eff} levels, see Figure 4.4 and Figure 4.5. This behaviour appears to be due to the lower reactivity sensitiveness in the subcritical operating state, which effectively weakens the response and mitigates any spatial distortions.

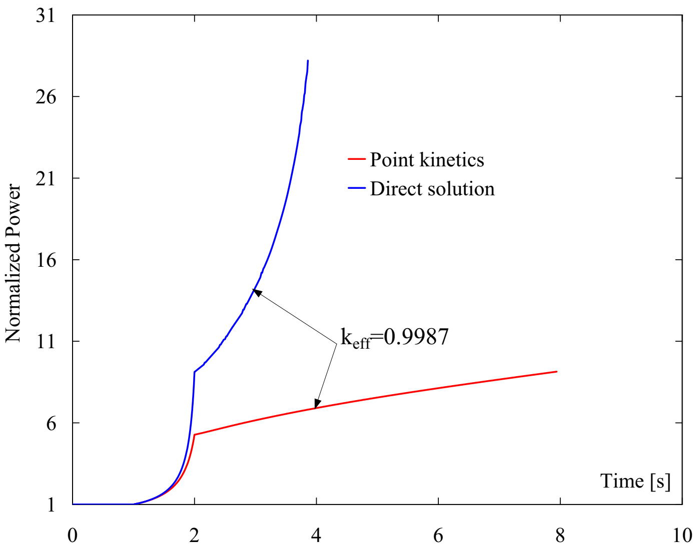

Figure 4.4 Reactivity insertion near core-center (k_{eff}=0.9987). Subassembly no. 4, in accordance with Figure 4.1, is fully withdrawn at initial conditions and is suddenly inserted during operation.

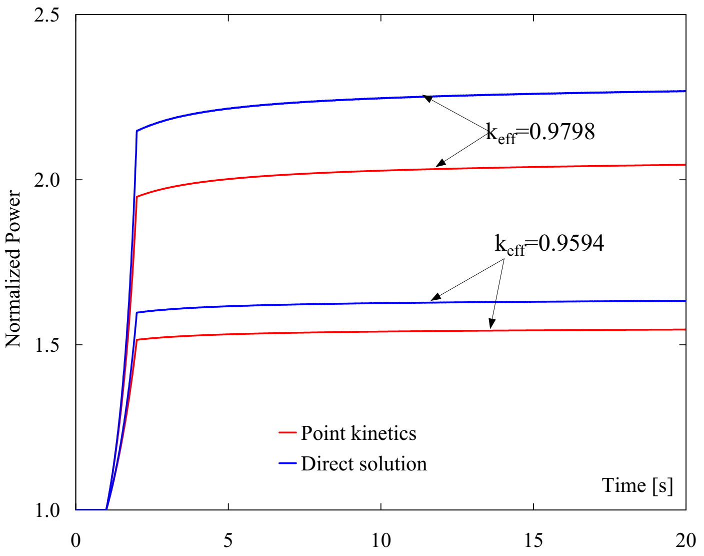

Figure 4.5 Reactivity insertion near core-center (k_{eff}=0.9594 and k_{eff}=0.9798). Subassembly no. 4, in accordance with Figure 4.1, is fully withdrawn at initial conditions and is suddently inserted during operation.

The situation in a loss-of-flow scenario was also studied. Here again, the point method was capable of very accurate calculations. The reasons are similar to those previously discussed. It was also found that the point kinetics model has a tendency to underestimate the severity of reactivity insertion accidents, see Figure 4.6 and Figure 4.7. The same nonconservative behaviour is observed in critical systems, but it ought to be recognized for subcritical systems as well because of its overriding importance in reactor safety considerations.

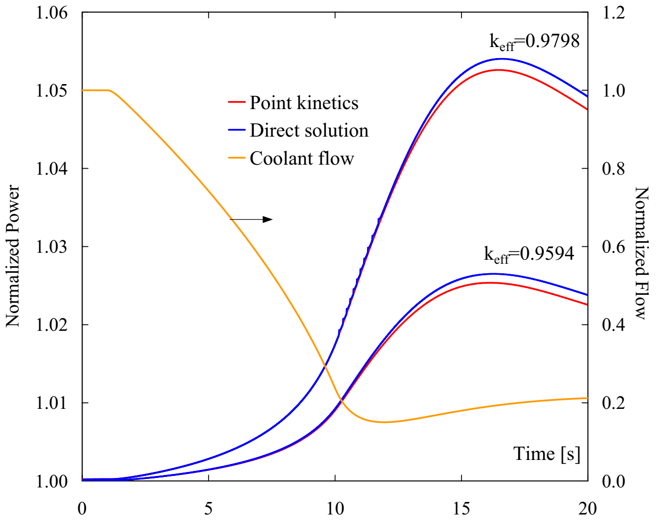

Figure 4.6 Loss-of-flow (k_{eff}=0.9594 and k_{eff}=0.9798)

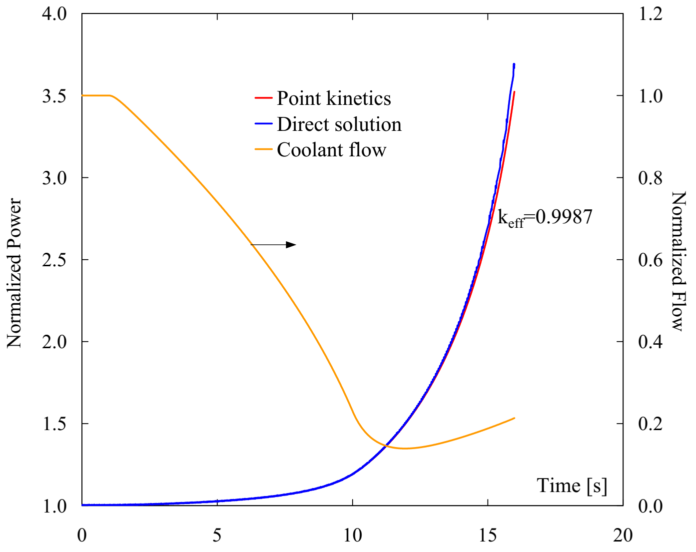

Figure 4.7 Loss-of- flow (k_{eff}=0.9987)

4.1.5 Concluding Remarks

The point kinetics approximation is capable of providing highly accurate calculations in subcritical systems. The results suggest better precision at lower k_{eff} levels. It was found that subcritical operation provides features that are favorable from a point kinetics view of application. Reduced sensitivity to system reactivity perturbations effectively mitigates any spatial distortions. Because a source-driven subcritical reactor approaches a stable level rather than exponential response behaviour, the error of the point kinetics method becomes essentially bounded. These characteristics, together with an overall smaller influence of delayed neutrons, and a typically strong space-time coupling in ADS's are all favourable from a point kinetics view of application. A possible non-favourable feature, but not apparent in these simulations, is that proposed ADS designs generally have large reactivity potential vested in the core [24]. Changes in lattice geometry or coolant density [25] may contribute with significant reactivity values. Such feedbacks are potential sources of spatial effects, and therefore, possible deviation from the point kinetics model. The essential requirements for an accurate point kinetics treatment of subcritical as well as critical reactors are symmetric reactivity insertion, small and tightly coupled core. Thus, favourable point kinetics performance in an ADS appears to be possible as long as the transient does not involve significant shape distortions. While the current study suggests that subcritical operation may provide for improved point kinetics performance and enhanced tolerance to system reactivity perturbations, the results showed that it should still be used with care for local reactivity perturbation studies and in situations involving strong feedback phenomena.

5 ADS SAFETY STUDIES ADS SAFETY STUDIES – PASSIVE AND INHERENT SAFETY MECHANISMS

OVERVIEW

The doctoral dissertation called ‘Passive and Inherent Safety Mechanisms applied on a Pb/Bi-cooled Accelerator-Driven System’ has been defended in May 2003 – see Appendix 1.

Two papers have been published describing main results of the safety studies. A paper called “Safety Aspects of Larger Heavy Metal-Cooled Accelerator-Driven Systems” (Appendix 8) and “Comparison of Safety Performance of Pb/Bi-cooled Accelerator-Driven Systems for two heat-exchanger locations and two power levels” (Appendix 9)

ADS safety studies have been devoted in this part to the investigation of passive safety and inherent features of subcritical nuclear transmutation systems - accelerator-driven systems. The general objective of this research has been to improve the safety performance and avoid elevated coolant temperatures in worst-case scenarios like unprotected loss-of-flow accidents, loss-of-heat-sink accidents, and a combination of both these accident initiators.

The specific topics covered are emergency decay heat removal by reactor vessel auxiliary cooling systems, beam shut-off by a melt-rupture disc, safety aspects from locating heat-exchangers in the riser of a pool-type reactor system, and reduction of pressure resistance in the primary circuit by employing bypass routes.

The initial part of the research was focused on reactor vessel auxiliary cooling systems. It was shown that an 80 MWth Pb/Bi-cooled accelerator-driven system of 8 m height and 6 m diameter vessel can be well cooled in the case of loss-of-flow accidents in which the accelerator proton beam is not switched off. After a loss-of-heat-sink accident the proton beam has to be interrupted within 40 minutes in order to avoid fast creep of the vessel. If a melt-rupture disc is included in the wall of the beam pipe, which breaks at 150 K above the normal core outlet temperature, the grace period until the beam has to be shut off is increased to 6 hours. For the same vessel geometry, but an operating power of 250 MWth the structural materials can still avoid fast creep in case the proton beam is shut off immediately. If beam shut-off is delayed, additional cooling methods are needed to increase the heat removal. Investigations were made on the filling of the gap between the guard and the reactor vessel with liquid metal coolant and using water spray cooling on the guard vessel surface.

The second part of the studies was focused on examinations regarding an accelerator-driven system also cooled with Pb/Bi but with heat-exchangers located in the risers of the reactor vessel. For a pool type design, this approach has advantages in the case of heat-exchanger tube failures, particularly if water is used as the secondary fluid. This is because a leakage of water from the secondary circuit into the Pb/Bi cooled primary circuit leads to upward sweeping of steam bubbles, which would collect in the gas plenum. In the case of heat-exchangers in the downcomer steam bubbles may be dragged into the ADS core and add reactivity. Bypass routes are employed to increase the flow speed in loss-of-flow events for this design. It has been shown that the 200 MWth accelerator-driven system with heat-exchangers in the riser copes reasonably well with both a loss-of-flow accident with the beam on and an unprotected loss-of-heat-sink accident. For a total-loss-of-power (station blackout) and an immediate beam-stop the core outlet temperature peaks at 680 K. After a combined loss-of-flow and loss-of-heat-sink accident the beam should be shut off within 4 minutes to avoid exceeding the ASME level D of 977 K, and within 8 minutes to avoid fast creep. Assuming the same core inlet temperature, both the reactor design with heat-exchanger in the risers and the downcomers have similar temperature evolutions after a total-loss-of-power accident.

A large accelerator-driven system of 800 MWth with a 17 m tall vessel may eventually become a standard size. For this higher power ADS, the location of the heat-exchangers has greater impact on the natural convection capability. This is due to that larger heat-exchangers have more influence on the distance between the thermal centers during a loss-of-flow accident. The design with heat-exchangers in the downcomers, the long-term vessel temperature peaks at 996 K during a loss-of-flow accident with the beam on. This does not pose a threat of creep rupture for the vessel. However, the location of the heat-exchangers in the downcomers will probably require secondary coolant other than water, like for example oil (for temperatures not higher than 673 K) or Pb/Bi coolant.

Details of the studies are attached in the Appendix 1.

6 FUEL DEVELOPMENT FOR ADS

PRELIMINARY SAFETY REPORT OF INERT MATRIX FUELS

6.1 INTRODUCTION

Fuels for transmutation reactors must, by their very purpose, contain no uranium, but significant amounts of plutonium and minor actinides (Np, Am, Cm). Generally, such fuels suffer from poor thermal properties; the thermal conductivity and the melting point of plutonium and minor actinide fuels are lower compared to their uranium-based equivalent. Thus, new fuel concepts, sometimes entitled dedicated fuels, are sought to better suit the requirements of a plutonium and minor actinide burning strategy. In this regard, inert matrix fuels, i.e., fuel supported by an inactive material acting as a diluent, are considered that would help to improve the thermal performance. An inert matrix helps to limit the power density, which permits lower fuel operating temperatures. Various concepts, in terms of fuel material (metal, oxide, nitride) and form (solid solution or composite) and choice of diluents, are being investigated, but the ultimate selection is not yet made. In Europe, the leading fuel candidates are oxides and nitrides. Interest in oxide fuel is promoted by experience gained from this type of fuel in fast reactor programs and in the development of fuels for light water reactors. For the oxide transmutation fuels, both composite fuels, like ceramic-metallic and ceramic-ceramic mixtures, and solid solution fuels are possible. However, composite oxide fuels are of main interest because of the possibility of offering higher thermal conductivity. Nitride fuel remains as a promising alternative in the development of fuels for minor actinide burning, yet the knowledge on nitride fuels is limited compared to the extensive experience available on oxide fuel. Nitride fuels offer relatively high thermal conductivity and high dissolution in nitric acid, which makes it compatible with the PUREX reprocessing technique. A drawback of the oxide fuels is that the solubility in nitric acid decreases as the concentration of plutonium increases. Nitric acid is the standard solvent for the PUREX process. The nitride fuels presently under consideration are of the solid solution type; composite nitride fuels have so far gained little interest. A specific problem of the nitrides is the production of radioactive ^{14}C by (n,p) reaction in ^{14}N during reactor operation. ^{14}N constitutes 99.6% of natural nitrogen (0.4% is ^{15}N). Presence of ^{14}C increases the radiation hazard and makes the fuel more difficult to handle during reprocessing. For that reason, it is considered necessary to employ enriched ^{15}N in the fabrication of nitride fuels. Most of this nitrogen can, however, be recovered in the reprocessing stage, either in a PUREX process or in a pyrochemical process.

In the present work three fuels are investigated from the point of view of safety performance during reactor operation. The objective is to assist in the feasibility study of these fuels and provide additional information for selecting the most promising fuels.

6.2 INERT MATRIX FUELS WITH MO, MGO, AND ZRN DILUENTS

Two oxide fuels and one nitride fuel are considered in this study, namely: an oxide-metal composite (cermet) fuel where the plutonium and minor actinides, $(Pu_{0.4},Am_{0.5},Cm_{0.1})O_{2-x}$, are dispersed in a molybdenum (Mo) matrix and an oxide-oxide composite (cercer) in which the actinides are dispersed in a magnesium oxide (MgO) matrix. The nitride fuel under consideration is dissolved in a zirconium nitride (ZrN) matrix. The current set of fuels including many others is examined at various laboratories and in joint European programs [27]-[29]. There are several reasons for studying these fuels. Neutronic considerations are of particular concern. These requirements, including void reactivity effects, are treated in more detail in a separate study [30]. Table 6.1 lists the investigated fuels together with relevant details of their composition and design characteristics. Fuel assembly characteristics are inherited from neutronics design studies. The current study compares the thermal performance for two pin diameters (D_{out}=5.7 mm and 6.8 mm) and two lattice configurations (P/D=1.50 and 1.75). Specifications shown in Table 6.1 correspond to a pitch-to-diameter ratio of 1.50 with an outer pin diameter of 5.7 mm. Ac denotes the actinide fuel composition, i.e., 40%Pu, 50%Am and 10%Cm. The oxide fuel is hypostoichiometric with an oxygen-to-metal ratio=1.90 and it is referred to as $AcO_{1.9}$.

Table 6.1: Fuel assembly specifications

Fuel	$AcO_{1.9}$+MgO	$AcO_{1.9}$+Mo	(Ac,Zr)N
Fuel type	Cercer Composite	Cermet Composite	Nitride Solid solution
Linear power (pin average), W/cm	250	350	350
Linear power (max flux plane), W/cm	350	480	480
Average inert matrix fraction$^+$	0.58	0.49	0.67
Minimum inert matrix fraction^a	0.42	0.37	0.55
Fuel pellet porosity (%)	5*	10**	15
Smear density (%)	91	88	82
Fuel assembly (lattice/FTF/pins)	Hex/10cm/127	Hex/10cm/127	Hex/10cm/127
Pitch-to-diameter ratio	1.50	1.50	1.50
Active core length, cm	100	100	100
Coolant velocity, m/s	2.5	2.5	2.5
Outside pin diameter, mm	5.7	5.7	5.7
Initial fuel-clad radial gap, μm	50	100	50
Fuel-clad bond	He	He	He
Cladding/structure material	15-15Ti	15-15Ti	15-15Ti

*5% porosity of both phases

**Refers to the porosity of the oxide phase. The metallic phase is fully dense (100% TD).

[+] Matrix fraction in the middle zone

[a] Refers to the matrix fraction in the outer zone

Fuel and diluent are mixed in proportions to obtain a core multiplication factor equal 0.97. The design procedure is not discussed here (see chapter on neutronics studies of

ADS fuels in this report for further reference). As shown in 0, it results in fuels having different inert matrix concentrations. The maximum amount of diluent is limited by neutron absorption properties. The core is partitioned into three regions of different matrix fractions. The purpose is to level out the radial power distribution. As a result, the fuels with the lowest concentrations of diluent are located in the outermost region. It is desirable to have as high volume fraction of diluent as possible. For the composite fuels, the diluent must typically predominate in volume for the matrix to respond as a continuous network. Similar amounts are also required to facilitate fuel fabrication. This becomes of particular concern for the Mo-cermet fuel since the minimum fraction of diluent for some pin configurations are too low. To some extent a higher diluent fraction can be accommodated through design modification, e.g., keeping a tight pin lattice and use of larger pin diameters. However, higher void value and larger coolant ΔT are two side effects. Other ways to allow for larger amount of diluent include modifying the actinide composition, but it has negative impact on burnup reactivity management.

The low thermal conductivity of the MgO-cercer fuel constraints the allowable linear power. Normally, oxide fuels can compensate this to some degree by having a high melting point; however, complications arise due to a low solid solubility of the oxide fuel particles in MgO. Eutectic reaction appears to occur at much lower temperatures, below the melting points of individual components: AcO_2 and MgO. For that reason, the MgO-cercer fuel is required to operate at lower linear powers; 25 kW/m compared to 35 kW/m for the cermet and the nitride fuel, respectively. Lower linear power has some obvious penalties since it requires that more pins are present for a given total power and hence larger core size. As a result, larger fuel volumes must be stored and reprocessed and more pins needs to be re-fabricated in each step. Besides economic disadvantages, it is has safety consequences on reactor operation because reactivity void worth’s tend to increase as the neutron leakage component diminishes for larger core sizes.

The oxide fuels may be fabricated with a rather low porosity. The MgO-cercer fuel has an as-fabricated porosity of 5%. The porosity of the oxide phase for the Mo-cermet fuel is purposely made greater (10%) to compensate for a lower swelling accommodation in the metallic phase, which is fully dense. The nitride fuel is fabricated with 15% porosity to accommodate a higher fission product swelling rate. Lower operating temperature and smoother temperature gradients of nitride fuels causes greater fission product retention compared to oxide fuels.

Molybdenum has been used as small addition in metallic uranium alloys to improve their swelling behavior [31]. However, very little information is yet available for Mo-cermet fuels. Fabrication tests [32] of Mo-cermet fuels showed promising results with cerium acting as a surrogate of the minor actinides. But yet no experience exists for AcO_{2-x}+Mo cermets. Issues that need to be answered are: material properties and thermal stability, irradiation resistance and swelling behavior, compatibility with cladding material and coolant. The principal problems of metallic fuels are related to the irradiation-swelling rate. Metallic fuel suffers from very high swelling rates. In practice, such fuel is limited to low burnup levels. The swelling can be accommodated if the fuel pin is fabricated with a low smear density, e.g., the fuel-cladding gap is made large enough. It is noted that no controlled fuel porosity can be built into a metallic fuel during fabrication. For cermets the as-fabricated porosity in the oxide phase allows for additional fission gas accommodation. Because molybdenum is a very hard metal it is likely that the mechanical interaction with the cladding may be more severe. Its hardness and a possible higher swelling rate led to the decision of increasing the initial fuel-cladding gap. It is currently twice as large (100 μm) for the Mo-cermet compared to the MgO-cercer and the nitride fuel pin. Such a gap allows the Mo-cermet fuel to swell to about 13% increase in volume before fuel-cladding contact. A different option could be to provide an axial hole in the pellet to facilitate swelling internally, however, this may become of concern for fabrication and so far the performance has not been investigated in any more detail. The smear density for the cercer, cermet, and the nitride fuels are 91%, 88%, and 82%, respectively. All three fuels are assumed to be helium-bonded (λ_{He}=0.36 W/mK at 1000 K).

Previous studies [33] have indicated that there are limited number of inert matrices suitable for nitride fuels; promising candidates, however, appear to be zirconium nitride (ZrN) and aluminum nitride (AlN). While AlN is not dissolvable in the actinide nitrides, ZrN forms a solid solution. Although AlN may improve the thermal conductivity somewhat (36 W/mK at 1000°C), insolubility introduces other difficulties, e.g., complicates the fabrication process and affects the dimensional stability. At this point ZrN is our primary choice for diluent. ZrN offers relatively high thermal conductivity (23 W/mK at 1000°C) and high melting point (2960°C). It has a stabilizing effect on plutonium and americium nitride and is itself stable in air (no oxidation). Furthermore, it has a high transparency to neutrons, has good chemical compatibility with steel cladding and it is solvable in nitric acid.

6.3 MATERIAL PROPERTIES

In discussing the minor actinide (MA) fuels, it should be realized that material property data is limited, particularly at high temperature. Thus, safety assessments become subject to large uncertainties. Thetford and Mignanelli [34], [35] have recommended preliminary correlations based on existing data for oxide and nitride MA fuels. These correlations have been used in the present work with minor modification. In general, the effects of temperature, matrix fraction, oxygen content, and porosity are taken into account. We will discuss these effects in the following section, with emphasis on the thermal conductivity. Where the required the data is missing, the models are based on rational assumptions. Material properties will change during irradiation, due to the effect of restructuring and fission product swelling. However, due to the limited amount of experimental information on irradiation effects our study is limited to embrace only fresh fuel properties.

Selected physical properties are presented in Table 6.2. The values are given at 100% theoretical density at 1000°C. Compositions correspond to the intermediate core zone.

Table 6.2: Thermophysical properties of investigated fuels.

Fuel material	Melting points, K	Properties at 1000^{o}C (100% TD)			Mean thermal expansion coefficient^a, 1e+6/K
		Density, g/cm^3	Thermal conductivity, W/mK	Specific heat, kJ/kgK	
$AcO_{1.9}$+49%Mo	2640*	10.62	51.2	0.33	9.2
$(Ac_{0.33},Zr_{0.67})N$	2200**	9.29	17.0	0.43	9.0
$AcO_{1.9}$+58%MgO	2200-2300$^+$	6.57	4.7	0.90	14.0

*No eutectic melting. Melting point of $AcO_{1.9}$ is 2640 K. Pure molybdenum melts at 2896 K.

**Dissociation temperature of AmN nitride fuel in 1% nitrogen gas.

$^+$Eutectic reaction between MgO and AcO_{2-x}. The melting point for pure MgO is 3100 K.

^{a}Mean linear coefficient of thermal expansion between 300 to 2100 K.

Relative to Mo-cermet and nitride, MgO-cercer has a higher coefficient of thermal expansion, which tends to increase the negative reactivity feedback due to fuel axial expansion in an overpower transient and may increase thermal stress cracking in the fuel. MgO-cercer also has considerably lower thermal conductivity, lower density, and a much higher specific heat.

In discussing physical properties of the nitride-based fuel, it should be realized that the data for AmN contain large uncertain. The most notable omissions are thermal conductivity, linear expansion, and specific heat. Information on (Pu,Am)N is essentially obtained from extending known data for (U,Pu)N and pure PuN. The recommended values for (Pu,Am,Zr)N is found by combining the actinide and zirconium data weighted by their respective volume fractions, i.e., Vegard’s law. Thetford and Mignanelli [34] recommend the use of thermal conductivity data for (U,Pu)N as replacement for ZrN. The correlation is adjusted for the fact that the thermal conductivity of actinide nitride decreases with increasing atomic number [36]. Given the lack of experimental data at high temperatures, the correlations are extrapolated for temperatures beyond 1600 K.

6.3.1 Thermal conductivity

The thermal conductivity is a key property in the fuel selection process. It is of fundamental importance for the safety of the entire reactor. It essentially determines the allowable power rating and the margin to melting Figure 6.1 shows the thermal conductivity of the investigated fuels as function of temperature. Values are given for the porous composition.

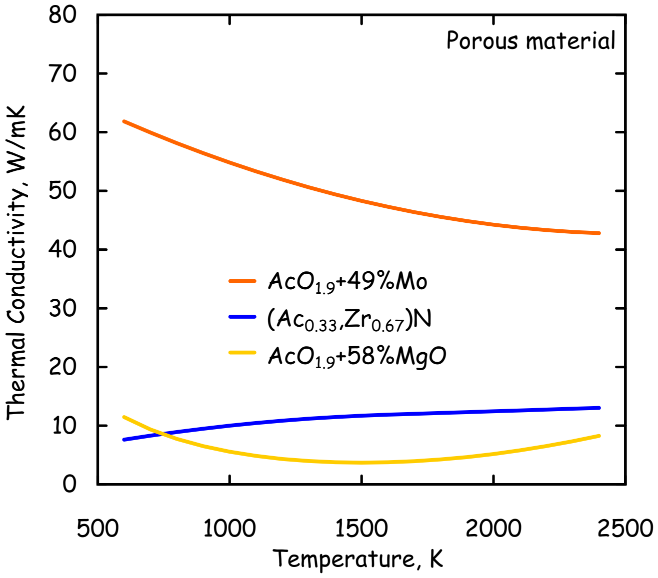

Figure 6.1 Thermal conductivity of porous fuel as function of temperature.

The Mo-cermet fuel has excellent thermal conductivity. The thermal conductivity of the nitride fuel is quite high, about 2-3 times higher than the MgO-cercer fuel but only about 20-30% of that of Mo-cermet. There is no systematic variation of the thermal conductivity with the temperature. The thermal conductivity of the MgO-cercer fuel shows a similar behavior as classical MOX fuels, i.e., decreasing at low temperatures and increasing at high temperatures. It is noteworthy that thermal conductivity of MgO [37]exhibits similar shape dependence, with a minimum around 1500 K. For the nitride fuel, the thermal conductivity increases with temperature, but it has been shown that the slope decreases for higher plutonium content [38]. For the Mo-cermet fuel, the thermal conductivity is determined primarily by the molybdenum conductivity, which decreases with temperature. Decreasing thermal conductivity with increasing temperature is a disadvantage from a safety point of view.

A certain amount as-fabricated porosity is desirable to manage fuel swelling during irradiation. Porosity affects fuel properties; in particular it reduces the thermal conductivity. A common method to treat the effect of porosity on thermal conductivity is the Maxwell-Eucken model:

$$\lambda(p) = \lambda_{100\%} \frac{1-p}{1+\beta p}$$

Where $\lambda(p)$ is the effective thermal conductivity, $\lambda_{100\%}$ is the thermal conductivity corresponding to the fully dense material, β is a pore shape factor and p is the fractional porosity. A shape factor of $\beta=2$ has been recommended for the present fuels. Depending on the pore geometry, which depends on the fabrication process, various modifications of the Maxwell-Eucken model exist. The MgO-cermet fuel has a bulk density of 95% of the theoretical value. Hence the correction factor for the thermal conductivity is 0.864. For the Mo-cermet fuel the as-fabricated porosity has a limited effect on the overall conductivity as it is primarily determined by the metallic component, which is fully dense. The porosity has a significant effect on the conductivity of the low-density nitride fuel. The effective thermal conductivity of the nitride fuel is reduced to 65% of the fully dense material.

In Figure 6.2, the temperature is held constant at 1000°C and the fraction of diluent is varied, which shows the effect of the matrix content on the thermal conductivity. The combined thermal conductivity of the diluent and fuel is calculated using Vegard's law. We recognize that this is a crude approximation and not necessarily appropriate, but in the absence of better data, we are compelled to accept it until more information become available. Not surprisingly, the thermal conductivity is an increasing function of matrix content. Because of the Vegard's law approximation, the thermal conductivity is a linear function of the amount of diluent. The deviation from the Vegard's law for the nitride fuel is the result of a correction applied by Thetford and Mignanelli [35] to account for decreasing thermal conductivity with increasing atomic number of the actinide element. It was mentioned earlier that there are three zones of different matrix fraction in our model of the core. Suggesting that the fuel thermal conductivity depends on the location in the core. In the thermal analysis, the fuel assemblies with the lowest matrix content, i.e., the outermost assemblies will produce the highest fuel temperatures and these are used in the design evaluation.

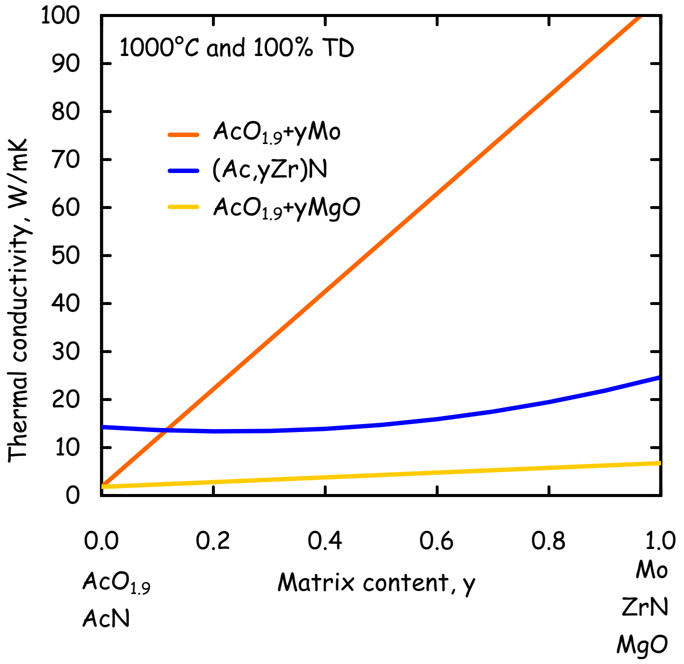

Figure 6.2 Thermal conductivity of actinide oxide fuel and actinide nitride fuel as function of matrix content.

Oxygen deficiency in the actinide fuel oxide phase is desirable because it reduces the oxygen chemical activity inside the pin, such that cladding corrosion is reduced and therefore the wastage can be less. Reduction of the oxygen-to-metal ratio is accompanied by a decrease of the thermal conductivity. This is illustrated in Figure 7.3 for AcO_{2-x}. It is seen, that the effect is notable at low temperatures (<2000 K). As the oxide fuel is mixed with diluents, the O/M effect becomes less influential because of lower relative contribution of the oxide part. For the Mo-cermet fuel the effect becomes negligible.

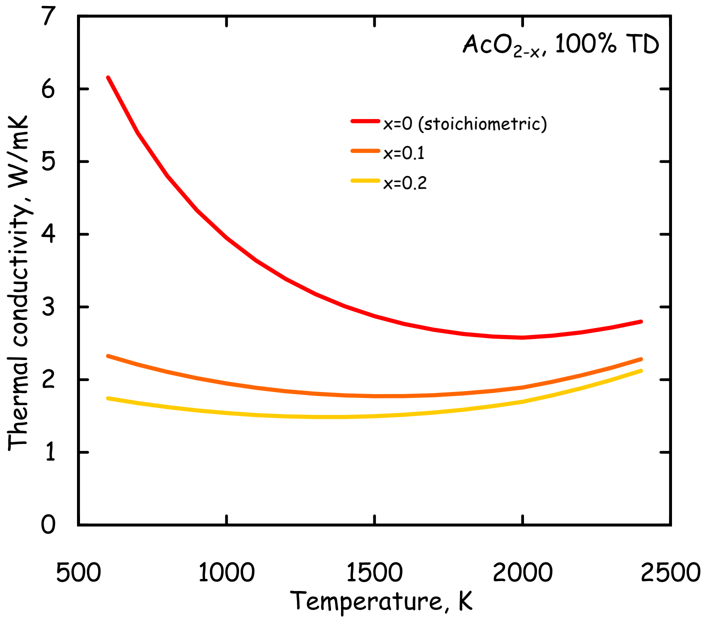

Figure 7.3 Effect of oxygen-to-metal ration on the thermal conductivity of AcO_{2-x}.

7.4 TEMPERATURE CONSTRAINTS

7.4.1 Fuel

The melting point of $AcO_{1.9}$ is estimated to 2640 K, using the melting point of PuO_2 as 2663 K [39], and AmO_2 and CmO_2 as 2783 K and 2838 K [40], respectively, and applying Vegard's law. It was further assumed that the melting point dependence on the oxygen content was similar to the recommendations for $(U,Pu)O_{2-x}$[41]. It appears that no eutectic reaction occur between molybdenum and UO_2. If a similar behavior is assumed for $Mo+AcO_{1.9}$, then melting will occur first in the oxide phase. It should be noted, however, that the fluid-like behavior might appear either at the lower or the higher temperature, depending on the volume fraction of molybdenum. It is recognized that the oxygen content may affect the possibility of eutectic melting and also oxidization of Mo into MoO_2, but this has not been taken into account in this study. For the $MgO\text{-}AcO_{2-x}$ fuel, complication arises due to the possibility for eutectic melting below the melting points of AcO_2 and MgO (3100 K). Laboratory measurements [42] found no eutectic reaction up to ~1923 K, while theoretical calculations [43] predicted that eutectic may start to form at temperatures as low as 1930 K for low oxygen contents. The same study also estimated that the melting point stabilizes around 2300 K for oxygen-to-metal ratios above 1.62. Keeping low oxygen content, however, is desirable because it reduces corrosion of the cladding. The melting point of $MgO-PuO_{2-x}$ [44] ranges from 2341 to 2503 K when the oxygen content changes from 1.61 to 2. Following these results, and keeping in mind that significant uncertainties exist in the thermodynamic modeling data, we have assumed that melting of $MgO+AcO_{1.9}$ is onset in the range of temperatures 2200-2300 K.

Americium nitride may decompose into actinide metal and nitrogen gas at relatively low temperatures. It should not influence normal operation, but it raises safety questions regarding the stability in thermal upset conditions. In an inert gas environment, it has been observed that thermal decomposition of AmN occurs for temperatures above 1600 K. However, it has been noted that ZrN has a stabilizing effect on the vaporization behavior of plutonium and americium nitride. Given that more than 50% of ZrN is dissolved in solid solution with plutonium and americium suggest that the material properties may resemble ZrN rather than pure AmN. Furthermore, it is found that decomposition is suppressed in a nitrogen atmosphere. Recent calculations have estimated that the onset for decomposition may increase by 250 degrees if the pin fill-gas contains a certain concentration of nitrogen [45]. These conditions led to a preliminary assumption that the temperature of $(Ac_{0.33},Zr_{0.67})N$ should not exceed 2200 K under any circumstances (accidental conditions). It should be noted that the reliance on a sealed nitrogen atmosphere might become a safety matter if a breach would occur in the cladding that would allow the nitrogen gas to escape the pin. The safety merits of such design solutions to enhance the fuel stability are subject to further investigation. Efforts to increase the understanding of the mechanisms of nitride dissociation are underway. It is essential that these effects be known precisely to demonstrate a safety performance based on realistic limits.

7.4.2 Cladding

Swelling and degradation of mechanical properties due to fast neutron irradiation are life-limiting factors for the structural materials. In the following evaluation, three stainless steels are discussed as candidate materials for fuel cladding. The 316 SS material is included because it is reference stainless steel cladding for fast reactor applications. It has been studied extensively over the years and large amount of transient/mechanical properties data exists for this material. However, standard 316 SS is susceptible to radiation damage that results in dimensional instability and embrittlement of structural components. It suffers from unacceptable swelling for doses above 50 dpa. For that reason, 316 SS has been abandoned as cladding material for long term application in fast reactors. Advanced austenitic stainless steels have been developed that withstand doses up to 150 dpa. Ti-modified 316 and CW15-15Ti austenitic steels have been used as cladding in the French fast reactors Phénix and Superphénix. The best irradiation performance has been achieved with Si-modified 15-

15Ti stainless steel. The third cladding material discussed is the ferritic stainless steel alloy HT-9. This class of alloy is primarily studied as an option for enhancing the material's irradiation resistance. HT-9 has shown excellent swelling resistance to doses up to 200 dpa. However, it has limited high temperature mechanical properties. The mechanical strength decreases drastically for temperatures above 500°C. This has notable impact on the maximum allowable cladding temperatures during normal and off-normal conditions. For this reason, austenitic alloys have typically been used for high temperature core applications rather than ferritic steels. The choice of ferritic steels has traditionally focused on their application for wrapper tube and duct material because of lower operating temperatures of these components. The burnup potential of the current set of fuels as limited by cladding radiation damage can be estimated [30] based on the specified material dose limitations and on the fact that a fast neutron fluence (>0.1 MeV) of 10^{22} n/cm^2 correspond to approximately 5 dpa in steel [46]. It is found that the burnup potential is approximately 32%, 25%, and 9% using HT-9, 15-15Ti, and 316 SS, respectively.

Failure temperatures relevant for the fuel pin cladding during transient overpower conditions were estimated based on transient burst test data. This type of test, called Fuel Cladding Transient Test (FCTT), duplicate reactor transient conditions in which the cladding is heated until failure occurs. Results are normally presented as failure temperature as function of cladding hoop stress, and often the results are related to a particular thermal ramp rate. The FCTT tests are typically carried out for relatively fast ramp rates, in the temperature range 0.5-100°C/s. Cladding failure predictions based on FCTT data are less representative for very slow transients, e.g., decay heat transients, or transients held at elevated temperatures for long times. An extensive FCTT database has been accumulated on mechanical performance of irradiated and unirradiated 20% cold-worked 316 SS [47]-[49] and on HT-9 [50]. Some data is available for D9 stainless steel. For the current system, the temperature limits were established for a cladding hoop stress of 100 MPa and a thermal ramp rate of 5°C/s. The assumed hoop stress is based on a plenum pressure at end-of-life of 10 MPa plus 30% increased loading due to unforeseen stress phenomena (the hoop stress corresponding to an internal gas loading of 10 MPa is 74 MPa). The thermal ramp rate was chosen because it is similar to those of the transients involved. The FCTT limit approach was selected to define an ultimate failure limit for events of a very low probability of occurrence (worst-case conditions). For operational incidents and anticipated transients it is relevant to employ more conservative limits.

Early FCTT tests conducted on standard 20% CW 316 SS [48] showed remarkable degradation of transient burst temperatures of irradiated and fueled pins. It was attributed to the so-called Fuel Adjacency Effect (FAE) [52] as liquid metal embrittlement induced by the fission products of cesium and tellurium. Later [53], it was suggested that the observed reduction of ductility and strength was due to insufficient atmosphere control during specimen preparation and testing. Without atmosphere control and for fuel burnup exceeding 20 GWd/t, it was found that accumulated cesium in the fuel-cladding gap could react with moisture in the hot-cell atmosphere to form CsOH, which may induce stress corrosion and cause premature failure. Transient burst tests of CW 316 SS conducted in atmosphere-controlled environment [54] gave further proof that the fuel adjacency effect may be negligible in the actual fuel pin environment. It was found that the failure temperature for 10% CW and 20% CW 316 SS irradiated in the range 30-90 dpa was comparable to unirradiated cladding.

Based on these studies, the failure temperature for the 316 SS cladding, under the assumed loading conditions, was established at 1060°C. For the HT-9 cladding, which is apparently not affected by FAE, as 316 and D9, but with much lower high temperature mechanical strength the failure temperature was established at 870°C. FCTT data for irradiated D9 stainless steel [51] was used to develop temperature limits for 15-15Ti steel. The D9 alloy is a titanium modified 316 stainless steel, which has similar composition as 15-15Ti steel. Apparently D9 exhibit similar failure temperature as 316 SS. No FCTT data has been found for 15-15Ti, however, tension tests [54] show that the mechanical properties of irradiated 15-15Ti is better than Ti-stabilized 316, indicating that transient/mechanical properties should be no less than D9.

Allowable cladding temperatures during normal operating conditions are established based on available stress rupture test data. Limited test data is available for CW15-15Ti, however, reasonable amount of data is available for D9 type steels. Considering the better tensile properties of CW15-15Ti suggests that the thermal creep performance of CW15-15Ti is comparable or better than CW D9. Tests conducted on 20% CW D9 cladding showed that the in-pile rupture lifetime is lower compared to out-of pile data [55], indicating that the pin cladding might fail sooner than predicted with out-of-core test results. Based on available data the maximum operating temperature for the CW15-15Ti cladding was set to 650°C (maximum midwall temperature). This integrity limit was determined for a constant plenum pressure loading of 10 MPa and an expected in-pile service of 3 years (exposure time 30,000 h). The calculated Larson-Miller Parameter (LMP) corresponds to $1.64 \cdot 10^{-4}$. Ongoing studies show that silicon modified CW15-15Ti stainless steel posses the best tensile properties indicating that further improvement of the thermal creep performance is possible. The experience is that D9 has better thermal creep properties than 20% CW 316 SS. The maximum temperature of the 316 SS clad under normal operating conditions is established at 600°C. As far as in-pile creep behavior of HT-9 is concerned, little information is available in the open literature. Based on empirical studies of unirradiated HT-9 [56] and on structural design criteria specified by the ASME code [57], the maximum operating temperature for the HT-9 cladding was set to 540°C. Clearly, the creep rupture strength of the austenitic alloys is superior to the ferritic; 316 has generally lower thermal creep rates than type HT-9.

Previous discussion concerned the irradiation and mechanical performance of cladding steels, which set constraints on the allowable radiation dose and temperatures during normal and accidental conditions. At the same time, external corrosion by Pb/Bi induces additional constraints. The effect of the corrosion attack on the cladding is manifest as wall thinning, higher stresses, and reduced fuel pin lifetime. The corrosion rate shows a strong dependence on temperature. It has been demonstrated [58] that the temperature limits for non-protected stainless steels are: 400°C for austenitic steels and 450°C for ferritic steels. However, the corrosion stability can be affected by the concentration of oxygen dissolved in the liquid metal. One finds that at a certain level of oxygen concentration a protective oxide film may form on the surface of the structure and substantially reduce further corrosion attack. The protective film is formed by oxidation reactions with the steel elements. The most common phases of the oxide films are M_3O_4 and M_2O_3, where M stands for elements with high affinity for oxidization, e.g., Fe, Cr, Si. Using this technique it is possible to increase the operating temperature by 150-200°C. In Russia, where most corrosion studies with Pb/Bi as coolant have been carried out, ferritic/martensitic steels have received particular interest. A particular reason is the low nickel content of ferritic steel compared to the austenitic steels [58]. Nickel shows high solubility in Pb/Bi alloy, which has an impairing effect on the oxide film. Developmental work in Russia has shown that addition of silicon to the steel help to increase the corrosion resistance at higher temperatures (>600°C). Laboratory tests conducted in the U.S. indicate similar results [59]. Still, according to Russian sources, it appears that operating temperatures around 650°C is suitable only for relatively short-term service application (≤5000 hours). In this study, the maximum temperature on the outer surface using HT-9 steel is limited to 600°C under normal operating conditions. It is cautioned that this limit is uncertain and may change as more data becomes available. Although, HT-9 has similar material composition as the Russian EP-823 steel, which has been studied extensively in corrosion tests [58] in the temperature range up to 620-650°C, it has lower content of silicon (0.3%wt) than the Russian steel (1.3%wt), which appears to have significant impact on the corrosion resistance. In general, the database on Pb/Bi corrosion performance of western steels is limited, especially when it comes to long-term operation. As was mentioned above, the austenitic steels appear to be less corrosion resistant than the ferritic steels. Thus, with reference to 316 SS and CW15-15Ti we have assumed that their admissible operating temperature on the outside of the cladding is 50 degrees lower than for HT-9. It is noteworthy, that the Si-modified CW15-15Ti derivative steel, which has shown promising dimensional and mechanical stability, also could be an interesting option in the context of corrosion resistance considering the apparent favorable effect of adding Si. However, considerably more operational data is required for most western steels before reliable information can be established regarding their long-term performance.

The corrosion rate increases with the fluid velocity. Theoretical modeling [59] suggests that the Pb/Bi corrosion rate is proportional to $V^{0.6}$, where V is the average turbulent fluid velocity. Increased corrosion is typically observed in hot spots and in locations with a disturbed flow pattern. But there are conflicting data regarding the recommended maximum flow velocity. Based on early corrosion tests with liquid bismuth [60] little increase in corrosion was observed when the velocity itself was increased from 1.5 m/s to 4.2 m/s. At IPPE in Russia, Pb/Bi corrosion tests with EP-823 steels have been carried out for flow velocities up to 3-3.5 m/s and exposure times of 5,000 hours and more. However, most authors recommend a maximum bulk velocity during normal operation somewhere in the range 2-2.5 m/s [61]. The maximum flow velocity in the pin bundle is set to 2.5 m/s in the current study.

0 summarizes the temperature constraints of the investigated cladding materials. It should be noted that the temperature limits are not universal; they are established for the current system in mind. The reason is that loading conditions, corrosion- and irradiation conditions, and design life vary between systems and therefore the temperature limits may be different even if the cladding material is identical. Temperature limits established for overpower events also take into account an expected frequency of occurrence and the thermal ramp rate and transient duration. The higher the occurrence probability of the incidents, the more conservative the safety margins must be.

Table 6.3: Stainless steel cladding performance data (temperatures given in °C).

Clad type	HT-9	316 SS	15-15Ti
Structure type	Ferritic	Austenitic	Austenitic
Irradiation resistance (max dpa)	200	50	150
Approx. burnup capability*, atom %	32%	9%	25%
Max midwall clad temperature** (overpower condition)	870	1060	1060
Max outer clad temperature$^+$ (normal operation)	600	550	550
Max midwall clad temperature^a (normal operation)	540	620	650

*Based on specified fuels and irradiation conditions (σ_f=0.66 b, 1e+22 n/cm^2=5 dpa in steel)

**Failure criterion based on transient burst limits (FCTT data).

$^+$Based on corrosion rate limitations.

^{a}Design criterion based on thermal creep limitations (time-to-rupture data).

6.4.3 Fuel Pin Thermal Analysis at Normal Operation

In Figure 6.4 the temperature profiles under normal operation are shown. The large fuel-clad gap of the Mo-cermet fuel is undesirable from a thermal point of view since it yields a very large temperature drop from the fuel surface to the cladding and it greatly increases the fuel centerline temperature (by approximately ~400 degrees compared to a gap size of 50 µm). This circumstance eliminates much of the advantage of the high conductivity cermet fuel. Use of a bonding material could significantly reduce fuel surface temperatures, but it would introduce new complications. It is seen that the MgO-cercer fuel has a steep temperature gradient in the fuel region (more than 300°C/mm). A number of phenomena are affected by the presence of a strong temperature gradient. Fuel restructuring (grain growth and pore migration) during operation and development of thermal stresses (cracking) are directly dependent upon temperature gradients. Thermal stresses are aggravated by a higher coefficient of thermal expansion. Restructuring usually takes place in oxide fuels and this can form a central void in the pellet early in the operating life. Much less restructuring occurs for nitride fuels. The very flat temperature gradient in the cermet fuel (approaching 50°C/mm) suggests low restructuring due to thermal effects but yet no in-pile experience exists. Restructuring affects fuel swelling and densification, thermal conductivity, and hence operating temperatures, and therefore it has an important role on the safety performance.

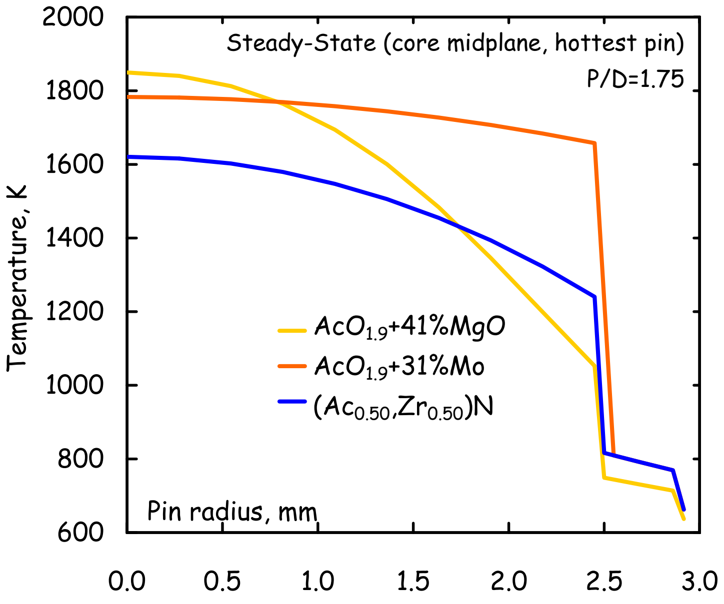

Figure 6.4 Radial temperature distribution in fuel pin

Fuel pin design temperatures shown in

Table 6.4 and Table 6.5 correspond to pitch-to-diameter ratios of 1.50 and 1.75, respectively. It is seen that under normal operating conditions the fuel temperature limits are much less restrictive than the cladding temperature constraints. For P/D=1.50, the cladding temperature (max at the top of the pin) becomes unacceptable with respect to coolant corrosion damage and it is also somewhat high considering long-term thermal creep performance. Because the MgO fuel is operated at a lower linear power, cladding temperatures are much lower. Maintaining a protective oxide surface layer on the cladding calls for reduced operating temperatures in return for longer lifetime of the cladding. This can be achieved by opening up the lattice of fuel pins to increase the coolant volume fraction or lowering of the linear power. Increasing P/D to 1.75 reduces the peak cladding temperature by approximately 100 degrees. Increasing the coolant velocity through the core is associated with increased wear of the oxide film. Novikova [61] recommends the circulation velocity not to exceed 2.5 m/s, which is the current operational setting.

Table 6.4: Temperatures at normal operation (temperatures given in °C). Results correspond to P/D=1.50.

Fuel	$AcO_{1.9}$+MgO	$AcO_{1.9}$+Mo	(Ac,Zr)N
Peak fuel temperature	1590	1520	1370
Peak clad outer temperature	540	640	640
Peak clad midwall temperature	550	650	650
Clad-coolant temperature drop (core midplane)	60	90	90
Coolant temperature rise	210	290	290
Thermal margin to fuel melting	340	850	560
Clad thermal margin (corrosion limit)	10	ua	ua
Clad thermal margin (thermal-creep limit)	100	0	0

ua=unacceptable

Table 6.5: Temperatures at normal operation (temperatures given in °C). Results correspond to P/D=1.75.

Fuel	$AcO_{1.9}$+MgO	$AcO_{1.9}$+Mo	(Ac,Zr)N
Peak fuel temperature	1580	1510	1350
Peak clad outer temperature	480	540	540
Peak clad midwall temperature	490	550	550
Clad-coolant temperature drop (core midplane)	80	110	110
Coolant temperature rise	130	180	180
Thermal margin to fuel melting	350	860	580
Clad thermal margin (corrosion limit)	70	10	10
Clad thermal margin (thermal-creep limit)	160	100	100

6.5 SUMMARY

The work presented so far contains a general discussion of a few selected plutonium- and minor actinide inert matrix fuels and their associated thermophysical properties. Temperature constraints are established for the fuel and cladding materials. It is recognized that the fuel material properties contain missing data. Thermal-hydraulics calculations have so far treated the fuel pin performance under normal operating conditions. The Mo-cermet fuel is clearly superior with regard to thermal conductivity, which indicates much better thermal performance, but yet very little information is available on its irradiation performance. Under normal operating conditions, the primary design constraint is due to the cladding temperature limits. The ferritic steels do not posses sufficient strength at high temperature operation whereas the austenitic steels are limited by radiation damage and coolant corrosion attack. Compared to austenitic stainless steel, ferritic/martensitic steels demand lower operating temperatures in return for improved cladding operating life. Standard 316 austenitic steel is not expected to survive the neutron doses and the corrosive environment anticipated for a lead/bismuth-cooled reactor. The CW 15-15Ti stainless steel is selected as cladding material because it has a proven irradiation resistance and reasonable knowledge is available on the mechanical performance of this type of steel. However, the maximum fluence of this steel may still remain below some goals and the Pb/Bi corrosion resistance is not known, so the choice may change as more data becomes available. In the next phase, the fuel pin performance will investigated during accident conditions. Safety analysis is conducted considering some typical accidents of interest in accelerator-driven systems.

7 MATERIAL STUDIES FOR ADS - MODELLING OF RADIATION EFFECTS ON MECHANICAL PROPERTIES OF FERRITIC STEELS.

In the frame of the European Project SPIRE – "SPallation and IRradiation Effects - "Irradiation Effects in Martensitic Steels under Neutron and Proton Mixed Spectrum" a work has been initiated to developed a set of EAM (Embedded Atom Method) - potentials for simulation of Fe-Cr alloys. This collaborative effort between KTH, UU, CNRS (Paris) and SCK-CEN (Mol) progresses very successful and has resulted in few important publications including 2 papers published in 2003.

7.1 INTRODUCTION

Mechanical properties of steels used as components in reactors are degraded due to effects of radiation, thermal ageing and thermo-chemical environment. Often threshold behaviours are observed, meaning that a component may have served without problem for many years, or even decades, before an abrupt change in ductility of volume takes place. These phenomena are further known to be dose rate dependent, meaning that accelerated irradiation tests often will give wrong predictions of limits to service life in a real reactor environment. This is especially trouble-some in light water reactors, where the threshold time for embrittlement or swelling to become significant is of the order of decades.

Therefore, it becomes important to obtain a basic understanding of the mechanisms responsible for the irradiation degradation of mechanical properties. Today this can be achieved for pure metals by means of computer modelling, using a multi-scale approach ranging from solutions of the Schrödinger equation to elasticity theory for macroscopic bodies.

In the present project, existing empirical models for pure elements like Fe are extended to the Fe-Cr-C system, which may serve as an idealised model of ferritic steels actually used for reactor components. By the end of the project, a so called ”Embedded atom method”, or EAM model for this system will have been developed, that is able to correctly reproduce elastic, thermophysical and point defect properties of this material out of pile, as function of Cr and C content. This model will be used for predicting the change of mechanical properties as function of irriadiation dose, dose rate and temperature. Comparison with relevant experimental data will then be made, to check the predictive power of the model. Finally, an evaluation of the applicability of the results with respect to real industrial ferritic steels will be attempted.

7.2 METHODOLOGY

In the EAM formalism, the total energy of a system is written as the sum of pairwise interactions and a many-body term given as function of electron density. Historically, EAM potentials describing the effective interaction between atoms of the same kind have been fitted to reproduce experimental data for lattice parameters, elastic constants, crystal structure and vacancy formation energies. In order to include information relevant for defect production in irradiated materials, the short range of the pair-potential has ben fitted to threshold energies for Frenkel pair production in electron irradiated speciments.

Several potentials for iron have been reported in the literature, which reasonably well reproduce the properties they were fitted to. However, none of them provides correct values for thermal expansion. In addition, only short range potentials, excluding the FCC lattice second nearest neighbour, could reproduce the relative stability of self-interstitials in different lattice directions. In order to obtain a better potential for iron, our group started out by fitting a long range pair potential to the measured thermal expansion coefficients of iron. Interestingly, it was found that the stability of the <110> interstitial was improved by this procedure, at the expense of increasing the absolute formation energy of the defect.

Chromium is anti-ferromagnetic and highly anisotropic at room temperature. Hence it was believed to be impossible for EAM potentials to reproduce its elastic properties. The latter fact has been considered to be a major obstacle for the applicability of the embedded atom method to simulation of Cr bearing steels. Examining the temperature dependence of the elastic constants, we however found that at higher temperatures, where chromium is paramagnetic, that the so called Cauchy pressure becomes positive, meaning that the EAM formalism may be applied. By thus fitting the Cr potential to the elastic constants of its paramagnetic state, we were able to obtain a potential reproducing elastic properties at $T > 450$ K. Since reactor components typically operate at even higher temperatures, we believe that results obtained in simulations using this potential should be relevant. Further, it is known that the addition of just a few percent of iron to chromium makes the alloy paramagnetic at room temperature. Hence our Cr potential should well describe the behaviour of Cr in the alloy at all temperatures of interest.

Mixed pair potentials, i.e. potentials describing the interaction between Fe and Cr atoms, have been fitted to reproduce the lattice parameter, the bulk modulus and the mixing enthalpy of the alloy, at Cr concentrations of 5 and 20%. The mixing enthalpy for the ferro-magnetic state was fitted to data calculated with Ab Initio methods in collaboration with Uppsala University. These data show that the formation energy is negative for Cr concentrations below 6%, a fact that was not known in previous attempts to obtain EAM potentials for the alloy.

7.3 RESULTS

A detailed account of our results has been published in 2 papers P. Olsson, I.A. Abrikosov, L. Vitos, J. Wallenius, 'Ab initio formation energies of Fe–Cr alloys, ' Journal of Nuclear Materials, 321 (2003) and J. Wallenius, C. Lagerstedt et al, "Development of an EAM potential for simulation of radiation damage in Fe-Cr alloys", 11th International Conference on Fusion Reactor Materials: ICFRM-11, Kyoto, 7 12 December 2003 which are attached in Appendices 5 and 6

One may note that our set of potentials yield better values for vacancy activation energies than any other published potential. The relative stability of interstitials in iron is also in good agreement with measurements, while the absolute formation energy appears to be somewhat high. Using our alloy potentials in kinetic Monte Carlo (KMC) simulation of vacancy driven thermal ageing it was found that the potential fitted to the negative mixing enthalpy of Fe-5Cr predicted no precipitation of Cr at any temperature. The potential fitted to the positive mixing enthalpy of Fe-20Cr did however yield formation of Cr clusters, as seen in Figure 7.1. Cr-rich clusters are indeed observed in real alloys only for Cr concentrations above nine percent, being denoted as the alpha-prime phase. The calculated time and temperature dependence of the precipitation rate was found to be in good agreement with data for hardening of Fe-Cr alloys.

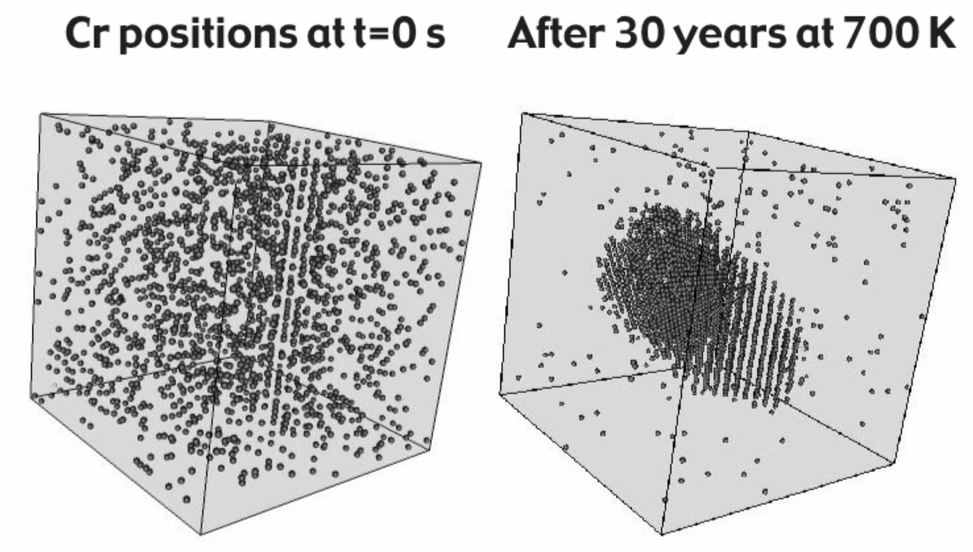

Figure 7.1 Simulated precipitation of Cr in Fe-20Cr.

The calculated sizes of the precipitates do however not agree with the measured size distribution (2-4 nm). This is due to the fact that the properties of Fe-20Cr no longer are relevant for describing a cluster containing 85% Cr, which is the measured Cr content in the alpha-prime phase. We will need to introduce a many-body potential into the EAM that is dependent on the local Cr concentration in order to predict a correct cluster size distribution. We are also preparing to construct potentials for Fe-C and Cr-C, with the purpose of simulating formation of metal-carbide precipitates, which are known to govern the mechanical properties of real steels.

8 REACTOR BASED TRANSMUTATION – NEUTRONIC STUDIES THE BURNUP CAPABILITIES OF THE DEEP BURN MODULAR HELIUM REACTOR

8.1 NEUTRON FLUX, SPECTRUM, CAPTURE TO FISSION RATIO AND TEMPERATURE COEFFICIENTS OF THE DEEP BURN MODULAR HELIUM REACTOR FED BY LWR's WASTE

Some important neutronic features of the Deep Burn Modular Helium Reactor (DB-MHR) have been studied using the MCNP/MCB codes. Our attention was focused on the neutron flux and its spectrum, capture to fission ratio of ^{239}Pu and the temperature coefficient of fuel and moderator. The DB-MHR is a graphite-moderated helium-cooled reactor proposed by General Atomic to address the need for a fast and efficient incineration of plutonium for non-proliferation purposes as well as the management of Light Water Reactors (LWRs) waste. In fact, recent studies have shown that the use of the DB-MHR coupled to ordinary LWRs would keep constant the world inventory of plutonium for a reactor fleet producing 400 TWe/y. In the present studies, the DB-MHR is loaded with Np-Pu Driver Fuel (DF) with an isotopic composition corresponding to LWRs spent fuel waste. DF uses fissile isotopes (e.g. ^{239}Pu and ^{241}Pu), previously generated in the LWRs, and maintains criticality conditions in the DB-MHR. After an irradiation of three years, the spent Driver Fuel is reprocessed and its remaining actinides are manufactured into fresh Transmutation Fuel (TF). Transmutation Fuel mainly contains non-fissile actinides which undergo neutron capture and transmutation during the subsequent three-year irradiation in the DB-MHR. At the same time, TF provides control and negative reactivity feedback to the reactor. After extraction of the spent Transmutation Fuel, irradiated for three years, over 94% of ^{239}Pu and 53% of all actinides coming from LWRs waste will have been destroyed in the DB-MHR. In this paper we look at the operation conditions at equilibrium for the DB-MHR and evaluate fluxes and reactivity responses using state of the art 3-D Monte Carlo simulations.

8.1.1 Introduction

The DB-MHR has been conceived by General Atomic (GA) as a new generation of nuclear power plants, graphite-moderated and helium-cooled, being able to face two major current problems of nuclear energy: proliferation and LWRs waste handling. In fact, the DB-MHR concept has a unique flexibility concerning nuclear fuels that can be loaded into the core: it can run as well on military plutonium as on LWRs waste. In a scenario where the use of DB-MHRs would be coupled with further use of LWRs, the world plutonium inventory would be kept constant in coming decades for a nuclear reactor fleet producing 400 TW_e/y [62].

The current design of the DB-MHR consists of four modules, each of them with a thermal power of 600 MW_{th}. The reactor operates using two different types of fuel: Driver Fuel (DF) and Transmutation Fuel (TF). The fresh DF contains $NpPuO_{1.7}$ coming from LWRs spent fuel, which is the fission products and uranium extraction from LWRs waste; whereas the fresh TF is made from spent DF (after it has been irradiated for three years in the DB-MHR) plus some set-aside Am-Cm (in the form $AmCmO_{1.7}$) coming directly from the reprocessing of the LWRs spent fuel. The DF depletes fissile isotopes and supplies the fission neutrons, mainly through fission of ^{239}Pu and ^{241}Pu. Whereas, the TF depletes non-fissile isotopes by neutron capture followed by natural decay or fission and it provides excess reactivity control. Because fissions in the DF are the main driver of the DB-MHR operations, and captures in the TF are control mechanism, the capture to fission ratio should be as low as possible for DF, and absorption in the TF should be facilitated as much as possible. After irradiation of three years transmutation of over 94% of ^{239}Pu and 53% of all actinides coming from LWRs waste [63] is achieved. The spent Transmutation Fuel constitutes the final waste of the DB-MHR. The high burnup capability of high temperature reactors has been also confirmed in pebble bed reactors [64]; in addition, chemical analysis studies have shown good agreement with the predictions of numerical simulations [65].

A part from the deep burn of nuclear waste, the DB-MHR exhibits several benefits: a cost lower than an ordinary LWR [66], a clear passive safety mechanism [67] - [74], a flexibility in the choice of fuel type, a high conversion energy efficiency, a well developed technology and an improvement of the barriers protecting the environment from the radiotoxicity of spent fuel. The DB-MHR fuel pins consist of a graphite matrix filled by a square lattice of triple isotropic coated particles (TRISO) [75] - [89], which are also an effective waste form with a reliable protective barrier. Each TRISO particle is made of a fuel kernel, a sphere with a radius of 150 μm for DF and 100 μm for TF, surrounded by a cladding of 4 layers: porous carbon, inner pyrolitic carbon, silicon carbide and outer pyrolitic carbon. The ratio between the width of the cladding and the radius of the kernel is 1.7 for DF and 2.6 for TF; by contrast, in ordinary LWRs the ratio between the width of zircaloy cladding and the radius of fuel pellets is only 0.14. Because of the large thickness of the cladding, TRISO particles can retain all fission products up to a temperature of 1600 ^{o}C. This limit can be higher, up to 1800 ^{o}C, if ZrC replaces SiC [90] - [93]. If the cooling of helium ceases, the passive heat removal grants that the temperature of the fuel never exceeds 1600 ^{o}C; in addition, the peak of power occurs after 72 hours, a period long enough to allow the plant operators to activate all safety devices. Nevertheless, a temperature excursion may trigger the oxidation of the graphite matrix of the fuel pins, because at 1000 ^{o}C its oxidation rate, as function of the surface temperature, increases to the asymptotic level, see [70].

The inner pyrocarbon layer usually is the first layer of a TRISO particle that fails, since it is subjected to counteracting mechanical stresses: a swelling, due to the pressure of fission products gases, and a shrinkage, due to the neutron irradiation. Therefore, the most usual failure is a radial crack on the internal side of the inner pyrocarbon layer (fig. 3 of [79]), where the strains are stronger (fig 5 of [78]). The strain of the mechanical stresses depends on: the fluence, the pyrocarbon density, the degree of anisotropy (the Bacon anisotropy factor) and the irradiation temperature. Recent studies have proven that the optimal width of the inner pyrocarbon layer of TRISO particles is about 15 μm, because, after this threshold, a greater thickness increases the probability of failure of the coating (fig. 11 of [78]). By contrast, a greater thickness of the porous carbon and SiC layers always reduces the probability of failure of the coating (fig. 10 and 12 of [78]).

Finally, the use of TRISO particles are useful also to reduce proliferation because it would be necessary to process 10^{10} coated particles to reach the critical mass of ^{239}Pu [64].

8.1.2 The DB-MHR - description and operation at the equilibrium of the fuel composition

The DB-MHR has been modeled in the numerical simulations as a cylinder, of 4 m radius and 10 m height, filled by a 13X13 matrix of fuel and graphite hexagonal blocks. The fuel blocks consist of 3 concentric rings of 36 hexagons as shown in *Figure 8.1*. Each fuel block has a side of 20.8 cm and a height of 7.93 m; a graphite reflector covers further 1.035 m, both at top and at bottom, along the axial direction (fig. 6 of [63]). In each hexagonal block there are 108 cooling channels, with a diameter of 0.797 cm, 144 DF pins and 72 TF pins, both with a diameter of 0.622 cm (fig. 5 of [63]The coolant channel surrounding the fuel pin has an external radius of 0.635 cm. Each fuel pin consists of graphite filled with a square lattice of TRISO particles, which are fuel oxide spheres (kernel) covered by a triple isotropic coated layer. The structure and properties of a TRISO particle are shown in Table 2 and fig. 5 of [63]. In order to decrease the capture to fission ratio of DF, and therefore of ^{239}Pu, see Figure 8.2, General Atomic selected a higher radius for the DF kernel comparing to TF. For simplicity design, we kept for both fuels the same packing ratio (defined as the volume of fuel kernels over the total volume of fuel pin) [63].

It takes about 12 years for DB-MHR to approach an equilibrium composition; therefore, all our studies have been focused on the 12th year. The in-core loading strategy is grounded on the following steps:

- At the beginning of the 1st year, we assumed that the reactor starts its life by loading the fresh DF into the inner ring.
- At the beginning of the 2nd year, the spent DF is shuffled into the central ring and fresh DF takes its place.
- After two years, at the beginning of the 3rd year, spent DF from the central ring is moved into the outer ring; the spent DF from the inner ring is shuffled in the central one; the inner ring is filled with fresh DF. No TF fuels the reactor during the first three years.

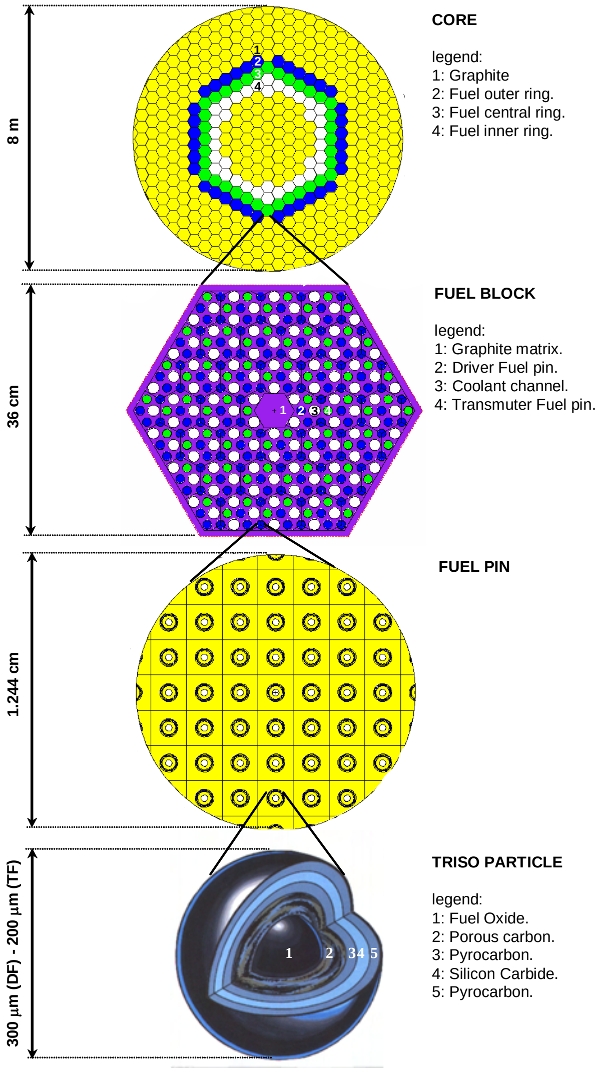

Figure 8.1 The model of the DB-MHR used in simulations.

- At the end of the 3rd year, the spent DF from the outer ring, which it has been irradiated a period of three years, is reprocessed, by fission products extraction, to build the fresh TF, which contains also some set-aside Am-Cm from the reprocessing of LWR spent fuel.

- At the beginning of the 4th year the inner ring contains both fresh DF and TF. In the following years, the shuffling policy is continued as in the first three years: moving both spent DF and TF outwardly at the end of each year.

- The reactor loads DF and TF in all three rings just at the beginning of the 6th year. After an irradiation of 3 years, the TF is extracted from the outer ring as waste.

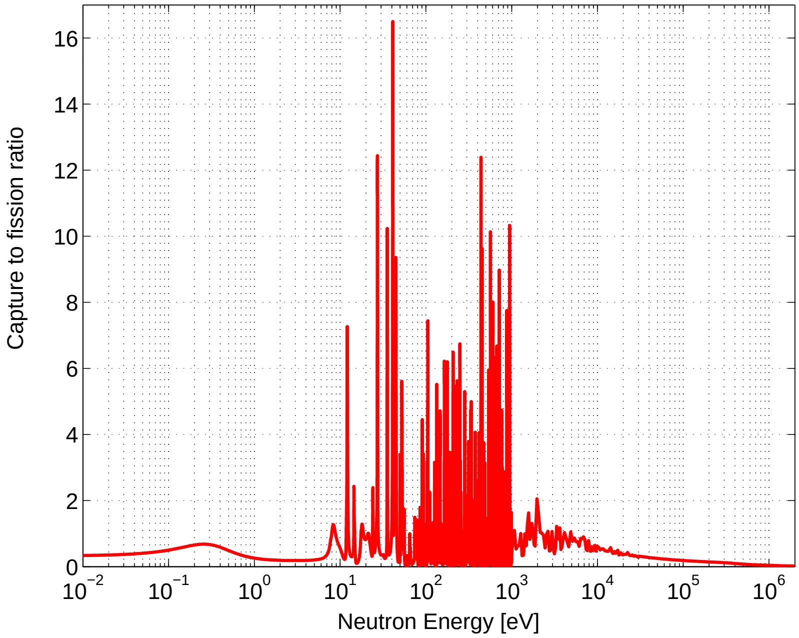

Figure 8.2 Capture to fission ratio of ^{239}*Pu.*

In the approach to equilibrium, we simulated for a time being only the radial shuffling and we neglected the axial one. In the real project of General Atomic, each hexagonal fuel block consists of 10 axial sub-blocks, which every year should shuffle from [0 1 2 3 4 5 6 7 8 9] to [4 3 2 1 0 9 8 7 6 5]. This axial shuffling optimization will be addressed in our next work.

Our model of the DB-MHR lacks, at the moment, the representation of the control rods, but this approximation should not seriously affect burnup calculations since the value of k_{eff} is very close to criticality (fig. 8 of [63]).

We performed all time dependent simulations by the code MCB [4]-[7] , an extension of MCNP [3] with the burnup implementation; whereas, we used the MCNP code for the static calculations. Both numerical codes have been equipped with a cross section library based on JEF-2.2 complemented with ENDF\B-6.8 and JENDL-3.2.

8.1.3 Neutron Flux and spectrum at the equilibrium of the fuel composition

We investigated both the radial and the axial profile of the neutron flux in the DB-MHR core and in the fuel pins. We performed the calculations at the beginning of the 12th year and after 330 days of full power operation. In order to evaluate the radial flux profile in the core, we selected 11 hexagonal blocks (the 12th block is cut by the edge of the reactor) disposed along the radial direction from the center of the reactor (which corresponds to the vertical direction of fig. 5 of [63]). At the same time, we divided each hexagonal block into 10 axial sub-blocks equally spaced along the z axis in order to estimate the axial flux at different heights. It is important to highlight that the axial division into 10 sub-blocks reflects the real reactor, since the graphite blocks are manufactured with this structure. Nevertheless, since the flux is symmetric along the z axis, we limited our studies only to the upper 5 axial sub-blocks. In this set of simulations we did not consider the flux in the two axial reflectors.

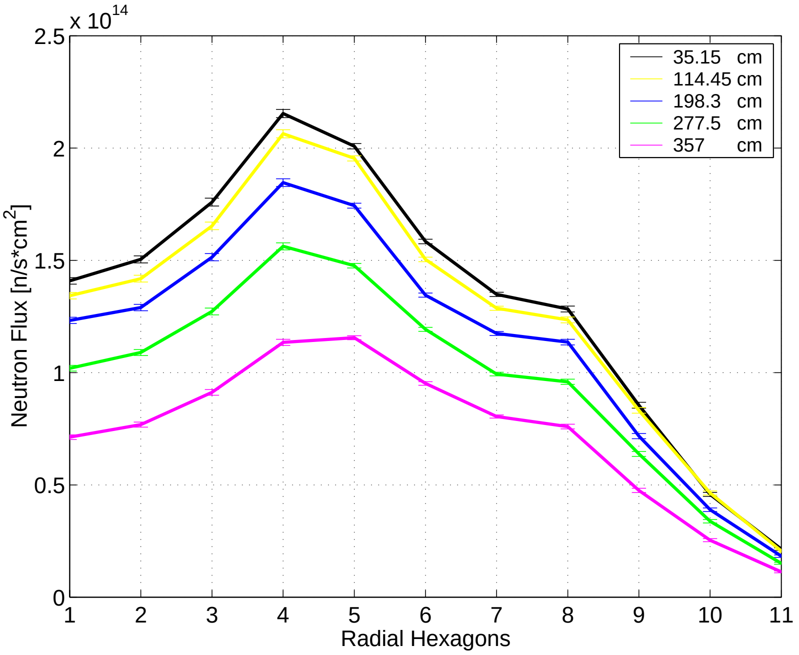

Figure 8.3 Neutron flux profile at the beginning of the 12th year. Neutron flux has been averaged in 10 axial sub-blocks and 11 radial hexagonal blocks from the center of the reactor. Curves refer to the upper 5 axial sub-blocks. The 5th radial hexagonal block corresponds to the inner ring, the 6th to the central one and 7th to the outer one. Ticks on the curves represent the standard deviation

Figure 8.3 shows the radial profile of flux in the reactor sampled in the radial hexagonal blocks, each curve represents one of the 5 upper axial sub-blocks at the beginning of the 12th year. The neutron flux drops after the 8th block due to the increase of leakage in the outer blocks; the same effect plays a visible role in the last two axial sub-blocks, where, in addition, the flux becomes more flattened because neutrons with a higher energy escape the more. Nevertheless, leakage plays a little role in the economy of the reactor since only 3.2% of neutrons escape. We can observe in Figure 8.3 that the peak of the neutron flux emeges in the 4th block, which consists of pure graphite and it is adjacent to the fuel block of the inner ring. This behavior is explained by the graphite moderation of neutrons coming from the inner fuel ring, which contains fresh fuel, and the circular shape of fuel, which does not allow radial leakage. Moreover, fuel blocks disposed in an anular shape flatten the flux in the center of the reactor.

In order to understand better the radial and axial flux behavior, we performed studies of the flux distribution inside of the DF and TF pins located at the center of a hexagonal block for each of the three rings of fuel. We analyzed a total of 6 pins: a pair of pins for the inner, central and outer rings. The 6 fuel pins have been separately divided, both along the radial and the z axes, into 10 equivolume regions. Figure 8.4 shows the radial flux profile in the DF and TF pins located at the center of a hexagonal block for the inner, central and outer rings at the beginning of the 12th year. We can note that the flux in the inner ring is much higher because it contains fresh fuel. It is not surprising that the neutron flux is quite flat, because of the small radius of fuel pin (0.622 cm) compared to the whole reactor (4 m). Figure 8.5 shows the axial flux profile for the same pins of Figure 8.4; we can see that the flux drops about 50% along the height of the pins. By contrast, as Figure 8.3 shows, the radial drop of the flux is significantly lower (about 25%). Therefore the axial shuffling of the fuel plays an important role for the optimization of the ^{239}Pu burnup.

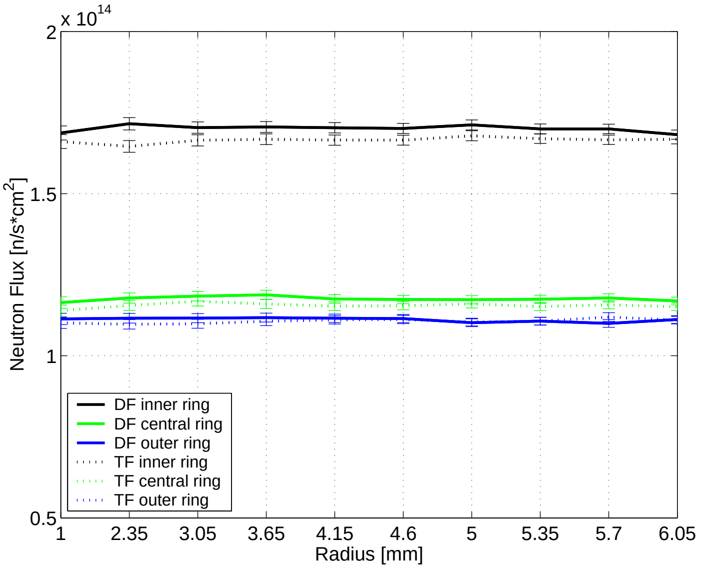

Figure 8.4 Radial neutron flux at the beginning of the 12th year of DF and TF pins in the center of a hexagonal block in the inner, central and outer rings.

Figure 8.6 shows the same flux of Figure 8.3 but referred to the end of the 12th year; we can note that the flux is a little higher (about 6%) than that one at the beginning of the year since the reactor operates at constant power and fuel depletes. Nevertheless, even if flux is a little higher, the values of flux in the 11th block, which is located close to the boundary of the reactor, remain unchanged at the end of the 12th year, since a higher flux increases neutron leakage. Let us note that the difference between the flux at the beginning of the year and that one at the end is not bound to the statistical error, since the relative standard deviation of flux is only 0.8%. In addition, the two curves at top of Figure 8.6 are closer than those ones in Figure 8.3, because the top curve of Figure 8.3 experienced a higher burnup. Analogue considerations, about the difference between the flux at the beginning of the 12th year and that one at the end, may apply to Figure 8.7

and Figure 8.8 versus Figure 8.4 and Figure 8.5, respectively. Figure 8.4 and Figure 8.5 show that the flux in the DF is higher than in TF since DF contains an higher quantity of fissile actinides; nevertheless this effect if negligible at the end of the 12th year because of the burnup. Let us also remark that the choice of the cross sections library between JEF, JENDL and ENDF/B may affect up to 6.5% the value obtained for neutron flux (table 5 of [95]).

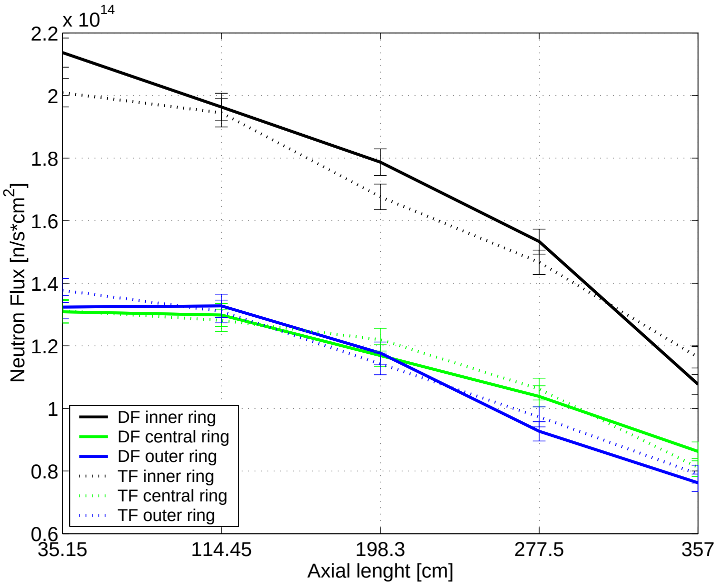

Figure 8.5 Axial neutron flux at the beginning of the 12th year of DF and TF pins in the center of a hexagonal block in the inner, central and outer rings.

We calculated the neutron spectrum averaged over the whole reactor, including the two axial reflectors, and in the DF and TF kernels for each of the three rings of fuel blocks. All neutron spectra have been calculated using the energy binning corresponding to the 69 energetic groups of the WIMS cross section library for thermal reactors; these groups are composed of 14 fast groups, 12 resonance groups, and 42 thermal groups [96] and [97]. Figure 8.9 , which shows the neutron spectrum at the beginning of the 12th year, clearly indicates the reactor operates in a thermal spectrum with a spectral peak located at the energy of 0.11 eV, which is a little less than the value of 0.2 eV calculated by Nakata in [98].

The DB-MHR, as other power reactor types, requires a proper reactivity management in order to compensate for burnup of fissile isotopes without violating safety limits for reactivity excess available during operation. The ^{167}Er isotope can serve this purpose as a burnable poison enhancing simultaneously the Doppler temperature feedback. However, it is also possible to take advantage of the unique features of the TF, which contains isotopes having both a breeding potential which sustains reasonable reactivity margins and favorable neutron capture cross sections contributing to the desired temperature feedbacks. Particularly, TF neutron capture cross section is favorable in the energy region just behind the thermal peak of the spectrum (Fig. 2 in [63]).

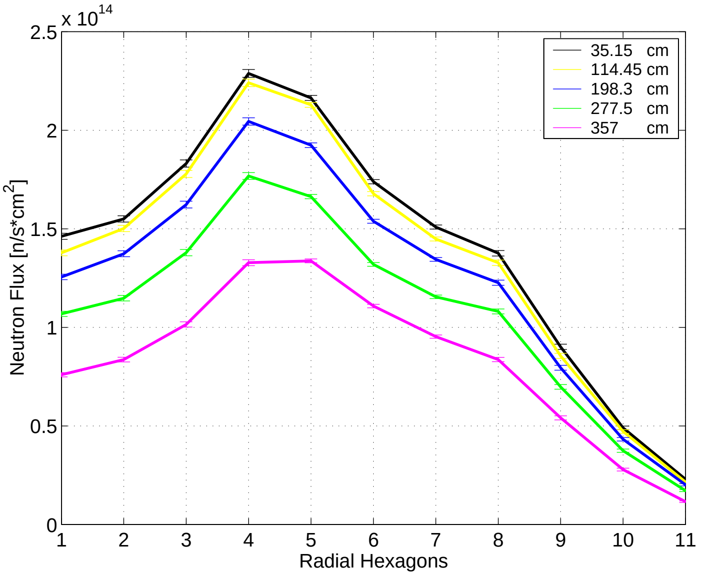

Figure 8.6 Neutron flux profile at the end of the 12th year. Neutron flux has been averaged in 10 axial sub-blocks and 11 radial hexagonal blocks from the center of the reactor. Curves refer to the upper 5 axial sub-blocks. The 5th radial hexagonal block corresponds to the inner ring, the 6th to the central one and 7th to the outer one. Ticks on the curves represent the standard deviation

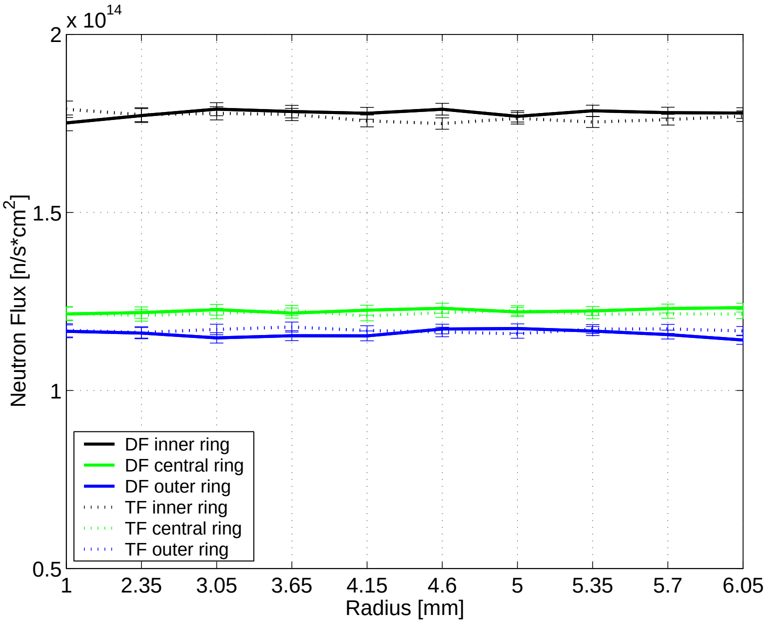

Figure 8.7 Radial neutron flux at the end of the 1^{2th} year of DF and TF pins in the center of a hexagonal block in the inner, central and outer rings

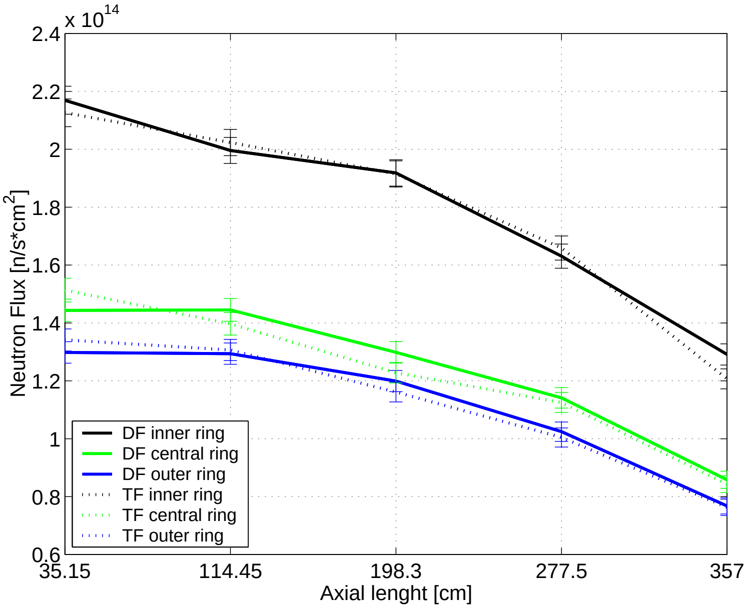

Figure 8.8 Axial neutron flux at the end of the 12^th^ year of DF and TF pins in the center of a hexagonal block in the inner, central and outer rings

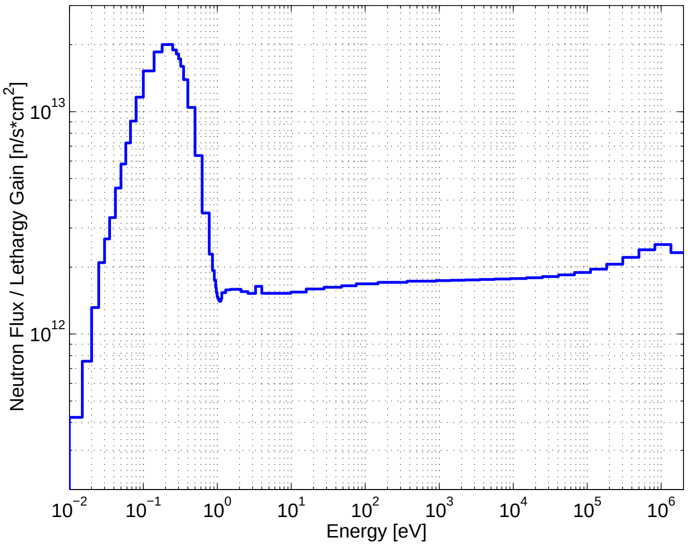

Figure 8.9 Neutron spectrum at the beginning of the 12^th^ year averaged in the whole reactor.

The neutron spectra of DF and TF kernels, as showed on Figure 8.10 - Figure 8.15, exhibit a pattern, reminding a fast spectrum. In fact, kernels as a bulk *see* mostly fast fission neutrons leaving; whereas, all thermalised neutrons entering back are immediately absorbed. We can note some fine differences on those neutron spectra. The central ring has hardest spectrum among the three fuel rings, since is not moderated by any adjacent block of graphite. Moreover, the inner ring has a harder spectrum than the outer one, because it is loaded with fresh fuel. In fact, ^{239}Pu, abundant in the fresh fuel, depresses significantly the low energy part of the spectrum on Figure 8.11 in the energy range 0.1-0.3 eV due to its high capture to fission ratio. The distinct dip in Figure 8.10, located at 1 eV, is due to resonance capture of ^{240}Pu. During full power operation, the relative abundance of ^{239}Pu, both in DF and TF, decreases but abundance of ^{240}Pu increases. Consequently, the dip corresponding to ^{239}Pu resonance becomes more shallow while passing from the inner ring (Figure 8.10), the central one (Figure 8.11) to the outer one (Figure 8.12). By contrast, resonance capture of ^{240}Pu responsible for the second dip has a somewhat opposite behavior due to the increased amount of ^{240}Pu in irradiated fuel: the dip corresponding to ^{240}Pu becomes deeper while passing from the inner ring (Figure 8.10), the central one (Figure 8.11) to the outer one (Figure 8.12). The same phenomena can be observed by analyzing the spectra at the beginning of the 12th year and after 330 days of full power operation. In fact, the dip of ^{239}Pu decreases and that one of ^{240}Pu increases while comparing Figure 8.12 with Figure 8.10, Figure 8.14 with Figure 8.11 and Figure 8.15 with Figure 8.12. It is worth to note that at the end of the 12th year the ^{239}Pu dip in TF (Figure 8.15) has almost disappeared because of ^{239}Pu depletion.

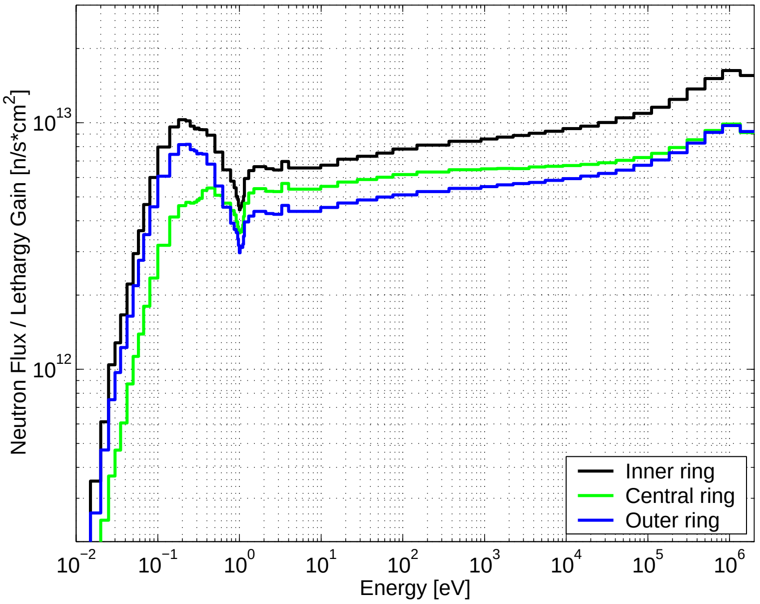

Figure 8.10 Neutron spectrum at the beginning of the 12th year averaged in one hexagonal block

The spectrum averaged in the whole reactor at the end of the 12th year had as expected no significant differences with the corresponding one at the beginning of the year; in fact, the moderation of graphite attenuates the differences of the spectra in the kernels.

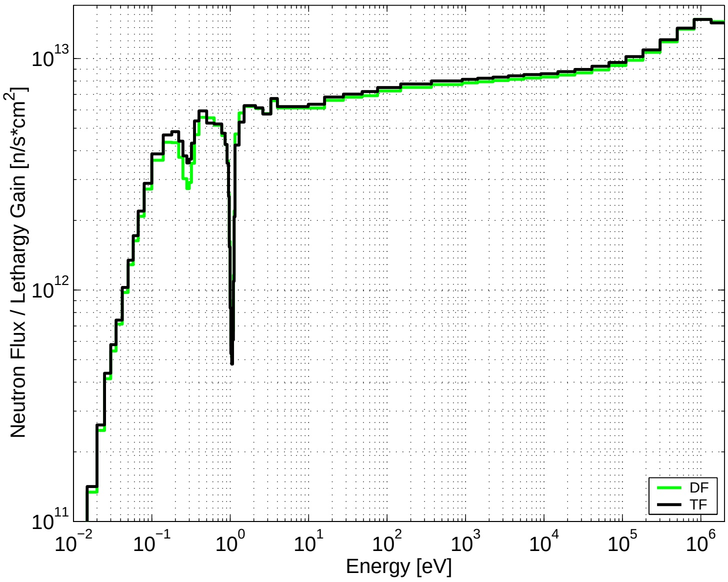

Figure 8.11 Neutron spectrum at the beginning of the 12th year in the kernel of the fuel pin located at the center of a hexagonal block of the inner ring.

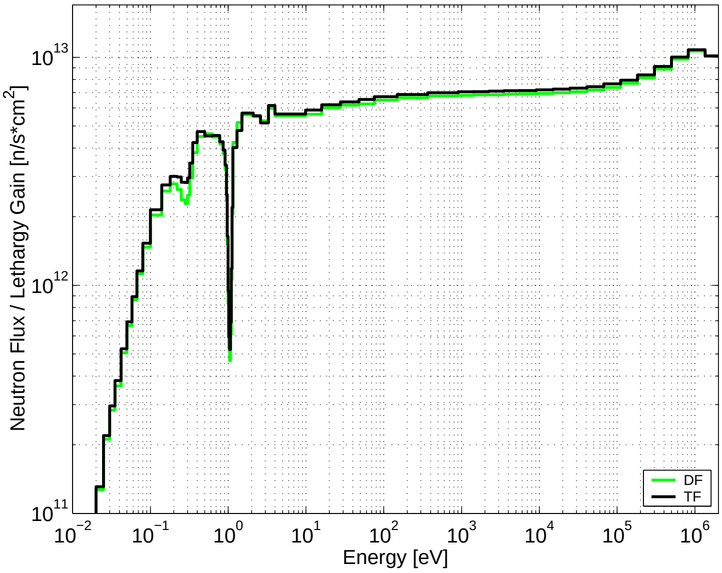

Figure 8.12 Neutron spectrum at the beginning of the 12th year in the kernel of the fuel pin located at the center of a hexagonal block of the central ring.

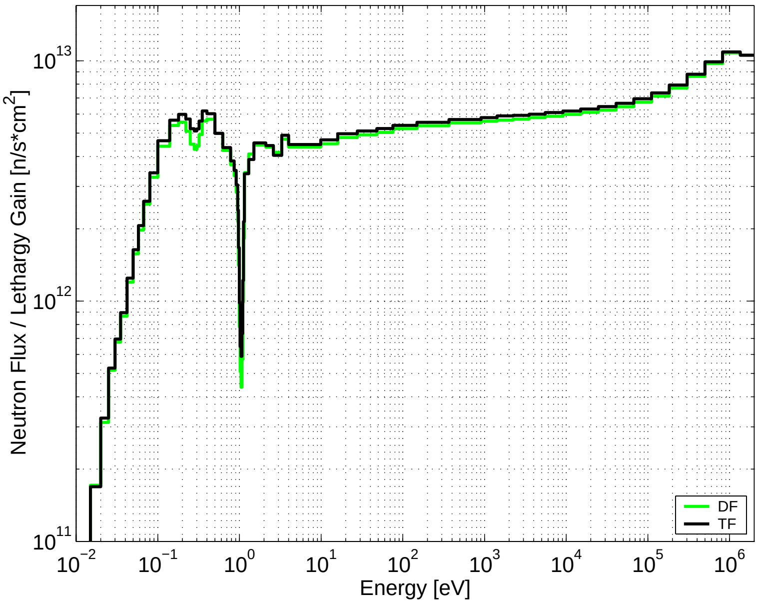

Figure 8.13 Neutron spectrum at the beginning of the 12th year in the kernel of the fuel pin located at the center of a hexagonal block of the outer ring.

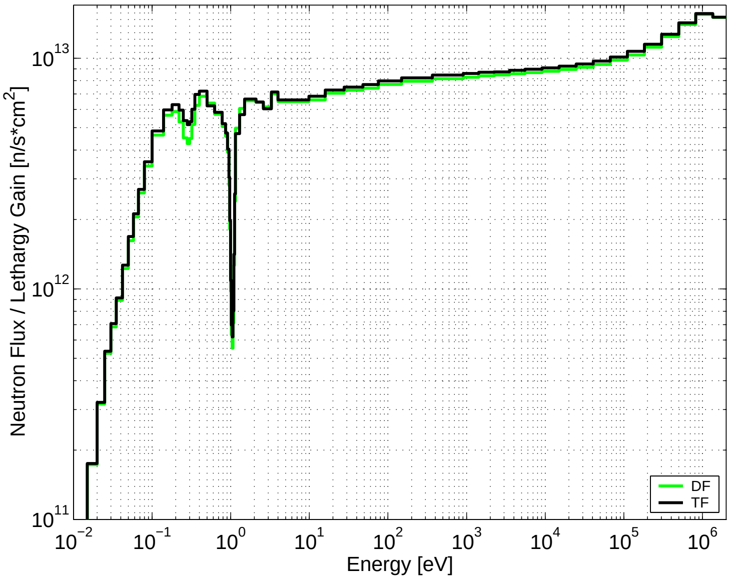

Figure 8.14 Neutron spectrum at the end of the 12th year in the kernel of the fuel pin located at the center of a hexagonal block of the inner ring.

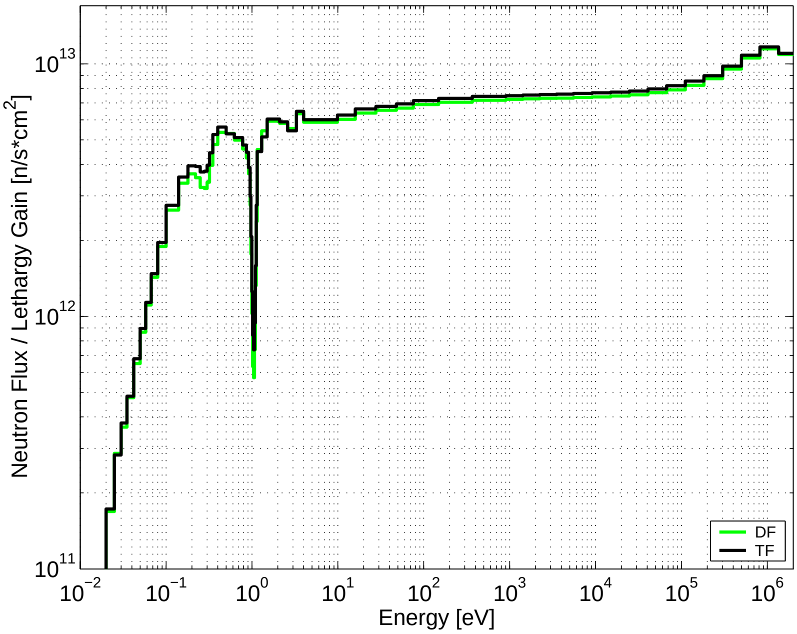

Figure 8.15 Neutron spectrum at the end of the 12th year in the kernel of the fuel pin located at the center of a hexagonal block of the central ring.

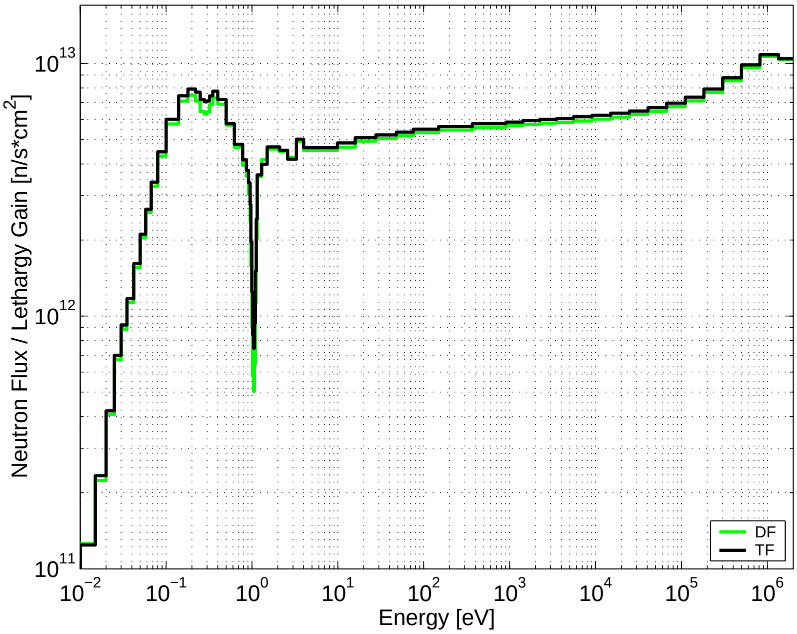

Figure 8.16 Neutron spectrum at the end of the 12th year in the kernel of the fuel pin located at the center of a hexagonal block of the outer ring.

8.1.4 Effect of DF kernel volume to the capture to fission ratio

In order to optimize the rector performance, one would like to obtain the capture to fission ratio of fuel as low as possible for DF, since DF should be efficiently fissioned, whereas TF is dominated by neutron capture. Consequently, General Atomic set the radius of the DF kernel of TRISO particles (150 μm) greater than that one of TF (100 μm). We tried to verify the benefits of this choice by studying the capture to fission ratio of ^{239}Pu, because this isotope is the most abundant one in DF and any change on its reaction rate strongly affects the behavior of the reactor. In order to analyze the effects of the kernel size in the capture to fission ratio of ^{239}Pu, we gradually changed, the radius of the DF kernel keeping constant its packing ratio. We used the set of values: 100, 150, 200, 250 μm as radii of the DF kernel; whereas, we kept constant the radius and packing ratio of the TF kernel at their nominal values [63]. All calculations were performed for the beginning of the 12th year.

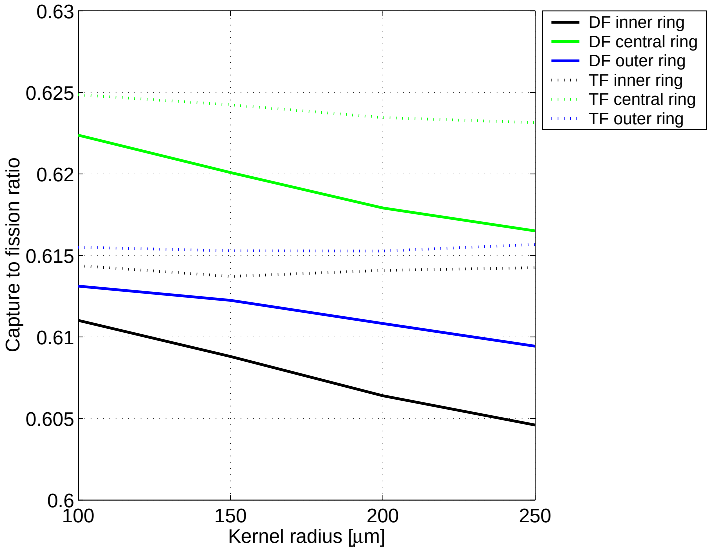

Figure 8.17 Capture to fission ratio of ^{239}Pu at the beginning of the 12th year for different radii of the DF kernel. The TF radius has been kept constant to 100 μm.

A greater radius of the kernel of TRISO particles induces a better thermalization of neutrons in the fuel volume and therefore a decrease in the capture to fission ratio, as Figure 8.17 shows. In fact, the neutron spectrum in the fuel is fast and the major contribution to the capture to fission ratio comes from the resonances of the fast region (Figure 8.2); therefore, better termalizatuion of the spectrum results in a lower capture to fission ratio. In addition, the spatial self-shielding is negligible because the mean free path of neutrons in the DF kernel is about 1.8 cm, 600 times higher than the kernel diameter. Since the inner ring contains a larger quantity of ^{239}Pu, with the low capture to fission value in the slope between 0.1 and 0.3 eV (Figure 8.2), it has a lower capture to fission ratio than the outer one (Figure 8.13 and Figure 8.16). Whereas, the central ring with the hardest spectrum of all the three rings, has the highest values of the capture to fission ratio (Figure 8.17) around the the resonace peaks and consequently the higher average capture to fission ratio. TF – as can be seen on Figure 8.17– shows negligible changes, since the TF radius has been kept constant.

It can be concluded that there is no significant impact of the kernel size variation, so one can have DF and TF kernels of the same size, a choice that simplifies manufacturing of fuel.

Since ^{239}Pu is the most abundant isotope of DF, mostly responsible for sustaining the fission chain, a lower capture to fission ratio of ^{239}Pu leads to a higher k_{eff} (Figure 8.17 and Figure 8.18) and the variation of k_{eff}, with different radii of DF kernel, have the same magnitude as the changes in the capture to fission ratio of ^{239}Pu (about 1%).

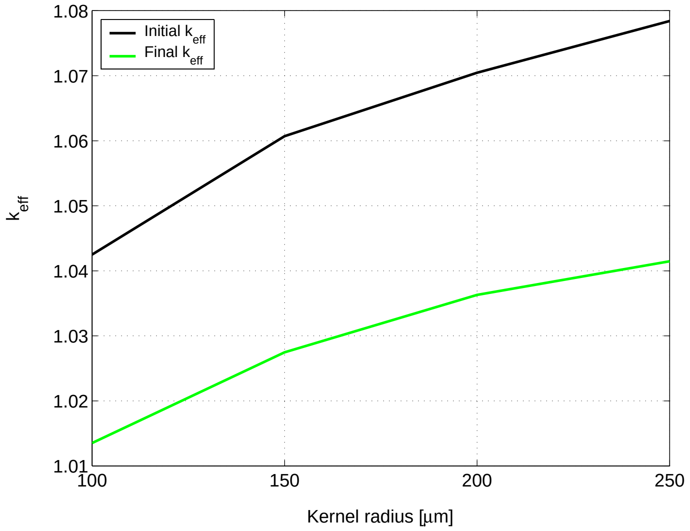

Figure 8.18 k_{eff} for different radii of the DF kernel during the 12th year. Maximal standard deviation lower than 0.00041.

8.1.5 Reactivity temperature coefficients.

8.1.5.1 Cross section changes

We calculated the temperature coefficient (CT) for a temperature excursion affecting only the cross sections of either the fuel or the moderator. Again, we focused our studies at the beginning of the 12th year.

Since the operational temperature of the DB-MHR fuel is about 1400 K and the coolant temperature is in the range of 760 -1100 K, we assumed the reference temperatures of 1500 K for fuel and of 1200 K for graphite. Then, we varied separately the temperature of the fuel and the moderator from 1200K, through 1500K up to 1800 K. With this set of temperatures, we estimated the reactivity changes corresponding to the temperature variation, by the formula:

$$\Delta\rho=\rho(T)-\rho_{reference}$$

where ρ(T) is the reactivity of the reactor for different fuel or moderator temperatures. Whereas, $\rho_{reference}$ is the reactivity of the reactor for which both fuel and moderator are at the reference temperatures. Then, we calculated the temperature coefficient (CT) by the formula:

$$CT=\frac{\Delta\rho}{\log\left(\frac{T}{T_{reference}}\right)}$$

Table 8.1 summarizes the results for the fuel temperature changes and Table 8.2 for the moderator. The DB-MHR exhibits negative reactivity temperature coefficients both for fuel and moderator cross section variations. The reactivity changes corresponding to the 300 K temperature raise or drop are of the level of 420 pcm for the fuel and 4000 – 9000 pcm for the moderator. Consequently, the temperature coefficients for moderator are 10 times larger than those for the fuel. This huge difference may be explained by Figure 8.19, because it shows that the peak of neutron spectrum, for a fuel temperature of 1800 K and a moderator one of 1500 K, shifts from 0.11 eV (at the reference temperatures) to 0.2 eV, exactly where ^{239}Pu exhibits a peak in the capture to fission ratio. Therefore, the shift of the spectrum generates a very strong feedback and it affects mainly the moderator CT; in fact, the moderator CT is mainly driven by the spectrum shift, whereas that one of fuel does by the broadening of capture resonances.

Table 8.1: k_{eff}, reactivity (ρ), differential reactivity (Δρ) and temperature coefficient (CT) for different temperatures of the cross sections of the fuel at the beginning of the 12th year. Maximal standard deviation of k_{eff} lower than 0.00023.

Fuel Temperature [K]	1200	1500	1800
k_{eff}	1.06511	1.06040	1.05550
ρ	0.06113	0.05696	0.05258
Δρ	0.00417	0	-0.00438
CT	-0.01869	0	-0.02401

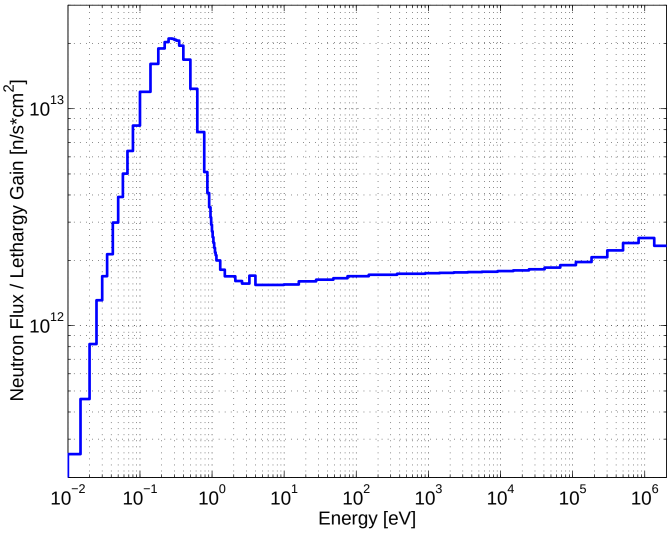

Figure 8.19 Neutron spectrum at the beginning of the 12th year averaged in the whole reactor for fuel at 1800 K and graphite at 1500 K (with S(α,β) at 1600 K).

Table 8.2*:* k_{eff} , reactivity (ρ), differential reactivity (Δρ) and coefficient of temperature (CT) for different temperatures of the cross sections of the moderator at the beginning of the 12th year. Maximal standard deviation of k_{eff} lower than 0.00022.

Moderator Temperature [K]	1200	1500	1800
k_{eff}	1.06040	1.01883	0.96468
ρ	0.05696	0.01848	-0.03661
Δρ	0	-0.03848	-0.09357
CT	0	-0.17243	-0.23078

We performed also a set of simulations using different temperatures of the moderator to test the sensitivity of MCNP results on the S(α,β) thermal neutron treatment data, necessary for a proper simulation of the thermal neutron interactions with graphite (upscattering processes). Table 8.3 shows a dependence of k_{eff} on temperature dependent S(α,β) matrices for the moderator. Table 8.3 indicates that temperature dependent thermal neutron scattering in graphite is responsible for almost the entire cross-section dependent reactivity feedback from the moderator. Moreover, it should be noted the the S(α,β) dependent reactivity feedback in the temperature interval 1200 - 1600 K is four time bigger than in the interval 800-1200 K. This behavior can be explained by the neutron spectral shift towards a large resonance capture in ^{239}Pu.

Table 8.3 **:** k_{eff} at different temperatures of the moderator using a different thermal treatment.

	S(α,β) 800 K	**S(α,β) 1200 K**	**S(α,β) 1600 K**
900 K	1.07090	1.06027	1.01895
1200 K	1.07083	1.06040	1.01890
1500 K	1.07095	1.06000	1.01883
1800 K	1.06847	1.05788	1.01671

In addition, we tested the sensitivity of k_{eff} on a temperature dependent free gas neutron treatment (TMP parameter on the cell cards). As expected no significant impact has been found; in fact, the free gas treatment can be accounted as highest to only 0.07% of k_{eff}, a value lslightly higher than the standard deviation (0.02%).

8.1.5.2 Density and volume changes

Temperature dependent changes of density driven by the thermal volume expansion contribute also to the thermal reactivity feedback, CT. We simulated two different scenarios: increase of the fuel temperature (up to 1800 K) with a constant moderator temperature at the reference value of 1200 K; whereas, in the second scenario we increased also the temperature of moderator to the value of 1500 K.

In order to take into account the volume expansion of the fuel, the radius of the kernel of the TRISO particles at 1800 K (r_{1800}) has been increased according to the following formula [100]:

$$r_{1800}=r_{293}\cdot(a_0+a_1T+a_2T^2+a_3T^3) \qquad T=1800\text{ K}$$

The a_i are constants (given in Table 8.4) and r_{293} is the radius at the temperature of 293 K, which has been calculated by:

$$r_{293}= r_{reference}\cdot(a_0+a_1T+a_2T^2+a_3T^3)^{-1} \qquad T=1500\text{ K}$$

where $r_{reference}$ is the radius of the kernel during normal operation (150 μm for DF and 100 μm for TF at 1500 K). Then, we preserved the mass of fuel by decreasing its density according to the new volume.

Table 8.4**:** Fuel thermal expansion constants.

$\mathbf{a_0}$	0.99652
$\mathbf{a_1}$	$1.17876 \cdot 10^{-5}$
$\mathbf{a_2}$	$-2.42851 \cdot 10^{-9}$
$\mathbf{a_3}$	$1.21876 \cdot 10^{-12}$

In the second simulation we modified also the temperature of moderator, the H451 graphite. In the long run, the volume of graphite changes according to irradiation temperature and time exposure. Irradiated graphite may tend to swell or shrink depending on the operational temperature. Since during normal operation in the DB-MHR graphite works above 700 K, which is the turnaround temperature, the volume change results always in swelling [101]. However, in our model we neglected the irradiation effects on graphite volume, since we considered only the major fast contributes due to a temperature change: thermal expansion. We assumed the linear expansion coefficients of graphite(α_C) and silicon carbide (α_{SiC}) equal to $4.55 \cdot 10^{-6}$ [102] and $4 \cdot 10^{-6}$ K^{-1}, respectively. Consequently, the density d1500 of all graphite zones at temperature of 1500 K and that one of silicon carbide in the layer of the TRISO particles have been recalculated according to the following formula:

$$d_{1500}=d_{reference} \cdot (1+\alpha\Delta T)^{-3} \qquad \Delta T=300\ K$$

where α is the linear coefficient either of graphite or silicon carbide and $d_{reference}$ is the density during normal operation. In order to take into account the thermal expansion of graphite and silicon carbide, we increased all the geometric data regarding graphite and silicon carbide by the following equation:

$$x_{1500}=x_{reference} \cdot (1+\alpha\Delta T) \qquad \Delta T=300\ K$$

where x_{1500} and $x_{reference}$ respectively are the geometric data at the temperature of 1500 K and at 1200 K.

The temperature coefficients weakly depend on variation of the density and volume of materials comparing to the change of cross sections temperature. In fact, the value of CT reported in the first column of Table 8.5, which includes also the variation of density and volume, differs just 13% from the result calculated in the third column of Table 8.1, which includes only cross-sections variation. The columns of Table 8.5 show that the addition of the variation of volume and density keeps unchanged the large difference (about an order of magnitude) between the moderator CT and the fuel one.

Table 8.5: k_{eff}, reactivity (ρ), differential reactivity (Δρ) and temperature coefficient (TC) at the beginning of the 12th year for different temperatures of fuel and moderator. Maximal standard deviation of k_{eff} lower than 0.00024.

	1800 fuel – 1200 moderator	1800 K fuel -1500 K moderator
k_{eff}	1.05474	1.01387
ρ	0.05190	0.01368
Δρ	-0.00506	-0.04328
CT	-0.02776	-0.23738

Table 8.6, which shows the capture to fission ratio of ^{239}Pu at increased temperatures, demonstrates how strictly connected are the changes in the capture to fission ratio of ^{239}Pu with the changes in the k_{eff}. In fact, a change, due to an increase of temperature, in the capture to fission ratio of ^{239}Pu (Table 8.6), has the same order of magnitude than a change in the value of k_{eff} (Table 8.5). Namely, when the moderator temperature increases to 1500 K (second column of Table 8.6), the change in the capture to fission ratio (from the reference value) is 8 times the change generated by the increase of only fuel temperature (first column of Table 8.6). At the same way, when the moderator temperature increases to 1500 K (second column of Table 8.5) the change in k_{eff} (from the reference value, Table 8.1 and Table 8.2) is 8 times the change generated by the increase of only fuel temperature (first column of Table 8.5). Finally, by comparing the values reported in Table 8.6, we see how an increase of temperature, therefore a faster spectrum, increases the value of the capture to fission ratio, as Figure 8.2 would have foretold because of a larger contribute of the peak at 0.2 eV.

Table 8.6**:** Capture to fission ratio of ^{239}Pu at the beginning of the 12th for different temperatures of fuel and moderator.

	Fuel at 1800 K Moderator at 1200 K	Fuel at 1800 K Moderator at 1500 K
Inner ring DF	0.609	0.616
Central ring DF	0.621	0.625
Outer ring DF	0.612	0.620
Inner ring TF	0.615	0.621
Central ring TF	0.624	0.628
Outer ring TF	0.615	0.623

8.1.6 Conclusions

The disposition of fuel in a circular shape and the radial shuffling strategy set a quite flat profile of neutron flux along the radial direction (since it drops only of 25%). Nevertheless, the axial profile exhibits a larger change than the radial one (since it drops of 50%); therefore, the inclusion of the axial shuffling in the simulation model may better optimize the fuel cycle. The peak of neutron flux lies not in the inner ring of fuel blocks, which contains fresh fuel, but rather in the adjacent (toward the center of the reactor) graphite block. Leakage become significant only in the last three radial hexagonal blocks. Flux level mainly depends on the geometry location and very little on the fuel isotopic composition, since the pins of DF and TF in the same block have almost same the same flux. The level of flux maintains quite constant during the operation of the reactor, since at the end of the 12th year it increases only of 6%.

The peak of neutron spectrum lies at 0.11 eV, which clearly proves that the DB-MHR operates in the thermal region. By contrast, fuel experiences a fast spectrum with two dips in the thermal region due to resonance captures of ^{239}Pu and ^{240}Pu. The amplitude of the dips changes according to both the location of fuel pin (different rings experienced a different level of fluence due to the radial shuffling) and the irradiation time during operation.

No single benefit came from the choice of General Atomic to set a radius of the DF kernel greater than the TF one in order to jeopardize the number of fissions.

Both the fuel temperature coefficient and the moderator one are negative; in addition, the temperature coefficient of moderator is very large (about 4000-9000 pcm) and it is one order of magnitude higher than the value of the fuel. The temperature coefficients allow the GT-MHR to automatically shutdown in an accident scenario, because, when the temperature of fuel increases to 1800 K and that one of moderator to 1500 K, the peak of spectrum shifts to 0.2 eV triggering a strong negative feedback due to a peak in the capture to fission ratio of ^{239}Pu. In the numerical model, the temperature of graphite is mainly established by the $S(\alpha,\beta)$ card of MCNP; whereas the TMP entry of the cell cards does not affects results. The inclusion of volume thermal expansion in the calculation of the temperature coefficients brings only to second order changes, since the values differ only 13% from the case in which it has been taken into account only the temperature of cross sections.

The fuel cycle based on Pu is mostly driven by ^{239}Pu, since any change on the capture to fission ratio of this isotope proportionately reflects the change on the k_{eff} value.

10 DEVELOPMENT OF CALCULATIONAL TOOLS FOR ADS

10.1 VALIDATION OF MONTE CARLO BURNUP CODE – MCB - ON RINGHALS 4 EXPERIMENT

10.1.1 Introduction

The Monte Carlo Burnup Code (MCB), developed at KTH in collaboration with the UMM in Krakow is a geometry-dependent burnup simulation tool that can be used to determine the material composition in reactor fuel. Being an extension of Monte Carlo n-Particle (MCNP) code, it solves the Bateman equations for each particular material.

Validation of MCB is now one of the most important steps in development of the reliable ADS and reactor burnup simulation tools based on the Monte Carlo technique.

The experimental burnup data of the pressurized water reactor (PWR) Ringhals 4 have been obtained in collaboration with Vattenfall Bränsle. Since the burnup measurements were performed only after the 14th burnup cycle the amount of calculational work to complete this task is very challenging. In year 2003 some results from the first reactor cycle were obtained.

10.1.2 Objectives

The main objective of the work is to validate the code versus experimental chemical data[2]. Other purposes of the validation are comparison with known reactor physical phenomenae, fuel behaviour and reactivity control (reactor dynamics). Assuming the code is valid, one great advantage will be the possession of a complete inventory of the isotopic composition of the spent fuel from the Ringhals reactor with a very good accuracy.

10.1.3 The Ringhals 4 reactor

The PWR is the most common reactor type in the world. Sweden has three PWR's, Ringhals 2, 3 and 4. They are of US design (Westinghouse) [104].

Ringhals 4 uses conventional uranium dioxide fuel, enriched in ^{235}U to between 1.8 and 3.6 percent [105]. The fuel consists of pellets, around 8 mm in diameter and length.The pellets are stacked and encapsulated in helium-filled zircalloy cladding tubes, 3.5 meters in length (called rods), and assembled into 17x17 arrays (bundles). In the array, some of

---

[2] Carried out mainly by gamma spectroscopy at Studsvik Nuclear.

the positions are occupied by guide tubes for control rods and instruments, see *Figure 9.1*

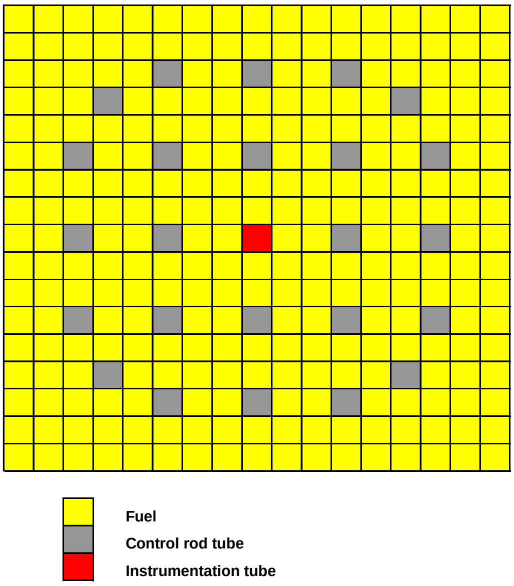

Figure 9.1 Schematic picture of a fuel assembly (bundle) in Ringhals 4.

The control rods are of a silver-cadmium-indium alloy and encased in stainless steel. To keep the array in position and reduce vibrations, the rods are kept in place by seven grid spacers, distributed along the bundle. The bundles are then placed in the 157 positions in the reactor core. The positioning of them is extremely important in order to obtain a homogenous power distribution in the core.

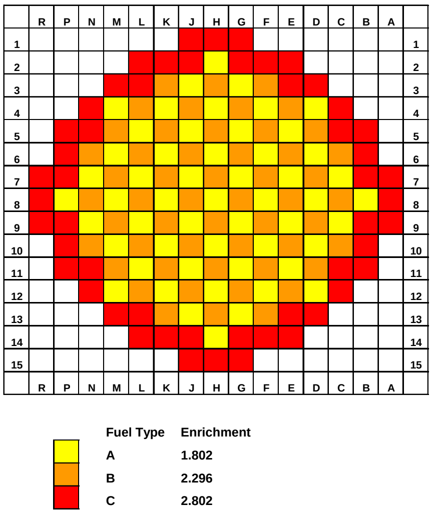

	R	P	N	M	L	K	J	H	G	F	E	D	C	B	A	
1							🟥	🟥	🟥							1
2					🟥	🟥	🟥	🟨	🟥	🟥	🟥					2
3				🟥	🟥	🟧	🟨	🟧	🟨	🟧	🟥	🟥				3
4			🟥	🟨	🟧	🟨	🟧	🟨	🟧	🟨	🟧	🟨	🟥			4
5		🟥	🟥	🟧	🟨	🟧	🟨	🟧	🟨	🟧	🟨	🟧	🟥	🟥		5
6		🟥	🟧	🟨	🟧	🟨	🟧	🟨	🟧	🟨	🟧	🟨	🟧	🟥		6
7	🟥	🟥	🟨	🟧	🟨	🟧	🟨	🟧	🟨	🟧	🟨	🟧	🟨	🟥	🟥	7
8	🟥	🟨	🟧	🟨	🟧	🟨	🟧	🟨	🟧	🟨	🟧	🟨	🟧	🟨	🟥	8
9	🟥	🟥	🟨	🟧	🟨	🟧	🟨	🟧	🟨	🟧	🟨	🟧	🟨	🟥	🟥	9
10		🟥	🟧	🟨	🟧	🟨	🟧	🟨	🟧	🟨	🟧	🟨	🟧	🟥		10
11		🟥	🟥	🟧	🟨	🟧	🟨	🟧	🟨	🟧	🟨	🟧	🟥	🟥		11
12			🟥	🟨	🟧	🟨	🟧	🟨	🟧	🟨	🟧	🟨	🟥			12
13				🟥	🟥	🟧	🟨	🟧	🟨	🟧	🟥	🟥				13
14					🟥	🟥	🟥	🟨	🟥	🟥	🟥					14
15							🟥	🟥	🟥							15
	R	P	N	M	L	K	J	H	G	F	E	D	C	B	A	

	Fuel Type	Enrichment
🟨	A	1.802
🟧	B	2.296
🟥	C	2.802

Figure 9.2 Core load plan for cycle 1.

One bundle consists of one type of fuel, but different bundles can have different fuel. This makes it possible to control the reactivity and burnup of the fuel. Typically, the more enriched fuel is placed in the periphery, where the lower neutron density is compensated by a higher enrichment, thus smoothing out the effect gradient.

Every one year or so, about a third of the fuel (the more consumed part) is exchanged for new fuel. The new fuel is oftenmost placed in the periphery, as mentioned above. At the same time, the other two thirds are rearranged in order to optimize the performance with respect to power distribution, burnup and neutron density. This rearrangement is far from straightforward; the theoretical possibilities being 157!, a number with 279 digits, most of them, however technically infeasible. The trend is towards higher and higher enrichment, now approaching four percent. This allows longer cycles and higher output (burnup).

Reactivity in a PWR is affected mainly by three factors: Fuel burnup, boron content in the coolant water and control rod positions. In addition to this, during cycle one, boron glass absorbers occupied some of the empty control rod tubes. This is to compensate for the over-reactivity due to the loading of only fresh fuel at startup. Boron is a burnable absorber. During operation, it will be consumed via the reaction ^{10}B(n,α) → ^{7}Li. In newer fuel designs (from cycle 2), this role is taken over by gadolinium.

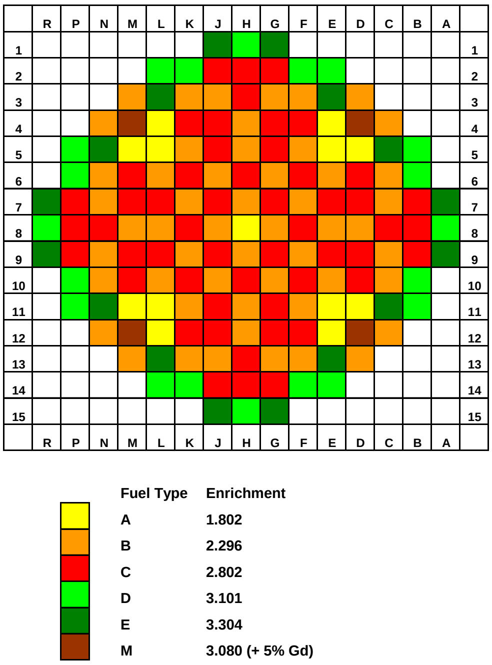

	Fuel Type	Enrichment
🟨	A	1.802
🟧	B	2.296
🟥	C	2.802
🟩	D	3.101
🟩	E	3.304
🟫	M	3.080 (+ 5% Gd)

Figure 9.3 Core load plan for cycle 2. Fuels type A, B and C remain from cycle 1.

9.1.4 Modeling the Ringhals 4 in MCNP/MCB

9.1.4.1 Geometry and limitations

The basic geometry of the core is described above. In order to make a computer model, however, a reasonable amount of simplifications have to be done. Ideally, these should not affect the results significantly.

A few observations can be made:

1) The fuel is kept in place locally and consists of the same material (within the bundle).
2) The bundles will be rearranged at every revision.
3) Although the control *tubes* belong to the bundles, the control *rods* are static objects in the reactor vessel (not all bundle positions in the core have control rods). A bundle could therefore contain rods in one cycle, and not in the next.
4) Equipment outside the core do not affect neutronics.

As it seems, it should be important to be able to move around the bundles. The fuel assemblies should therefore be modeled as static objects, but with unique identifiers. The model of the bundle could on the other hand be very detailed.

Geometry programming was carried out in the following way. A division of the model was made into three levels:

1) Rod level
2) Bundle level
3) Core level

These were then programmed consecutively and independently from each other.

Level one is very simple. The fuel rod is made in one piece, like a simple cylinder, surrounded by helium and cladding. The control tubes were of two varieties; one empty and one with a control rod inside.

On level two, the fuel rods and guide tubes were assembled into a 17x17 square lattice (a bundle) according to *Figure 9.1*. One complication arises from the spacers, which impose considerable effect on the neutron flux. This has to be modeled. Every bundle is thus duplicated; one horizontal cross-section with spacers and one without, and then assembled according to specifications.

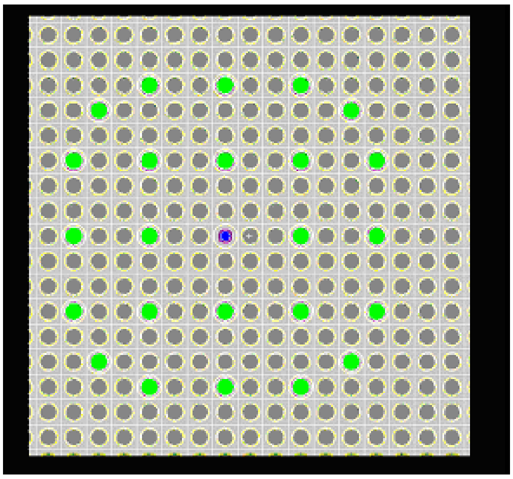

Figure 9.4 MCNP plot of a 22x22 cm cross-section of the geometrical model showing one bundle with fuel and control rods.

Features that are also modeled, but do not form a part of the active core, are the plenum above the fuel, the spring, and top and bottom plates.

Since every of the 157 bundles had to be programmed individually (different materials), this takes up a great part of the code. Each of the 45,373 rod positions makes two entries in the input code; one in spacer and one without.

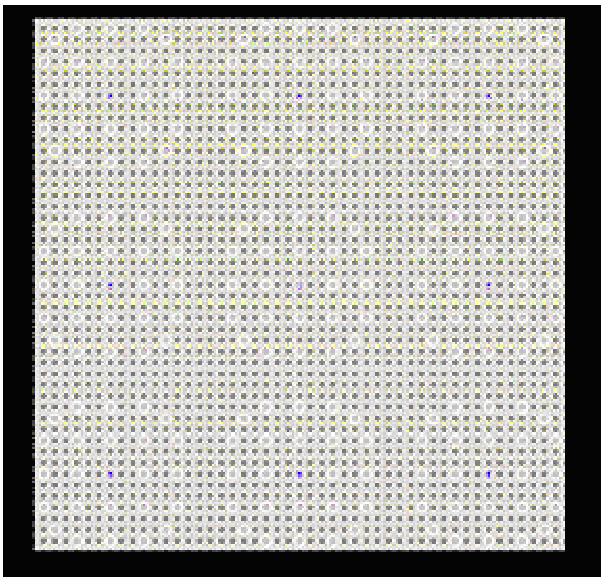

Figure 9.5 MCNP plot of a 60x60 cm cross-section of the geometrical model.

On level three, the bundles are placed in their respective positions in the core according to the load plan of cycle one.

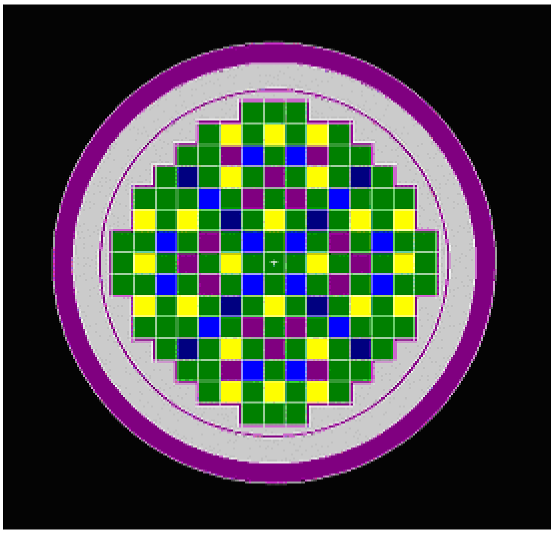

Figure 9.6 MCNP plot of a 250x250 cm cross-section of the core showing the bundles loaded (the different colours indicate positions of different types of control rods), baffle and thermal protection plates and reactor vessel wall.

At refueling, though, the bundles will not be moved (since the control rods have static positions). Instead, in the simulations, the materials are shuffled. One disadvantage is that if the bundles have different materials in the spacers, this has to be corrected for in the original model. Some other features of the core have to be modeled correctly, including the baffle plate, thermal protection plate and upper and lower core plates. For the sake of completion, the reactor vessel itself is also in the model.

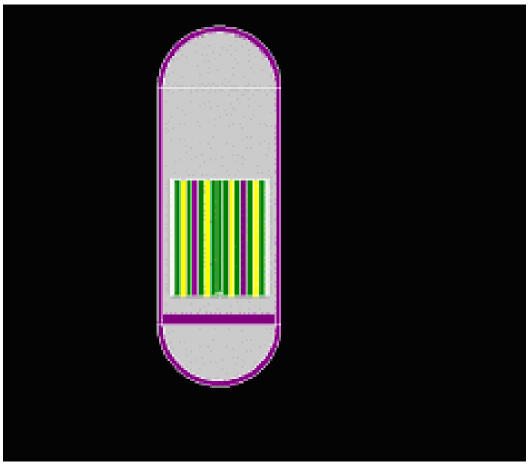

Figure 9.7. Axial cross-section of the reactor vessel.

9.1.4.2 Special refinements of the model

In order to be able to investigate the behaviour of single rods and pellets, one of the bundles is divided into 110 “slices” from bottom to top, with 33 mm equidistance. This bundle can be placed in any position, and makes it possible to monitor axial behaviour and material development in the core.

Likewise, one of the bundles consists of rods that are divided into 41 concentrical “shells” from the center and out, with 100 µm equidistance, making it possible to investigate radial effects on the fuel rods.

During cycle one, these bundles were (arbitrarily) placed in positions 7R and 2E (Figure 9.2), respectively.

9.1.5 Modeling of reactor operation during cycle one

Reactor cycle one lasted between startup of the reactor on 19.5.82 and shutdown for revision on 19.6.84.

Operational data from Ringhals 4 was provided by Vattenfall AB. The power over time is essential to the model. Since this data consists of thousands of numbers, only the overall trend is possible to model. The choice was made to discretize the period into 12 steps according to Figure 9.8

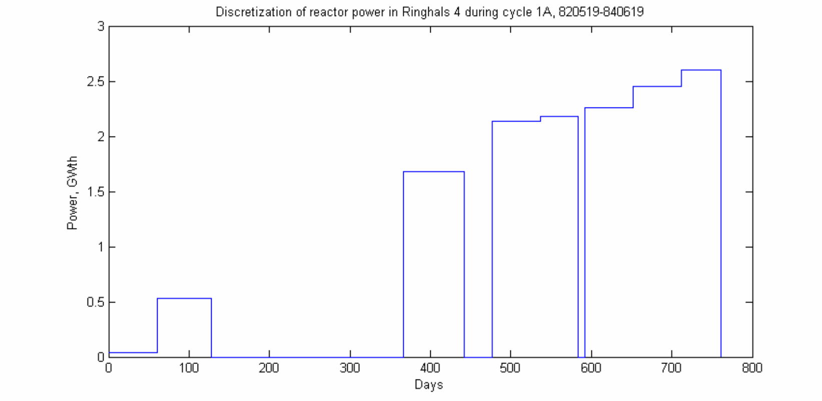

Figure 9.8 The discretization of power versus time in cycle 1.

In order to obtain valid conditions for the simulated operation of the reactor, boron content in the water and control rod positions have to be adjusted at several times during the cycle. At startup, this was achieved through iterative MCNP kcode simulation to attain criticity (keff = 1), and also in order to get a start distribution for the neutrons. In this step, circa $50*10^9$ neutrons were sampled.

At three steps in the cycle, this would again be repeated to compensate for the reduced reactivity due to fuel burnup, with reduced boron content and extraction of the control rods.

9.1.6 Some results from cycle 1

9.1.6.1 Axial power distribution

The axial power distribution on startup was checked on the axial sample bundle in position 7R. The result after approximately 10^{11} neutron histories shows good accordance with the expected cosine function. The effect from some of the spacers is also visible.

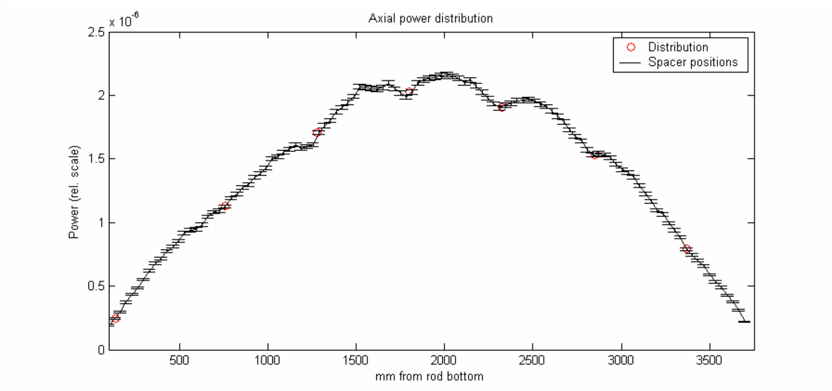

Figure 9.9 Axial power distribution along a fuel rod in position 7R together with the statistical deviation error bars.

9.1.6.2 Boron effect on reactivity

The negative reactivity effect of boron in the water was simulated during startup, and was found to be 11.9±0.2 pcm/ppm boron. The reference value [104] is 12 pcm/ppm.

9.1.6.3 Axial caesium-137 concentration

At two stages during cycle one (after burnups of 5.4 and 12.4 GWd/tU), the ^{137}Cs concentration in the axial fuel rod in position 7R was monitored, demonstrating the accumulation of the isotope as a function of burnup. ^{137}Cs was chosen because it is the most common isotope investigated in fuel gamma spectroscopy, and many validation data exist. Here, the effect of the spacers are even more visible.

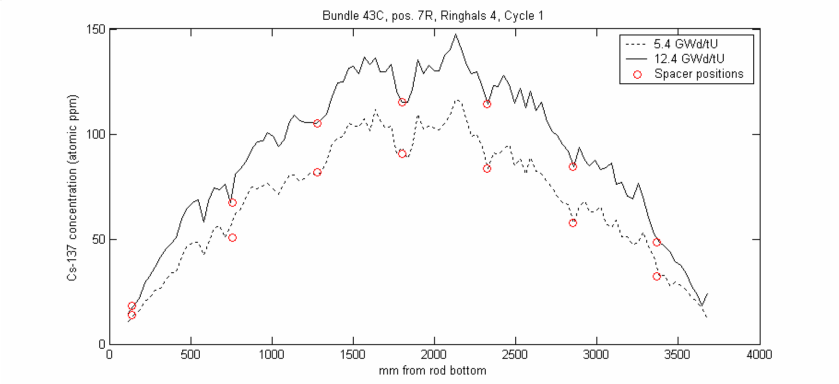

Figure 9.10. ^{137}Cs concentration along a fuel rod in position 7R after two of the burnup steps.

9.1.6.4 The rim effect

As neutrons reenter the fuel rod, they should ideally have been thermalized. However, the fraction that are in the intermediate energy regions (epithermal), will be absorbed as soon as they enter the fuel rod via the reaction $^{238}U(n,\gamma) \rightarrow {}^{239}U$, which via two beta decays in a few days forms ^{239}Pu [106]. This leads to an accumulation of ^{239}Pu on the periphery of the fuel.

The ^{239}Pu will further absorb neutrons: $^{239}Pu \rightarrow {}^{240}Pu \rightarrow {}^{241}Pu \rightarrow {}^{242}Pu$. Out of these, ^{239}Pu and ^{241}Pu are fissionable with thermal neutrons. The accumulation of these on the periphery will thus lead to an increased power (Figure 9.11 and Figure 9.12) and subsequent burnup in this region (Figure 9.13). This is commonly referred to as the “rim effect”.

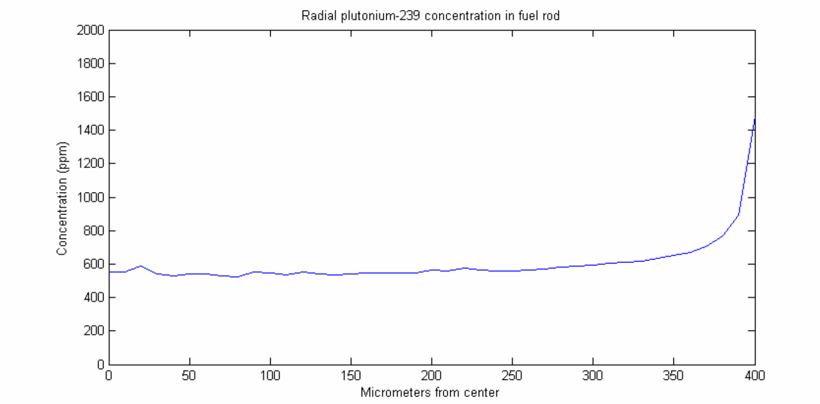

Figure 9.11. Formation of ^{239}Pu in a fuel rod in position 2E.

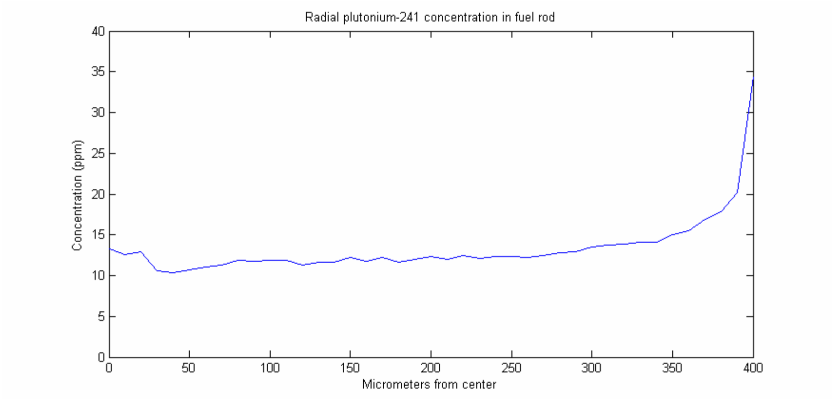

Figure 9.12 Formation of ^{241}Pu via neutron capture in ^{239}Pu in a fuel rod in position 2E.

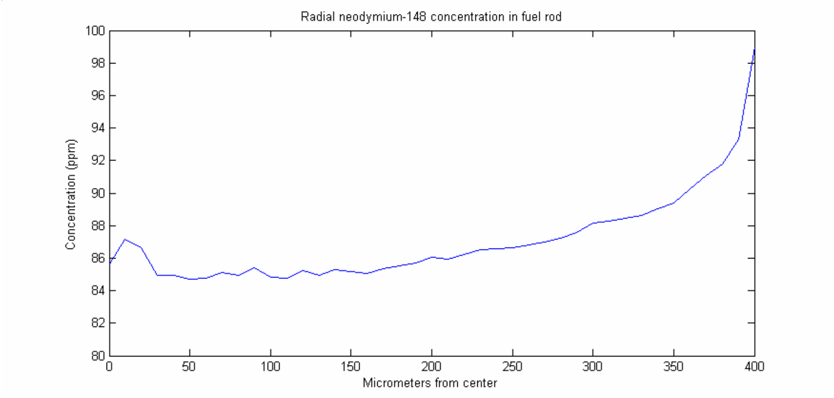

Figure 9.13 Radial concentration of ^{148}Nd in a fuel rod in position 2E.Concentration of this isotope corresponds to burnup.

To monitor burnup in fuel, the content of the fission product ^{148}Nd is often used [106]. It has three major advantages. Firstly, it tends to stay where it was formed, secondly, it is not present in the fuel from the beginning and third, it is a stable isotope. It is formed via neutron capture by ^{147}Nd, which comes directly from fission. Hence, the concentration of ^{148}Nd anywhere in the fuel will be proportional to the number of fissions having occured in that region, and thus the burnup.

9.1.7 Conclusions and future work.

The model seems to show very good correspondence with reactor physical phenomenae such as power distribution and reactivity control. Also, the irradiation effects on the fuel itself seem confirmed on a rod level.

As for now, there are no experimental data specifically from Ringhals 4 available. They are from cycle 13 onwards. Further improvement in computer capacity at the department will make it possible to reach this within a few months.

9.2 NUCLEAR DATA SUPPORT FOR ADS CALCULATIONS

The nuclear data libraries for Monte Carlo stationary and MCB-burnup calculations are under continuous development and tests at KTH. At the moment the following nuclear data libraries are available:

- ENDF/B6 version 8
- JENDL version 3.2
- JEF version 2.2
- JENDL version 3.3
- JEF version 3.0
- EAF version 99
- EAF version 2000
- JANIS ver. 1.1 and 2.1

The nuclear data for Pu-isotopes (239, 240, 241, 242) for energies up to 150 MeV have been added into libraries. Amercium data files are under preparation

11 INTERNATIONAL INTERACTIONS, SEMINARS AND CONFERENCES

In 2003 KTH prepared first an Expression of Interest and then an EU-proposal for a project: “Impact of Transmutation and Reduction of Wastes on Nuclear Waste Reopsitory”. The Project with 23 partners from 11 European countries has been approved with a KTH coordination. Start of the project – March 2004, EU-funding 2 MEuro.

KTH has in 2003 actively prepared for an Integrated EU project “Eurotrans”. First preparatory meetings took place in Karlsruhe in November and December 2003.

In 2003 two important ISTC projects have been approved for funding: Subcritical Assembly in Dubna – SAD project, and nitride nuclear fuel development MATINE-project. KTH is a major collaborator for this projects. The projects will start in 2004.

Waclaw Gudowski participated in following international meetings, workshops and conferences:

- Invited speaker for the public hearing of the French Parliament on Nuclear Waste Treatment (April 2003)
- European meetings:
    - EU-Project ADOPT meetings in Paris and Brussels (March 2003)
    - EU-ADOPT Project: International Workshop on P&T and ADS Development, October 6-8, 2003 SCK•CEN, Mol, Belgium
    - EU-Project Confirm and Future meeting in Sigtuna (June 2003)
    - EU-Project HINDAS – Final workshop in Darmstadt (September 2003)
    - EU-Project MOST meeting in Paris (March 2003)
    - EU-Project MUSE meeting in Madrid (May 2003)
    - EU-Project PDS-XADS meeting in Stockholm (April 2003)
    - Preparation for a new EU-Project RED-IMPACT – meeting in Brussels (September 2003)
    - Preparation of a new EU-Project EUROTRANS – meetings in Karlsruhe (November, December 2003)

- Sixth International Meeting on Nuclear Applications of Accelerator Technology Accelerator Applications in a Nuclear Renaissance – AccApp’03, June 1-5, 2003 • San Diego, CA
- IAEA and YALINA-experiment meeting in Minsk (May 2003) The 21st Conference of the Israel Nuclear Societies, May 22-23, 2002—Haifa, Israel (invited speaker)
- Contact Expert Group of the International Science and Technology Centre annual meeting in Brussels (January 2003)

Janne Wallenius:

- EU-meetings
    - ITEM Project meeting, Brussels (January and October 2003)
    - CONFIRM/FUTURE meeting Sigtuna (June 2003)
    - SPIRE meeting in Stockholm (September 2003)
    - ADOPT workshop in Brussels (October 2003)
    - FUTURE meeting in Paris (December 2003)
- ISTC Contact Expert Group meeting in Brussels (January 2003)
- Lecture on "Nordic Reactor Physics Conference" in Helsinki (April 2003)
- Fe-Cr workshop in Stockholm (April 2003)
- Presentation on Sixth International Meeting on Nuclear Applications of Accelerator Technology Accelerator Applications in a Nuclear Renaissance – AccApp’03, June 1-5, 2003 • San Diego, CA
- Invited speaker at FZK, Karlsruhe (July 2003)
- Invited speaker at JAERI, Tokai (July 2003)
- Fe-Cr workshop in Mol (October 2003)
- NEA/OECD meeting in Oak Ridge (November 2003)
- Presentation at GLOBAL 2003 Meeting in New Orleans, Nov. 16-20, 2003

Mikael Jolkkonen

- PSI (Switzerland): Colloquium on process modeling (March, 2003)
- Santa Fe (USA): "Materials Modeling and Simulations for Nuclear Fuels" workshop (June,2003)

- Sigtuna: FUTURE meeting (June, 2003)
- New Orleans (USA): "Global 2003 ANS/ENS International Winter Meeting" and "Materials Modeling and Simulations for Nuclear Fuels (MMSNF2) workshop" (November, 2003)

Marcus Ericsson:

- NEA/OECD WPPT Meeting in Paris, (March, 12-14, 2003)
- NEA/OECD WPPT Meeting in Oak Ridge, (November 10-14, 2003)
- GLOBAL 2003 Meeting in New Orleans, (November 16-20, 2003)

Daniel Westlén

- GLOBAL 2003 Meeting in New Orleans, Nov. 16-20, 2003

11 REFERENCES

[1] W. Gudowski, et al.: System and safety studies of accelerator driven transmutation, SKB Annual Report 2002, R-03-21, 2003

[2] K. Tuček, J. Wallenius, and W. Gudowski: Coolant Void Worth in Fast Breeder Reactors and Accelerator-Driven Transuranium and Minor-Actinide Burners, Accepted for publication in *Annals of Nuclear Energy*, 2004

[3] J.F.Briesmeister, 2002. A general Monte Carlo N-Particle transport code – version 4c. LANL, LA-13709-M.

[4] J. Cetnar, W. Gudowski and J. Wallenius, 1999. MCB : a continuous energy Monte Carlo burnup simulation code, in actinide and fission product partitioning and transmutation. EUR 18898 EN, OECD/NEA 523.

[5] J. Cetnar, W. Gudowski and J. Wallenius. Monte Carlo continuous energy burnup MCB1C – The description, methods and benchmarks. In preparation for Nuclear Science and Engineering.

[6] J. Cetnar, W. Gudowski, J. Wallenius and K. Tucek, 2001. Simulation of nuclide transmutation with Monte-Carlo Continuous Energy Burnup Code (MCB1C). Proc. Accelerator application 2001 and ADTTA 2001 Nuclear application in the new millennium, Reno (USA). ANS.

[7] J. CETNAR, J. WALLENIUS, W. GUDOWSKI “MCB: A Continuous Energy Monte-Carlo Burnup Simulation Code” in “Actinide and Fission Product Partitioning and Transmutation” - Proc of the Fifth Int. Information Exchange Meeting, Mol, Belgium November 25-27, pp 523-527, AEN NEA OECD (1999)

[8] EURATOM Council Directive 96/29/EURATOM in “The Basic Safety Standards” Safety Series No. 115, (1996) IAEA

[9] J. WALLENIUS et al., Application of burnable absorbers in an accelerator driven system”, Nucl. Sci. Eng., 96, 137 (2001).

[10] K. TUCEK et al., “Source Efficiency in an Accelerator-Driven System with Burnable Absorbers,” Int. Conf. on Back-End of the Fuel Cycle: From Research to Solutions, GLOBAL 2001, Paris, France (2001).

[11] P. SELTBORG and R. JACQMIN, “Spallation Neutron Source Effects in a Sub-Critical System,” Int. Meeting AccApp'01, November 11-15, 2001, Reno, Nevada, USA (2001).

[12] A. RINEISKI and W. MASCHEK, “On Application of Quasistatic and Point-Kinetics Schemes for Subcritical Systems With External Neutron Source,” Nuclear Mathematical and Computational Sciences: A Century in Review - A Century Anew, M&C 2003, Gatlinburg, Tennessee, USA, April 6-11 (2003).

[13] D. G. CACUCI, “On Perturbation Theory and Reactor Kinetics: From Wigner’s Pile Period to Accelerator Driven Systems,” PHYSOR 2002, Seoul, Korea, October 7-10 (2002).

[14] A. F. HENRY, "The Application of Reactor Kinetics to the Analysis of Experiments," *Nuclear Science and Engineering,* **3**, 52-70 (1958).

[15] E. P. GYFTOPOULOS, Chapter on "General Reactor Dynamics," in *The Technology of Nuclear Reactor Safety*, Vol. 1, p. 175-204, T. J. THOMPSON and J. G. BECKERLY, Eds., The MIT Press, Cambridge, Massachusetts, USA (1964).

[16] J. B. YASINSKY and A. F. HENRY, "Some Numerical Experiments Concerning Space-Time Reactor Kinetics Behavior," *Nuclear Science and Engineering,* **22**, 171-181 (1965).

[17] K. O. OTT and D. A. MENELEY, "Accuracy of the Quasistatic Treatment of Spatial Reactor Kinetics," *Nuclear Science and Engineering*, **36**, 402-411 (1969).

[18] "Comparison Calculations for an Accelerator-driven Minor Actinide Burner," OECD/NEA Nuclear Science Committee, NEA/NSC/DOC(2001)13, OECD (2002). Benchmark prepared by P. WYDLER and H. TAKANO, NEA/NSC/DOC(99)13, Revised 27 Aug. 1999.

[19] M. SALVATORES, et al., "Long-lived radioactive waste transmutation and the role of accelerator driven (hybrid) systems," *Nucl. Instrum. Methods Phys. Res., Sect. A*, **414**, 5-20 (1998).

[20] J. E. CAHALAN, T. AMA, G. PALMIOTTI, T. A. TAIWO, and W. S. YANG, "Development of a Coupled Dynamics Code with Transport Theory Capability," PHYSOR 2000, Pittsburgh, USA, 7-11 May (2000).

[21] R. D. LAWRENCE, "The DIF3D Nodal Neutronics Option for Two- and Three-Dimensional Diffusion Theory Calculations in Hexagonal Geometry," ANL-83-1, Argonne National Laboratory (1983).

[22] T. A. TAIWO, "DIF3D-K: A Nodal Kinetics Code for Solving the Time-Dependent Diffusion Equation in Hexagonal-Z Geometry," ANL/NPR-92/17, Argonne National Laboratory (1992).

[23] W. M. STACEY, Jr., *Space-Time Nuclear Reactor Kinetics*, p. 43-46, Academic Press, New York, USA (1969).

[24] R. D. LAWRENCE, "Perturbation Theory Within the Framework of a Higher-Order Nodal Method," *Trans. Am. Nucl. Soc.,* **46**, 402 (1984).

[25] W. MASCHEK, A. RINEISKI, K. MORITA, M. FLAD, "Inherent and Passive Safety Measures in Accelerator Driven Systems: A Safety Strategy for ADS," GLOBAL 2001, Paris, France, Sep 9-13 (2001).

[26] M. ERIKSSON, J. WALLENIUS, J. E. CAHALAN, K. TUCEK, and W. GUDOWSKI, "Safety analysis of Na and Pb-Bi coolants in response to beam instabilities," Proc. 3rd International Workshop on Utilisation and Reliability of High Power Proton Accelerators, Santa Fe, USA, May (2002).

[27] FUTURE, Fuels for Transmutation of Transuranium Elements, Contract FIKI.CT-2001-00148, 5th Framework Program EU, (2001).

[28] J. Wallenius, "CONFIRM: Collaboration on Nitride Fuel Irradiation and Modelling," Proc. AccApp/ADTTA, Reno November 2001, ANS.

[29] N. Chauvin, et al., "In-pile studies of inert matrices with emphasis on magnesia and magnesium aluminate spinel," *J. Nucl. Mater.* 274 (1999) 91-97.

[30] J. Wallenius, "Neutronic aspects of inert matrix fuels for application in ADS," *J. Nucl. Mater.* 320 (2003) 142-146.

[31] M.K. Meyer, G.L. Hofman , S.L. Hayes, C.R. Clark, T.C. Wiencek, "Low-temperature irradiation behavior of uranium–molybdenum alloy dispersion fuel," *J. Nucl. Mater.* 304 (2002) 221–236.

[32] A. Fernández, D. Haas, R.J.M. Konings, J. Somers, "Fuel/Target Concepts for Transmutation of Actinides," 6th Information Exchange Meeting on Actinide and Fission Product Partitioning and Transmutation, Madrid, 11-13 December (2000).

[33] H. Kleykamp, "Selection of materials as diluents for burning of plutonium fuels in nuclear reactors," *J. Nucl. Mater.* 275 (1999) 1-11.

[34] M. A. Mignanelli and R. Thetford, in: Proceedings on Advanced Reactors with Innovative Fuels, Chester, Uk., (2001). or M. A. Mignanelli and R. Thetford, "Physical Properties of Minor Actinides and Diluents in Oxide Fuel Pins," Restricted Report by BNFL, Oct. (2000).

[35] R. Thetford and M. Mignanelli, "The chemistry and physics of modeling nitride fuels for transmutation," *J. Nucl. Mater.* 320 (2003) 44.53.

[36] Y. Suzuki and Y. Arai, "Thermophysical and thermodynamic properties of actinide mononitrides and their solid solutions," *J. Alloys and Compounds*, 271-273 (1998) 577-582.

[37] Y Touloukian et al, Thermophysical properties of matter, Vol. 1, 1970, New York, Plenum.

[38] Y. Arai, et al., "Dependence of the thermal conductivity of (U,Pu)N on porosity and plutnium content," *J. Nucl. Mater.* 195 (1992) 37-43.

[39] E. H. P. Cordfunke, R. J. M. Konings, G. Prins, P. E. Potter, and M. H. Rand, Thermochemical Data for Reactor Materials and Fission Products, Elsevier Science, Amsterdam (1990).

[40] J. J. Katz, G. T. Seoborg, and L. R. Morss, *The chemistry of the actinide elements*, 2nd Ed., Vols. 1 and 2, Chapman and Hall, London (1986).

[41] J. Edwards, et. al, *Fast Reactor Manual*, Fast Reactor European Collaboration report, 1990.

[42] S. Casalta, Hj. Matzke, C. Prunier, Proc. GLOBAL'95, Int. Conf. On Evaluation of Emerging Nuclear Fuel Cycle Systems, Versailles, France, Sep. 11-14, 1995, p. 1725.

[43] H. Zhang, R. J. M. Konings, M. E. Huntelaar, and E. H. P. Cordfunke, "Melting behaviour of oxide systems for heterogeneous transmutation of actinides. III. The system Am-Mg-O," *J. Nucl. Mater.* 250 (1997) 88-95.

[44] H. Zhang, R. J. M. Konings, M. E. Huntelaar, and E. H. P. Cordfunke, ”Melting behaviour of oxide systems for heterogeneous transmutation of actinides. I. The systems Pu-Al-O and Pu-Mg-O,” *J. Nucl. Mater.* 249 (1997) 223-230.

[45] M. Jolkkonen, M. Streit , J. Wallenius, “Thermo-chemical modelling of uranium-free nitride fuels,” *Journal of Nuclear Science and Technology* 41 (2004), in press.

[46] H. Bailly, D. Menessier, and Prunier C, The Nuclear Fuel of Pressurized Water Reactors and Fast Neutron Reactors, p. 167, Lavoisier Publishing, Paris (1999).

[47] C. W. Hunter, R. L. Fish, and J.J. Holmes, “Mechanical Properties of Unirradiated Fast Reactor Cladding During Simulated Overpower Transients,” *Nuclear Technology*, Vol. 27, p. 376-388 (1975).

[48] M. L. Hunter, G. D. Johnson, C. W. Hunter, and D. R. Duncan, “Mechanical Behavior of Irradiated Fuel Pin Cladding Evalued Under Transient Heating and Pressure Conditions,” British Nuclear Energy Society Conference, Brighton, Great Britain, April (1983).

[49] I. Shibahara, et al., ”Mechanical Property Degradation of Fast Reactor Fuel Cladding During Thermal Transients,” Effects of Radiation on Materials: 16th Int. Symposium, ASTM STP 1175, p. 664-678, Philadelphia (1994).

[50] N. S. Cannon, F. H. Huang, and M. L. Hamilton, “Simulated Transient Behavior of HT-9 Cladding,” Effects of Radiation on Materials: 14th Int. Symposium, ASTM STP 1046, Vol. 2, p. 729-738, Philadelphia (1990).

[51] N. S. Cannon, F. R. Huang, and M. L. Hamilton, “Transient and Static Mechanical Properties of D9 Fuel Pin Cladding and Duct Material Irradiated to High Fluence,” Effects of Radiation on Materials: 15th Int. Symposium, ASTM STP 1125, p. 1071-1082, Philadelphia (1992).

[52] M. G. Adamson, et al., ”Synergistic tellurium-caesium embrittlement of Type 316 stainless steel”, *Nature*, 295, p. 49, 7 Jan., 1982.

[53] S. Tani, S. Nomura, and I. Shibahara, “Fuel Cladding Mechanical Property Degradation Mechanisms and Fuel Reliability Under Transient Conditions,” Int. Conf. on Reliable Fuels for Liquid Metal Reactors, Sep. 7-11, Tucson (1986).

[54] A. Fissolo, et al., “ Tensile Properties of Neutron Irradiated 316Ti and 15-15Ti Steels,” Effects of Radiation on Materials: 16th Int. Symposium, ASTM STP 1175, p. 646-663, Philadelphia (1994).

[55] R. J. Puigh and M. L. Hamilton, Influence of Radiation on Materials Properties: 13th Int. Symposium, ASTM STP 956, p. 22-29, Philadelphia (1987).

[56] R. J. Amodeo and N. M. Ghoniem, “Development of design equations for ferritic alloys in fusion reactors,” *Nuclear Engineering and Design/Fusion*, 2 (1985) 97-110.

[57] ASME Boiler and Pressure Vessel Code, 1977 Code Cases – Nuclear Components, 1977 Edition, Case N-47 (1977) 1592-10.

[58] G. S. Yachmenyov, A. Ye. Rusanov, B. F. Gromov, Yu. S. Belomytsev, N. S. Skvortsov, A. P. Demishonkov, “Problems of structural materials’ corrosion in

lead-bismuth coolant,” Proc. Heavy Liquid Metal Coolants in Nuclear Technology, Vol. 1, p. 133-140, Obninsk, Russia, Oct. 5-9 (1998).

[59] N. Li, et al., ”Corrosion Test of US Steels in Lead-Bismuth Eutectic (LBE) and Kinetic Modeling of Corrosion in LBE Systems,” Proc. AccApp'01, Reno, Nevada, USA, Nov. 11-15 (2001).

[60] J. R. Weeks, C. J. Klamut, “Reactions between steel surfaces and zirconium in liquid bismuth,” *Nucl. Sci. Eng*. 8, 133–147 (1960).

[61] N. N. Novikova, Yu. G. Pashkin , V. V. Chekunov, “Some Features of Sub-Critical Blankets Cooled With Lead-Bismuth,” Proc. Int. Conf. On Accelerator-driven Technologies and Applications, ADTTA’99, Praha, Czech Republic, 7-11 Jun. (1999).

[62] B. Bonin and D. Greneche, 2002. Prospective studies of HTR fuel cycles involving plutonium. IAEA proceedings of the conference on high temperature reactors, Petten (Holland).

[63] A. Talamo, W. Gudowski and F. Venneri, 2004. The burnup capabilities of the Deep Burn Modular Helium Reactor analyzed by the Monte Carlo Continuous Energy Code MCB. Royal Institute of Technology, Stockholm (Sweden). Annals of Nuclear Energy 31/2 pp. 173-196

[64] K. Kugeler, W. von Lensa, G. Haag and H.J. Rütten, 1998. Use of plutonium in pebble bed HTGRs. IAEA international working group on gas-cooled reactors meeting, Beijing (China), IAEA-TECDOC-1210, pp. 229-236.

[65] H. Werner, 1997. Build up of plutonium isotopes in HTR fuel elements, a comparison between computed predictions and chemical analysis. Nuclear Engineering and Design 170, pp. 147-164

[66] M.P. Labar and W.A. Simon, 1994. Comparative economics of the GT-MHR and power generation alternatives. General Atomics, GA-A 21722

[67] W. Fröhling, 1999. Courses and limitations of damage with air ingress accidents in HTR modules. OECD proceedings of the conference on survey on basic studies in the field of high temperature engineering, Paris (France), pp. 173-181.

[68] K. Kugeler and P.W. Phlippen, 1999. Aspects of inherent safety of future high temperature reactors. OECD proceedings of the conference on survey on basic studies in the field of high temperature engineering, Paris (France), pp. 29-39.

[69] K. Kunitomi, S. Nakagawa and M. Shinozachi, 1996. Passive heat removal by vessel cooling system of HTTR during no forced cooling accidents. Nuclear Engineering and Design 166.

[70] R.L. Moore, C.H. Oh, B.J. Merrill and D.A. Petti, 2002. Studies of air ingress for pebble bed reactors. IAEA proceedings of the conference on high temperature reactors, Petten (Holland).

[71] Nakagawa, A. Saikusa and K. Kunitomi, 2001. Development of a simulation model and safety evaluation for a depressurization accident without reactor scram in an advanced HTGR. Journal of Nuclear Science and Technology, 133.

[72] S. Nakagawa, A. Saikusa and K. Kunitomi, 1998. Safety evaluation during a depressurization accident of the SFHTR. IAEA international working group on gas-cooled reactors meeting, Beijing (China), IAEA-TECDOC-1210, pp. 77-84.

[73] W. Schenk, W. Fröhling, R. Moormann, H. Nabielek, 1994. Simulation of air ingress with irradiated fuel samples. JAERI Meeting on validation of predictive methods for fuel and fission product behavior in gas-cooled reactors, Tokai (Japan).

[74] A. Woaye-Hune and S. Ehster, 2002. Calculation of the decay heat removal transient by passive means for a direct cycle modular HTR. IAEA proceedings of the conference on high temperature reactors, Petten (Holland).

[75] C.A. Baldwin and M.J. Kania, 1990. Fission product retention in TRISO coated UO_2 particle fuels subjected to HTR simulate core heating tests. IAEA proceedings of the conference on gas-cooled reactors, Oak Ridge (U.S.A.), IWGGCR-25, pp. 132-138.

[76] P. Chapelot et al., 2001. Requirements for high temperature reactor fuel particle design assessment. Progress in Nuclear Energy 38

[77] K. Fukuda, S, Kashimura, T. Tobita and T. Kikuchi, 1995. Irradiation behavior of HTGR coated particle fuel at abnormally high temperature. Nuclear Engineering and Design 157, pp. 221-230.

[78] I. Golubev, I. Kadarmetov and V. Makarov, 2002. Mathematical model and computer code for coated particles performance at normal operating conditions. IAEA proceedings of the conference on high temperature reactors, Petten (Holland).

[79] G.K. Miller, D.A. Petti and J.T. Maki, 2002. Development of an integrated performance model for TRISO-Coated gas reactor particle fuel. IAEA proceedings of the conference on high temperature reactors, Petten (Holland).

[80] G.K. Miller, D.A. Petti, D.J. Varacalle and J.T. Maki, 2001. Consideration of the effects on fuel particle behavior from shrinkage cracks in the inner pyrocarbon layer. Journal of Nuclear Materials 295, pp. 205-212.

[81] K. Minato, K. Sawa et al., 2000. Fission product release behavior of individual coated fuel particles for HTGR. Journal of Nuclear Science and Technology 131.

[82] K. Minato, T. Ogawa et al., 1993. Release behavior of metallic fission products from HTGR fuel particles at 1600 and 1900 oC. Journal of Nuclear Materials 202, pp.47-53.

[83] H. Nabielek, W. Schenk, W. Heit, A.W. Mehner and D.T. Goodin, 1989. The performance of HTR fuel particles at extreme temperatures. Journal of Nuclear Science and Technology 84, pp. 62-81.

[84] H. Nickel, H. Nabielek et al., 2002. Long time experience with the development of HTR fuel elements in Germany. Nuclear Engineering and Design 217, pp. 141-151.

[85] D.A. Petti, J. Buongiorno, J.T. Maki and G.K. Miller, 2002. Key differences in the fabrication of US and German TRISO-coated particle fuel, and their implications on fuel performances. IAEA proceedings of the conference on high temperature reactors, Petten (Holland).

[86] J. Porta, P. Lo Pinto, M. Bonnet, K. Kugeler et al., 2001. Coated particle fuel to improve safety, design, and economics in water-cooled and gas-cooled reactors. Progress in Nuclear Energy 38, pp.407-410

[87] K. Sawa, S. Suzuki and S. Shiozawa, 2001. Safety criteria and quality control of HTTR fuel. Nuclear Engineering and Design 208, pp. 305-313.

[88] K. Sawa and T. Tobita, 2003. Investigation of irradiation behavior of SiC-Coated fuel particle at extended burnup. Journal of Nuclear Science and Technology 142.

[89] K. Sawa, S. Ueta et al., 2001. Prediction of fuel performance and fission gas release behavior during normal operation of the high temperature engineering test reactor by JAERI and FZJ modeling approach. Journal of Nuclear Science and Technology, pp.411-419.

[90] K. Minato, K. Fukuda, H. Sekino et al., 1998. Deterioration of ZrC-coated fuel particle caused by failure of pyrolitic carbon layer. Journal of Nuclear Materials 252, pp. 13-21.

[91] K. Minato, T. Ogawa, K. Fukuda, H. Sekino, I. Kitagawa and N. Mita, 1997. Fission product release from Zr-coated fuel particles during post-irradiation heating at 1800 and 2000 oC. Journal of Nuclear Materials 249, pp. 142-149.

[92] K. Minato, T. Ogawa, T. Koya et al., 2000. Retention of fission product cesium in ZrC-coated fuel particles for high-temperature gas-cooled reactors. Journal of Nuclear Materials 279, pp.181-188.

[93] K. Minato, T. Ogawa, K. Sawa et al., 2000. Irradiation experiment on ZrC-coated particles for high temperature gas cooled reactors. Journal of Nuclear Science and Technology 130.

[94] JANIS version 1.0. Jef-2.2.

[95] D. Ridikas, L. Bletzacker et al., 2002. Comparative analysis of ENDF, JEF and JENDL data libraries by modeling high temperature reactors and plutonium based fuel cycles. Journal of Nuclear Science and Technology supplement 2, pp. 1167-1170

[96] J.J. Kim, J.T. Lee and H.R. Kim, 1989. Generation and Benchmarking of a 69 Group Cross Section Library for Thermal Reactor Applications. J. Korean Nucl. Soc., 21, 245

[97] C.J. Taubman, 1975. The WIMS 69-Group Library Tape 166259. Report AEEW-M1324, U.K. Atomic Energy Authority, Winfrith (Great Britain).

[98] S. T. Nakata, Y. Matsuki and T. Mouri, 1995. Plutonium burning with high temperature gas-cooled reactor. Progress in Nuclear Energy 29, pp. 209-215.

[99] General Atomic, 2002. GT-MHR conceptual design description report. GA/NRC-337-02.

[100] R. Thetford, 2000. Physical properties of minor actinides and diluents in oxide fuels. AEA technology report ARMM/P(00)15.

[101] B.J. Marsden, G.N. Hall and J. Smart, 1998. Nuclear graphite ageing and turnaround. IAEA international working group on gas-cooled reactors meeting, Beijing (China), IAEA-TECDOC-1210, pp. 133-153.

[102] H. Matsuo, S. Nomura, H. Imai and T. Oku, 1986. Effects of high temperature neutron irradiation on the physical, chemical and mechanical properties of fine-grained isotropic graphite. JAERI specialists meeting on graphite component structural design, Tokai (Japan).

[103] K. Ohashi, F. Okamoto and H. Hayakawa, 2000. Modular High temperature reactor contributing the global environmental protection. Progress in Nuclear Energy 37, pp. 307-312.

[104] Bengt Pershagen, Lättvattenreaktorers Säkerhet, EFN Report, 1986

[105] Bränslepärm Ringhals 4, AB Vattenfall

[106] Bailly, Ménessier, Prunier, “The nuclear fuel of pressurized water reactors and fast neutron reactors”, Lavoisier Publishing, 1999